To the Graduate Council:
I am submitting herewith a dissertation written by Deepak Bhandari entitled "Surface-Enhanced Raman Scattering: Substrate Development and Applications in Analytical Detection." I have examined the final electronic copy of this dissertation for form and content and recommend that it be accepted in partial fulfillment of the requirements for the degree of Doctor of Philosophy, with a major in Chemistry.

Michael J. Sepaniak, Major Professor

We have read this dissertation
and recommend its acceptance:

David Joy

Frank Vogt

Ziling (Ben) Xue

Accepted for the Council:

Carolyn R. Hodges

Vice Provost and Dean of the Graduate School

(Original signatures are on file with official student records.)

Surface-Enhanced Raman Scattering: Substrate Development and Applications in Analytical Detection

A Dissertation
Presented for the
Doctor of Philosophy Degree
The University of Tennessee, Knoxville

Deepak Bhandari
May 2011

Copyright©2011 Deepak Bhandari
All Rights Reserved

Dedicated to my beloved father late Min B. Bhandari who passed away from brain lymphoma on December 24, 2010. May his soul rest in peace.

With Love....

Acknowledgements

At first, I would like to thank Professor Sepaniak for his thoughtful guidance and support. It is an honor to have you as a research advisor. Besides science, I have also learned the value of mentorship and professionalism from you. Thank you so much for having me in a *sepaniak group*. I would like to thank previous group members: Nahla AbuHatab for trainings on SERS experiments during my early days in the group and handing over nTP-SERS project to me, Kasey Hill for being a good friend and make me feel my presence in the department, and Zhou Long for all his help. I would also like to thank all present group members: Sabrina Wells for being all time SERS colleague, Lisa Taylor for her generosities, Matthew Walworth for his support on my first publication, Jim Patton and Teresa Kirchner for all their help. I would also like to acknowledge John Dunlap and Greg Jones for their assistance with SEM and AFM at UTK.

I would like to thank all my friends and family who consistently encouraged and helped me to accomplish this advance degree. Special thanks to my wife Bipana Dahal for her love, support, and sacrifice. Without your support I would not be able to finish my dissertation this early!

I would also like to extend my sincere thanks to all the staff members of Chemistry department who have directly or indirectly assisted my research. Thanks to Dr. Liguo Song for his guidance and training on mass spectrometers, Dr. David Cho for lunchtime conversation, and Stephen Gibson for being a great mass spec. colleague. I would also like to thank all the staff members of Center for Nanophase Materials

Sciences (ORNL) for their time and effort to train me on nanofabrication work. Special thanks to Dr. Ivan Kravchenko and Dr. Nickloy Lavrik for all their help and generosities.

Finally, I would like to acknowledge my Ph.D. committee members Prof. Ziling Xue, Prof. Frank Vogt, and Prof. David Joy for their time and support on my graduate work.

Abstract

To advance the capabilities of surface-enhanced Raman scattering (SERS), we developed a silver modified polypropylene filter (AgPPF) substrate which acts as a pseudo stationary phase in harvesting SERS signatures of so called "phytochemical estrogens" and other environmentally significant chemicals. To augment electron beam lithography (EBL) in SERS research, we also introduced an interesting nanotransfer printing (nTP) technique which could circumvent the low throughput and extremely high resolution (< 10 nm) limitations of EBL in designing advanced SERS substrates.

In our study, a nominal average thickness of 10 nm silver on the polypropylene microfiber produced nanoglobules of less than 100 nm in diameter. This noble metal nanoroughen layer allowed AgPPF to serve as a SERS active substrate, onto which the noted endocrine disrupting chemicals were passed through and harvested. The intense, multifeatured vibrational Raman spectra of very rarely SERS studied chemical species collected indicates the potential for useful detection via this approach of creating SERS substrates. AgPPF substrates were also used in characterizing the adsorption behavior of hydroxyl complexes of uranium. Interestingly, hydroxyl group on the uranium complexes showed slow sorption kinetics on the nanostructured silver surfaces. Understanding the adsorption behavior of aqueous solution of uranium on nanostructured silver surfaces has opened up the possibilities of SERS detection of these environmental and non-proliferation concerned species without any surface modifications.

nTP is a high resolution printing technique and relies on interfacial chemistries to control the transfer of thin metal film from a "stamp" to a "substrate". In our research, high-aspect-ratio AutoCAD designed nanopatterns were created on silicon wafers using e-beam lithography and reactive ion etching. Silicon relief pillars based stamps were then used to integrate a variety of nanostructures on different dielectric materials. Thus created nanopatterns have shown their promise to hold their inherent SERS activity. For its simplicity, cost-effectiveness, and ease of operation, this hyphenated nTP-SERS technique is impressive in the selection of suitable supporting-films for better SERS enhancements and also to manipulate gap between nanodiscs (gap-plasmonic SERS effect).

Contents

List of Figures xii

1 Introduction 1

1.1 A brief introduction to Raman spectroscopy 2

1.1.1 The discovery 2

1.1.2 Classical theory and mathematical explanations 2

1.1.3 Instrumentations 6

1.2 Raman terminology (linear and non-linear) 8

2 A Quick Overview of Surface-Enhanced Raman Scattering and Related Topics 12

2.1 The discovery of SERS 12

2.2 SERS enhancement mechanisms 13

2.2.1 Electromagnetic Enhancements 13

2.2.2 The Chemical Enhancement 17

2.2.3 Analytical/Substrate Enhancement Factors 18

2.3 Applications of SERS 20

2.4 SERS substrates 21

2.4.1 Random morphology SERS substrates 22

2.4.2 Periodic or uniform planer SERS substrate 24

3 Dual Function Surface-Enhanced Raman Active Extractor for the Detection of Environmental Contaminants **31**

3.1 Introduction . . . 31

3.2 Experimental . . . 34

3.2.1 Materials . . . 34

3.2.2 Silver Deposition . . . 34

3.2.3 Scanning Electron and Atomic Force Microscopy . . . 35

3.2.4 Sample preparation and preconcentration . . . 35

3.2.5 SERS Measurement and data acquisition . . . 36

3.3 Results and Discussion . . . 37

3.3.1 Substrate Morphology . . . 37

3.3.2 Optimization Studies . . . 39

3.3.3 Performance Studies . . . 43

3.3.4 SERS of Selected Flavonoids . . . 46

3.4 Conclusions . . . 49

3.5 Acknowledgements . . . 49

4 Characterization and Detection of Uranyl Ion Sorption on Silver Surfaces Using Surface-Enhanced Raman Scattering Detection **51**

4.1 Introduction . . . 51

4.2 Materials and Methods . . . 54

4.2.1 Materials . . . 54

4.2.2 Vapor deposition of silver particles . . . 54

4.2.3 Preparation of nanofabricated substrates (electron beam lithography, EBL, and reactive ion etching, RIE) . . . 54

4.2.4 Scanning electron microscopy . . . 56

4.2.5 SERS measurement and data acquisition . . . 56

4.3 Results and Discussions . . . 57

4.3.1 Studies involving experimental conditions . . . 57

4.3.2 Quantitative analysis of uranyl . . . 64
4.3.3 Prospective for nanofabricated SERS substrates in uranyl detection . . . 67
4.4 Conclusions . . . 70
4.5 Acknowledgements . . . 70

5 Stamping High-Aspect-Ratio Plasmonic Nanoarrays on SERS-supporting Platforms 71
5.1 Introduction . . . 71
5.2 Experimental . . . 73
5.2.1 Materials . . . 73
5.2.2 Nanofabrication of Silicon Pillars and Metal Deposition . . . 74
5.2.3 Substrate Preparation and Nanoscale Transfer Printing . . . 74
5.2.4 Scanning Electron and Atomic Force Micrographs . . . 75
5.2.5 SERS Measurements . . . 75
5.2.6 Theoretical Calculations . . . 76
5.3 Results and discussion . . . 77
5.3.1 nTP Process Description . . . 77
5.3.2 nTP Process Optimization . . . 79
5.3.3 SERS Detection . . . 80
5.3.4 Nanogap Manipulation . . . 88
5.3.5 Nanoarrays on a Microfiber Facet . . . 90
5.4 Conclusions . . . 90

6 Concluding Remarks 93

Bibliography 96

A Supporting Information: Stamping High-Aspect-Ratio Plasmonic Nanoarrays on SERS-Supporting Platforms 119

A.1 Functionalization of substrates 119
A.2 In-house built pressure monitoring device and nanotransfer printing . 120
A.3 Nanotransfer printing protocol on fiber optic facet 120

B Nanotransfer Printing *via* Fluropolymer Coated Stamp **123**

Vita **127**

List of Figures

1.1 Schematic of the origin of Rayleigh and Raman scattering 4

1.2 Schematics of JY Horiba LabRam spectrometer used in the current study 9

1.3 Quantum diagram of the linear and nonlinear Raman processes. Each photon is represented by an arrow; ν = laser frequency, ν_s = stokes frequency, ν_a = antistokes frequency, ν_v = vibrational frequency, and GS = Ground state 10

2.1 Schematics of the origin of electromagnetic field enhancement mechanism in SERS 15

2.2 Schematics of the origin of charge-transfer mechanism in SERS 19

2.3 Representation of the nanosphere lithography approach for SERS substrate fabrication. 28

2.4 Electron beam lithography for SERS substrate fabrication: Schematics of stamp fabrication procedure (left) and scanning electron micrographs of EBL created nanofeatures for SERS studies 29

2.5 Schematic depiction of the nanotransfer printing procedure for the creation of nTP-SERS substrate 30

3.1 SEM image of polypropylene prefilter (A) and AFM images of part "a" of Figure 1A, without silver (B) and with 10 nm physically vapor deposited silver (C). 38

3.2 Silver thickness optimization; Band areas centered at 763 cm^{-1} of 5×10^{-7} M R6G on AgPPF substrate at various thickness of silver. The inset is the spectrum of 5×10^{-7} M R6G (conditions: STT; 20x objective; 1s acquisition time; laser excitation of 4.0 mW at 632.8nm; and Ag deposition rate of 1.0 Å/sec). 40

3.3 Effect of Volume passed through AgPPF substrate on SERS signal; (A) Band area centered at 763 cm^{-1} against different load volumes but constant mass R6G solution (patterned bar). Solid bar is of 50 μL aliquot of each diluted solution. (B) SERS responses (triplicate) of 1×10^{-6} M R6G against the volume of analyte dispensed through AgPPF substrate. 150 μL is the optimized volume in our study. (Conditions: same as Figure 3.2) 42

3.4 SERS signatures and detectable spectra of various analyte at low concentration; (A) crystalviolet (B) MDH (C) R6G, and (D) PABA, at optimized conditions (Spectra were collected under STT conditions with 80x objective at 5 sec acquisition time using 4.0 mW, 632.8nm laser excitation) 44

3.5 Comparison of concentration protocol and dipping method for SERS enhancement of 1×10^{-5} M Aminothiophenol (A), and 1×10^{-5} M p-Aminobenzoic acid (B).(Spectra were collected under STT condition with 10x objective at 1 sec acquisition time using 10.0 mW, 632.8nm laser excitation) 45

3.6 SERS signatures of selected Flavonoids; (A) daidzein (B) genistein (C) flavone, and (D) apigenin. (Spectra were collected under STT conditions with 50x objective at 1 sec acquisition time using 4.0 mW, 632.8 nm laser excitation) 47

3.7 (A) SERS spectra of both apigenin and daidzein compared with the SERS spectrum of their mixture. Bands at 837 cm^{-1} and 1217 cm^{-1} are solely due to daidzein and apigenin, respectively. (B, C) Working curves for daidzein and apigenin, respectively. Bottom X- and left Y-axes (designated -A-) are for standard solutions without preconcentration, similarly top X- and right Y- axes (designated –B–) are of preconcentrated solutions. (Conditions; same as Figure 3.6) . . 50

4.1 Representative (a) Raman ([UO_2^{2+}] =0.1M, pH=3.6), and (b) SERS spectra ([UO_2^{2+}] = 5×10^{-7} M, 75 minutes delay time at room temperature, pH=7.1, PPF substrate) of uranyl nitrate hexahydrate solution. 59

4.2 Figure showing the effect of solute-surface interaction time on SERS intensity of uranyl loaded silver. Inset shown is the intensity versus time plot (5×10^{-7} M solution, pH=7.1 at room temperature, and PPF substrate used). [Each error bar indicates the standard deviation associated with three different substrates] 60

4.3 Figure showing the effect of temperature on SERS intensity of uranyl loaded silver. Shown on the top panel are the spectral profiles (5×10^{-7} M solution, pH=7.1, and PPF substrate used). [Each error bar indicates the standard deviation associated with three different spots in the same substrate] 62

4.4 Effect of pH on the symmetric stretching frequency of uranyl (5×10^{-6} M) on the silver modified PPF substrate. 65

4.5 (A) Calibration curve of an aqueous solution of uranyl, and (B) SERS spectra of 4×10^{-8} M uranyl recorded. Spectra were recorded using 50x objective, 2mW laser power and 1 sec acquisition time. The temperature, delay time, and pH were 90°C, 45 minutes, and 7.1, respectively on the silver modified PPF surface. 66

4.6 SEM of nanofabricated ellipse-sphere dimer patterns (A) without silver and (B) with 25 nm thermally vapor deposited silver. 69
4.7 Comparisons of SERS spectra of (A) a SAM of Benzenethiol, and (B) neutral pH solution of Uranyl nitrate; on the nanofabricated ellipse-sphere dimer substrates as a function of nanogaps. 69

5.1 Schematic depiction of the procedure for incorporating nanofeatures on various material surfaces: (a) conventional nanofabrication (e-beam lithogaphy/reactive ion etching) in creating relief nanopillars on silicon wafer, and (b) nanotransfer printing approach. Shown in the insets are SEMs of EBL/RIE fabricated silicon pillars. 78
5.2 Micrographs (AFM, b, SEM a, c, and d) representing transfer printing of metallic nanoarrays: (a) Silver modified nanofabricated silicon pillars prior to stamping. Nanotransfer printed bowtie silver array on (b) PDMS, (c) SU-8, and (d) glass slide. 81
5.3 SERS intensities of Benzenethiol peak centered at 1575 cm^{-1} and Rhodamine 6G peak centered at 763 cm^{-1}, with respect to various underlying substrates using extended arrays of silver (a) bowtie, and (b) dumbbell. 83
5.4 Theoretical calculations of the figure of merit: (a) Geometry of both nanoparticles configurations within the unit cell, where a=1100 nm and b=450nm. The nanoparticles are composed of silver and reside on a material substrate with refractive index nm. (Left) bowtie: w=650nm, v=300nm, g=50nm, p=30nm. (Right) dumbbell: d=300nm, g=50nm, p=30nm. (b) Figure of merit F for glass, PDMS, and SU8 reported relative to the maximum SU-8 value. Blue corresponds to the bowtie and red corresponds to the dumbbell configuration; (c) the variation of F as a function of the sinking parameter s in PDMS. Again results are reported relative to the SU-8 bowtie value. 85

5.5 SERS spectra of Benzenethiol collected from (a) silver modified silicon pillars (RSD ∼9%), and (b) similar nanopattern on SU-8 surface (RSD∼23%). Figures shown on the right hand side are the spectral mapping of probe molecules over 400 μm^2, and on left hand side are superimposed spectra. 86

5.6 Demonstrated an ability to integrate a single-particle to LDNAs macropattern on various substrates; (a, b) single-particle and 4 x 4 arrays of silver nanoparticles on glass substrate. (c, d) relatively large square patterns, consisting of two different types of LDNAs, on a PDMS substrate. (e, f) typical SERS spectra of BT harvested from two different clones. 89

5.7 Demonstrated nanogap reduction by physical manipulation of a elastomer: SEMs of bowtie arrays stamped on (a) a stretched PDMS, and (b) the same pattern after relaxing elastomer. Figures shown at the top are schematics of the gap manipulation. 91

5.8 SEMs of dumbbell arrays: (a) integrated on the fiber optic facet, (b) original silicon relief pillars prior to silver deposition. 91

A.1 Surface Chemistries between surface hydroxyl and 3MPTMS 121

A.2 Schematic depiction of an in-house built pressure device 121

A.3 Micrographs (AFM, b, SEM, a) representing non-optimal conditions imprinting on (a) PDMS elastomer and (b) SU-8 resist. 122

A.4 Schematic depiction of the procedure for transfer printing metallic nanostructures on a fiber optic facet. 122

B.1 Electron beam lithography and nanotransfer printing created nanoarrays: (a) 45° tilted view of fluoropolymer coated stamp, (b) top-view of the stamp after vapor deposition of 30 nm gold, (c-f) different size and spacing gold arrays tranfer printed on quartz surfaces. 124

B.2 Silver nanopatterns imprinted on quartz surface without any surface modification of a substrate (a-c); and gold nanopatterns on quartz surface treated with mercaptosilane griping reagent. 124
B.3 SEMs of transfer printed nanowire sensors: (a) Nanowire sensor array, (b) 12 nm wide (CAD design) connecting wire, (c) 24 nm wide (CAD design) connecting wire, (d) 32 nm wide (CAD design)connecting wire. 125
B.4 SEMs of various nanostructured devices fabricated via nTP: (a) Nanoaggregates of random morphology nanoparticles cloned on large UT pattern, (b) palladium nanoring array, (c) Planer nanogap gold electrode, (d) Just-touching dimer nanoparticles. 126

Nomenclature

α	Molecular polarizability
$\epsilon(r)$	relative dielectric function
μCP	Micro contact printing
μ	Dipole moment
ν	Incident frequency
$\nu^{'}$	Raman frequency
E	Initial energy of a scattered molecule
$E^{'}$	Final energy of a scattered molecule
E_0	Amplitude of electromagnetic wave
h	Planck's constant
r	Bond length
r_{eq}	Bond length at equilibrium
r_{max}	Bond length at maximum separation
$Re(\epsilon(r))$	Real dielectric function
3MPTMS	3-mercaptotrimethoxysilane

AEF	Analytical enhancement factor
AFM	Atomic force microscope
AgPPF	Silver modified polypropylene filter
ATP	Aminothiophenol
BT	Benzenethiol
C_{RS}	Concentration of analyte for Raman
C_{SERS}	Concentration of analyte for SERS
CARS	Coherent anti-stokes Raman Scattering
CCD	Charge coupled device
CE	Chemical enhancement
CSRS	Coherent stokes Raman Scattering
CT	Charge transfer
DL	Detection limit
E_L	Local electric field
EBL	Electron beam lithography
EDC	Endocrine disrupting chemical
EF	Enhancement factor
EF_{max}	Maximum enhancement factor
EM	Electromagnetic
HOMO	Highest occupied molecular orbital

HPEDC	High performance extraction disc cartridge
HRS	Hyper Raman Scattering
I_{RS}	Raman intensity
I_{SERS}	SERS intensity
IRS	Inverse Raman Scattering
LSPR	Localized surface plasmon Resonance
LSPs	Localized surface plasmons
LUMO	Lowest unoccupied molecular orbital
M_L	Local electric field enhancement
M_{Rad}	Radiation enhancement factor
MDH	Mitoxanthrone dihydrochloride
N_{SERS}	Average number of molecules adsorbed on volume V
N_{Vol}	Average number of molecules in a scattering volume V
NIR	Near infrared
NSL	Nanosphere lithography
nTP	Nanotransfer printing
P_0	Power radiated by Raman dipole in a free space
P_{rad}	Power radiated by Raman dipole in presence of metallic objects
PABA	*p* aminobenzoic acid
PARS	Photoacoustic Raman Scattering

PDMS	Polydimethylsiloxane
PMMA	Polymethyl methacrylate
PPF	Polypropylene filter
R6G	Rhodamine 6G
RIE	Reactive ion etching
RIKES	Raman-induced Karr effect Scattering
SAM	Self-assembled monolayer
SEM	Scanning electron microscope
SERS	Surface-enhanced Raman scattering
SMSERS	Single-molecule SERS
SRS	Stimulated Raman Scattering
SSEF	SERS substrate enhancement factor
STT	Sample translation technique

Chapter 1

Introduction

This dissertation is concerned about the development of surface enhanced Raman spectroscopy (SERS) substrates with the potential applications in analytical detection. Current work also deals with the photonic studies of arrays of metallic nanoparticles in understanding SERS effect.

The structure of this dissertation is set out such that a general overview of the Raman effect is provided (chapter 1) and a brief overview of SERS mechanism and substrate design is explained (chapter 2). This is followed by a brief discussion of various nanolithographiphic techniques currently used in the fabrication of reproducible SERS substrates (chapter 2). SERS based studies of possible endocrine disruptors (phytochemical estrogens, (chapter 3)), and uranyl species (chapter 4) are presented separately. Finally, discussions of nanotransfer printing (nTP) approach to incorporate nanofeatures on different dielectric materials and its promises in SERS research is elaborated (chapter 5).

This chapter introduces Raman spectroscopy and explains the need of SERS. Moreover, it also introduces various types of existing linear and non-linear Raman spectroscopy.

1.1 A brief introduction to Raman spectroscopy

1.1.1 The discovery

Raman scattering, what we call today, was first theoretically predicted by an Austrian physicist A. Smekal (1923), and later on experimentally observed by Indian physicist C.V. Raman (1928) [1]. The effect was discovered using a very rudimentary optical set up, i.e. sunlight as a light source, telescope, color filters, and observer's eye as a detector [2]. Professor Raman was awarded the Nobel prize in physics in 1930 for his discovery.

Originally, the phenomenon was measured on a number of highly concentrated pure organic solvents. Hence, the effect was visible to eyes. However, for dilute solutions or solids, the effect is rather weak. Therefore, many applications of Raman scattering were delayed for several decades until the discovery of the laser, along with development of more efficient detection systems (e.g. notch filter, holographic gratings, high throughput monochromators, photomultipliers, multi-channel charge-coupled devices etc.). It is, therefore, now possible to observe Raman scattering from materials that were almost impossible just a few decades ago.

1.1.2 Classical theory and mathematical explanations

When a beam of monochromatic exciting radiation interacts with matter, there occurs both elastic and inelastic scattering. Most of the scattered radiation has the same energy as the incident photons (Rayleigh scattering) while a small fraction of scattered radiation has either higher or lower energy than the incident photons (Raman scattering). In Raman scattering, due to light-matter interaction, the energy is either given or taken away from the molecule. According to the conservation of

energy:

$$h\nu + E = h\nu^{'} + E^{'} \tag{1.1}$$

$$or, \qquad \Delta E = h(\nu^{'} - \nu) \tag{1.2}$$

where ν and $\nu^{'}$ are incident and scattered frequencies respectively. Similarly, E and $E^{'}$ are initial and final energies of a scattered molecule.

On the basis of above equations, the scattered radiation can be classified as:

(a) ΔE=0, when $\nu = \nu^{'}$ **Rayleigh scattering**

(b) ΔE<0, when $\nu > \nu^{'}$ **Stokes scattering**

(c) ΔE>0, when $\nu < \nu^{'}$ **Antistokes scattering**

The schematic energy level diagram for Rayleigh, Stokes, and Antistokes scattering is shown in Figure 1.1

If a molecule is placed in an electric field, electrons and nuclei get displaced. As a result an induced dipole moment is produced in a molecule; and a molecule is said to be polarised. If E is the strength of electric field and μ is the magnitude of induced dipole moment, then

$$\mu = \alpha E \tag{1.3}$$

where α is the polarizability of the molecule. The electric field strength of an electromagnetic wave of frequency ν is expressed as

$$E = E_0 cos\ 2\pi\nu t \tag{1.4}$$

where E_0 is the amplitude of the electromagnetic wave. From equation (1.3)

$$\mu = \alpha E_0\ cos\ 2\pi\nu t \tag{1.5}$$

Equation (1.5) implies that interaction of electromagnetic radiation of frequency ν induces a molecular dipole moment which oscillates with the same frequency.

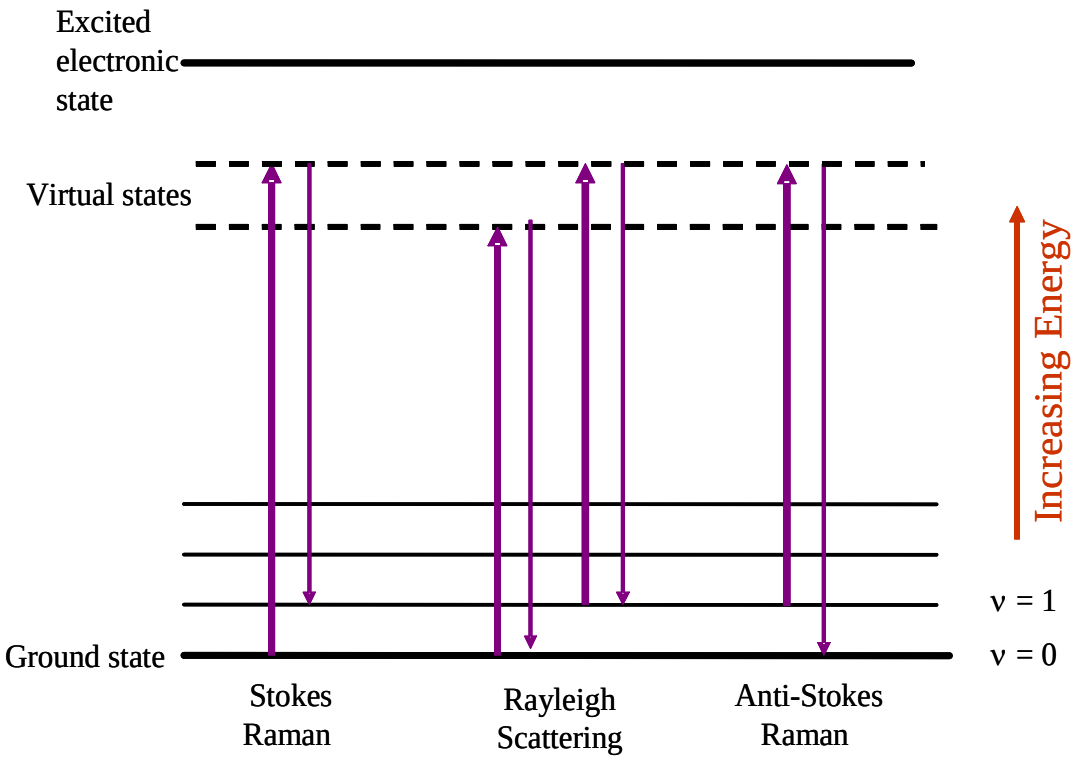


Figure 1.1: Schematic of the origin of Rayleigh and Raman scattering

However, the polarizability changes with small displacement from equilibrium position (i.e. molecular vibration), and is given by

$$\alpha = \alpha_0 + (r - r_{eq})\frac{\partial \alpha}{\partial r} \tag{1.6}$$

where α_0 is equilibrium polarizability; r_{eq} and r are bond lengths at equilibrium position and at any instant, respectively. If a molecule executes simple harmonic motion, the displacement can be represented as

$$r - r_{eq} = r_{max}\ cos\ 2\pi\nu_j t \tag{1.7}$$

where ν_j is the vibrational frequency of a molecule and r_{max} is the maximum separation distance between atoms relative to their equilibrium position. Substituting equation (1.7) into equation (1.6) gives

$$\alpha = \alpha_0 + (\frac{\partial \alpha}{\partial r})r_{max}\ cos\ 2\pi\nu_j t \tag{1.8}$$

Substituting equation (1.8) into equation (1.5) gives

$$\mu = \alpha_0 E_0\ cos\ 2\pi\nu t + E_0 r_{max}(\frac{\partial \alpha}{\partial r})cos\ 2\pi\nu_j t\ cos\ 2\pi\nu t \tag{1.9}$$

$$\mu = \alpha_0 E_0\ cos\ 2\pi\nu t + \frac{E_0}{2} r_{max}(\frac{\partial \alpha}{\partial r})cos[2\pi(\nu - \nu_j)t] + \frac{E_0}{2} r_{max}(\frac{\partial \alpha}{\partial r})cos[2\pi(\nu + \nu_j)t] \tag{1.10}$$

The first term in equation (1.10) represents Rayleigh scattering and occurs at the excitation frequency ν. The second and third terms correspond to stokes $(\nu - \nu_j)$ and antistokes $(\nu + \nu_j)$ scattering. In both inelastic scattering, the excitation frequency has been modulated by the vibrational frequency of the bond.

1.1.3 Instrumentations

In Raman experiments, the sample is irradiated with monochromatic light and the scattered light is traditionally observed at right angles to the incident radiation. However, in modern confocal Raman microscopes, the scattered signals are recollected by a microscope objective in a 180° geometry. Regardless, modern instruments mainly consists of four components: a laser source, a sample-illumination system, holographic optics, and a suitable spectrometer with a detector.

Since the intensities of scattered radiation are very weak, an extremely intense source of radiation is needed. In a traditional spectrometer, a collection of few mercury lamps were used to surround sample tube. However, with the advancement in laser technology laser sources have become the standard irradiation system in modern Raman spectrometers. The most commonly used laser sources in Raman applications are Argon ion (488/514 nm), Krypton ion (530.9/647.1 nm), Helium/Neon (632.8 nm), Diode lasers (782/830 nm), and Nd/YAG (1064 nm) [3]. Since the Raman scattering intensity varies as the fourth power of the laser frequency, short-wavelength Argon and Krypton ion lasers were integrated in the spectrometer until last two decades. In general, these sources can generate Raman signals that are up to three times more intense than those produced with the corresponding He/Ne laser [3]. However, intense incident radiation may result in higher fluorescence emission and photodecomposition of the sample. To minimize the above mentioned effects while keeping a reasonable Raman sensitivity, He/Ne source has been extensively practised. Most recently, near infrared (NIR) laser sources such as diode lasers and Nd/YAG laser are in extensive use and are very advantageous in dramatically reducing fluorescence and photodecomposition of the sample. These lasers have gained additional attention due to the suitability for the excitation of localized surface plasmons on gold nanoparticles for surface-enhanced Raman applications [4]

For the study of Raman effect the type of sample-illumination system to be used depends on the intensity and nature of radiation source. The study of Raman spectra

of gases requires sample holders which are bigger in size than those for liquids. In a confocal spectrometer, a sample holder can also be a simple capillary tube containing the liquid or powdered solid sample. Since water gives relatively weak Raman signal, it is preferentially used as a solvent.

There are several holographic filters or wavelength selectors used throughout the laser path. At first, a narrow band-pass filter (interference/absorption filter) is placed in between a source and a sample to isolate a single exciting line. Another most important filter used in the Raman spectrometer is a holographic notch filter. The notch filter provides efficient, narrow band width rejection of laser line. It transmits less than 0.5% of the backscattered laser line while allows more than 90% of the remaining frequencies to reach the detector.

Charge coupled devices (CCDs) are the most commonly used detectors in Raman systems. The CCD consists of a series of silicon photosites (elements or pixels) in a two dimensional array known as a chip [5]. Each photosite has two conductive electrodes separated by thin silica dielectric layer and each pixel is also surrounded by a non-conductive barrier. When photon strikes on a chip, it induces a charge build-up on the surface of irradiated pixel, which in turn is stored in a capacitor or potential well located below the electrodes. Once the analytical signals are collected, the number of electrons generated in each pixel or data can be recorded by the control electronics and computer to give the acquired Raman spectrum [6]. CCDs have an ability to simultaneously collect the entire spectrum and are also over two orders of magnitude more sensitive (high quantum efficiency and low noise) than photodiode array detectors. Such traits make CCDs an almost ideal detector for sensing weak Raman signal.

Shown in Figure 1.2 is a diagram of the confocal Raman instrument employed in the studies conducted and presented throughout this dissertation. All spectra were collected using JY Horiba Labram spectrograph. Confocal Raman systems are useful for the efficient rejection of stray light and fluorescence. They offers several other advantages such as, low sample requirements, high throughput, good

collection efficiency, ability to collect signals from micron size samples with good lateral resolution [7].

1.2 Raman terminology (linear and non-linear)

As explained earlier, Raman scattering arises from an induced oscillating polarization in the sample due to light-sample interaction. Conventional Raman scattering is a linear process and the induced sample polarization depends on the first power of the electric field strength of the incident radiation. All other techniques that depend on the second and higher order electric field strengths are termed nonlinear Raman techniques. Nonlinear Raman scattering includes stimulated Raman scattering (SRS), hyper Raman scattering (HRS), coherent anti-Stokes Raman scattering (CARS), coherent Stokes Raman scattering (CSRS), stimulated Raman gain (SRG), inverse Raman scattering (IRS), photoacoustic Raman spectroscopy (PARS), and Raman-induced Kerr effect spectroscopy (RIKES). Energy level diagrams of some Raman techniques are shown in Figure 1.3. More technical aspects of nonlinear Raman can be found in reference [8].

Resonance Raman scattering occurs when the frequency of the laser excitation corresponds to the energy of an electronic transition of the molecule. Raman signals thus obtained have intensities $10^2 - 10^6$ greater than normal Raman. Both linear and nonlinear Raman techniques can benefit from resonance enhancement. Thus lower limit of detections are a characteristics of the resonance Raman. However, it is not always possible to operate the technique in the resonance region of all samples. Resonance Raman is different from both normal Raman and fluorescence. When compared to fluorescence, resonance Raman is not preceded by radiationless relaxation to the vibrational ground state of the excited electronic state while that is the case in fluorescence (Figure 1.3h). A fluorescence process requires more than nanoseconds while Raman process is completed within picoseconds or less.

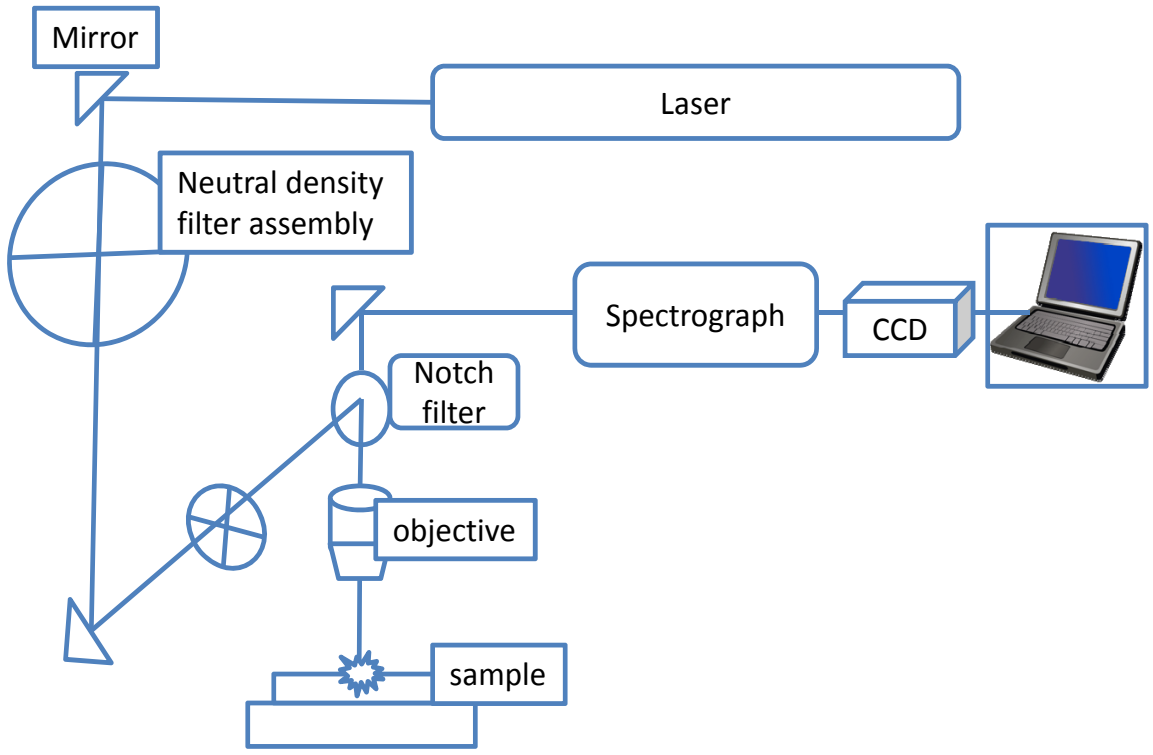


Figure 1.2: Schematics of JY Horiba LabRam spectrometer used in the current study

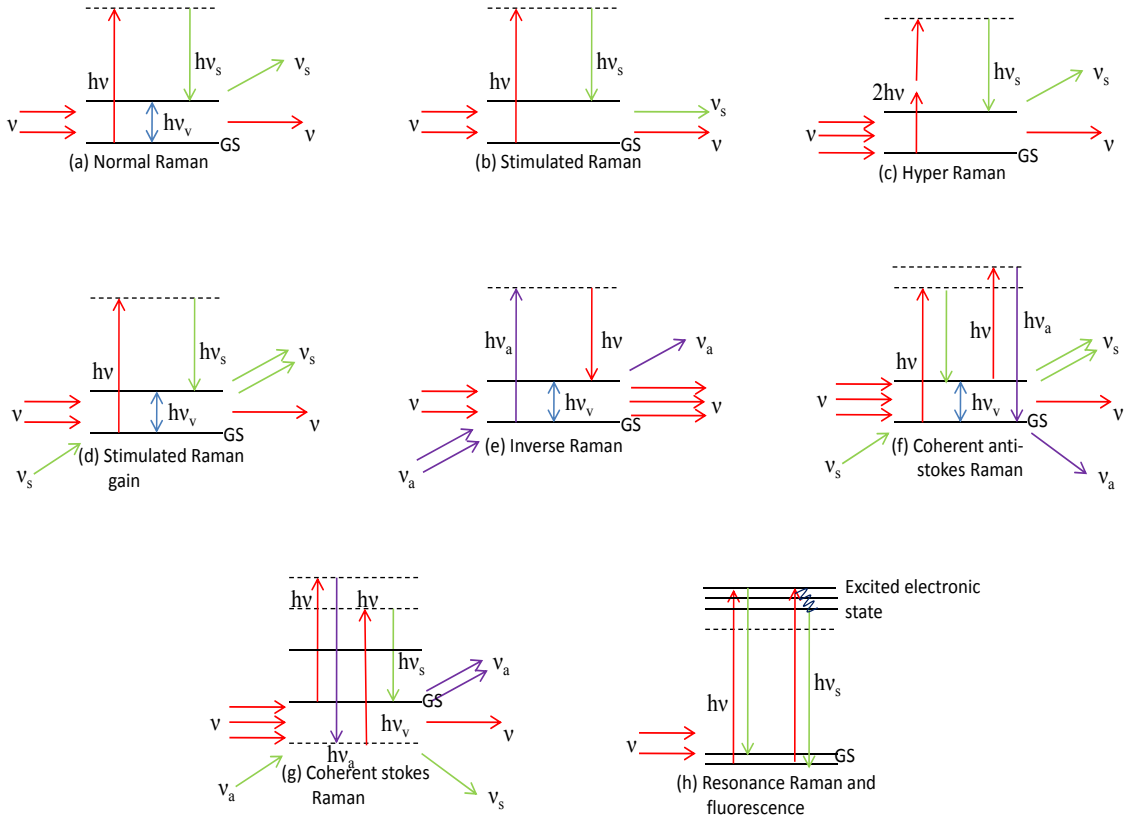


Figure 1.3: Quantum diagram of the linear and nonlinear Raman processes. Each photon is represented by an arrow; ν = laser frequency, ν_s = stokes frequency, ν_a = antistokes frequency, ν_v = vibrational frequency, and GS = Ground state

Currently there is a great deal of interest in the surface-enhanced Raman scattering (SERS) technique and also is the major focus of this dissertation. SERS is typically observed from molecular species in close proximity to nanostructured plasmonic surfaces. The technique is of particular interest in the analytical chemistry community, as the signals observed from SERS have been reported to have 12 or more orders of magnitude enhancement of normal Raman signals [9]. However, the are of SERS itself is multidisciplinary in nature and addresses *physical* (electromagnetic theory of plasmon resonances), *chemical* (molecular adsorption on nanostructured surfaces), *engineering* (SERS substrate fabrication), and *biological* (biomedical applications) studies [4]. A quick overview of SERS is discussed in next chapter.

Chapter 2

A Quick Overview of Surface-Enhanced Raman Scattering and Related Topics

SERS is all about amplifying Raman signals, almost exclusively from molecules, by several orders of magnitude. Mainly, the enhancement is due to the electromagnetic interaction of light with metallic nanoparticles, which produces strong electromagnetic fields localized around nanoparticles through plasmon resonances. Molecules attached or in close vicinity to the nanostructured metallic surfaces can experience this intense plasmonic field. Accordingly, the Raman signals of molecules are amplified.

This chapter discusses mechanisms, characteristics, and applications of SERS. Moreover, different classes of SERS substrates will be introduced. This is followed by a brief discussion of nanolithographic techniques used in engineering SERS substrates.

2.1 The discovery of SERS

The enhanced Raman signal of pyridine adsorbed on roughened electrochemical silver electrode, observed by Fleischmann et. al in 1974 [10], is considered to be the first

observation of the SERS effect. The effect was observed as the researchers were trying to implement Raman spectroscopy as a possible means to observe molecules on surfaces at a monolayer coverage. Fleischmann et al., in their original paper, interpreted the amplified Raman signal of pyridine as an outcome of increased surface area caused by the roughening of silver electrodes. However, there were many unanswered questions regarding this simple hypothesis. Later on in 1977, two independent research groups, *Jeanmarie* and *Van Duyne* [11] and *Albrecht* and *Creighton* [12] documented that the observed Raman enhancement could not be accounted for by increased surface area, instead other mechanisms exist. Since then several enhancement mechanisms were proposed in the early days of SERS, however only two mechanisms are now broadly accepted, i.e, Electromagnetic (EM) theory and Chemical Enhancement (CE) theory. CE theory depends on the chemical interaction between probe molecules and the noble metal and is said to contribute only a maximum of about 2-3 orders of magnitude [13]. The dominant EM theory, on the other hand, is based on the collective oscillation of free electron density generating localised surface plasmons (LSPs) and can contribute ten or more orders of magnitude enhancement [14].

2.2 SERS enhancement mechanisms

As stated earlier, SERS enhancements are mainly attributed to the electromagnetic and chemical effects. In theory, EM enhancement is analyte independent while CE is probe-dependent and requires some sort of chemical interaction to the metal surface.

2.2.1 Electromagnetic Enhancements

The majority of the overall SERS enhancements is due to EM enhancement mechanism and is a direct consequence of roughness present on the noble metal

surfaces. In order to understand the EM enhancement mechanism, it is important to recall the phenomenological approach to Raman scattering.

When monochromatic radiation of frequency ν and electric filed E interacts with a molecule, it induces a Raman dipole oscillating at a frequency ν_R

$$\mu_R = \alpha_R E \tag{2.1}$$

The oscillating Raman dipole radiates a power proportional to $|\mu_R|^2$ at frequency ν_R and is the frequency detected as Raman signal in far-field.

The same phenomenological description can be applied to SERS. However, the presence of roughened metal surface alters the effects, such as:

(a) The electromagnetic field at the metallic surface can be dramatically increased and may results in a possible local field enhancement.

(b) The radiation properties of the Raman dipole, μ_R, is affected by the metallic environment and may results in a possible radiation enhancement.

Therefore, EM enhancement mainly concerns about understanding the two effects listed above.

Local field Enhancement

When electromagnetic radiation impinges on a suitable metal surface (that possess a negative real and small positive imaginary dielectric constant), the electromagnetic field in the vicinity of metallic surfaces get strongly modified. This is due to the coherent oscillation of free electrons generating *surface plasmons*. Surface plasmons can be of two types, surface plasmon polariton (or propagating plasmon)- propagates in $x-$ and $y-$ directions along the metal-dielectric interface [15, 16], or localized surface plasmon- localized on the surface of a nanoparticle (Figure 2.1) with a frequency known as the localized surface plasmon resonance (LSPR) [17, 18].

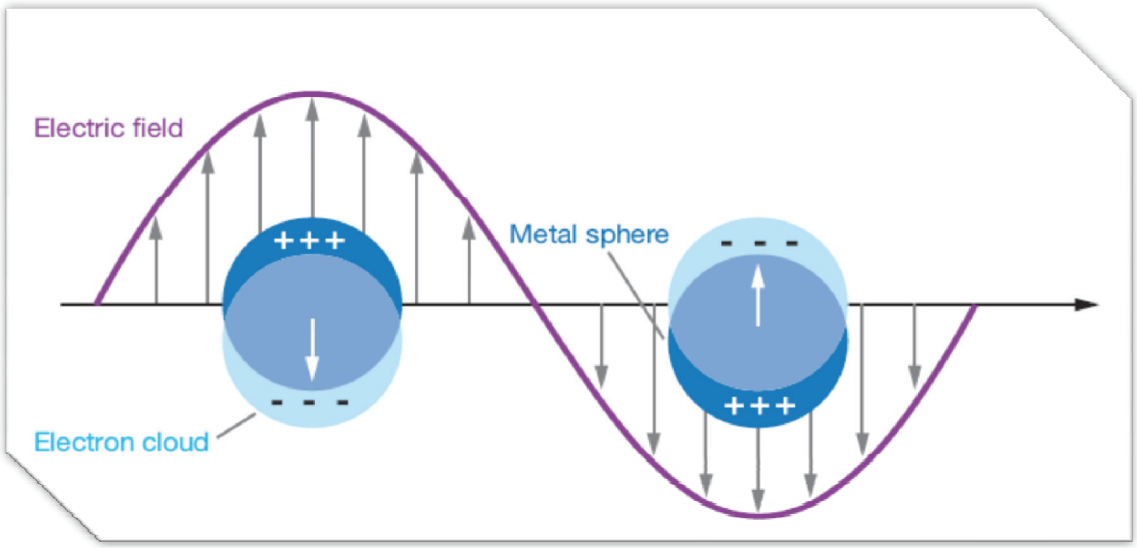


Figure 2.1: Schematics of the origin of electromagnetic field enhancement mechanism in SERS

SERS is benefited from LSPR and the LSPs or local field on the metallic object at the molecular position, E_L, could be different from incident field, E, in terms of both magnitude and orientation. Usually, the magnitude of $|E_L|$ can be much larger than $|E|$. The local field induces a Raman dipole

$$\mu_R = \alpha_R E_L(\nu_L) \tag{2.2}$$

Therefore, the Raman dipole is enhanced by a factor of $|E_L(\nu_L)|/|E|$. If such Raman dipole radiates in free-space (i.e., in absence of metallic environment), the radiated energy which is proportional to $|\mu_R|^2$, would enhance by a factor

$$M_L(\nu_L) = \frac{|E_L(\nu_L)|^2}{|E|^2} \tag{2.3}$$

$M_L(\nu_L)$ is the local electric-field enhancement factor and characterizes the enhancement of the electric field intensity, but ignores any changes in the electric field polarization.

Radiation Enhancement

In SERS, Raman dipole radiates in presence of metallic objects, unlike in free-space. Therefore, the presence of metallic environment significantly alters dipole radiation as in the case of incident electric-field. It is known that the total power radiated by the dipole, P_{rad} can be either quenched or enhanced (relative to that in free space, P_0) depending on the relative dielectric function $\epsilon(r)$ of the object, its geometry, and the dipole position, orientation and its emission frequency, ν_R. For example, a small quenching is observed for a dipole parallel to the surface of non-absorbing dielectric sphere, like glass, with $\epsilon(r) > 1$. For objects having negative real dielectric function, $Re(\epsilon(r)) < 0$, the radiated power is strongly enhanced. The large enhancement in the radiated power is due to coupling to the LSPR of metallic objects [4]. Therefore, the radiation enhancement factor is given by

$$M_{Rad} = \frac{P_{Rad}}{P_0} \tag{2.4}$$

$|E|^4$ Approximation

Considering local electric-field enhancement and radiation enhancement, EM enhancements of single-molecule SERS (SMSERS) can be simply expressed as [4]

$$Enhancement factor(EF) \approx M_L(\nu_L) M_{Rad}(\nu_R) \tag{2.5}$$

$M_L(\nu_L)$ can be calculated by solving the electromagnetic problem under specific external excitation conditions with an incident field, E, which yields local-field everywhere. However, estimation of $M_{Rad}(\nu_R)$ is a rather difficult task. For this, it is necessary to solve the electromagnetic problem of dipolar emission, instead of external excitation, which itself is very complicated. To avoid these complications, it is often assumed that local electric-field enhancements and radiation enhancements

are approximately equal. Hence, SERS enhancements can be expressed as

$$EF \approx M_L(\nu_L)M_{Rad}(\nu_R) \approx \frac{|E_L(\nu_L)|^2}{|E|^2}\frac{|E_L(\nu_R)|^2}{|E|^2} \tag{2.6}$$

This equation provides a very simple way of estimation SERS enhancement factor from the calculation of local field at the excitation and Raman frequencies. In addition to this, in many cases, the Raman shift is small (or the plasmon width is often large compared to the Stokes shift), and an additional approximation can be made, i.e., $\nu_R \approx \nu_L$. This results into even more famous expression of the SERS enhancement

$$EF \approx \frac{|E_L(\nu_L)|^4}{|E|^4} \tag{2.7}$$

In conventional SERS, EF is averaged over the surface area of the particles where molecules can adsorb to generate the observed enhancement factor $|EF|$ and is said to be *average EF*, while in *single-molecule EF* it is the maximum enhancement EF_{max} and represents the enhancement only at specific positions on the substrate. Since EF_{max} applies only to one or a few specific regions of a SERS substrate, it is important to note that average EFs are typically several orders of magnitude less than single-molecule EFs.

2.2.2 The Chemical Enhancement

Although the existence and a definition of CE are a subject to controversy [19], it is believed that, in SERS, a second enhancement mechanism (multiplicative when co-existing) operates independent of EM enhancement. It is almost impossible to separate these effects from a system that supports EM enhancement. Nevertheless, several efforts have been made in understanding the existence of CE [13, 20–24]. CE mechanism is viewed as a resonance Raman mechanism and is attributed to the modification of electronic polarizability of the adsorbate due to the formation of

metal-adsorbate complex. The mostly accepted explanation of CE is a charge-transfer (CT) mechanism [4, 25].

The adsorption of analyte on the metal surface results into the formation of metal-adsorbate complex. Due to direct covalent bonding of adsorbate to the metal surface (chemisorption), a new electronic states arise and serve as resonant intermediate states. In other words, the highest occupied molecular orbital (HOMO) and the lowest unoccupied molecular orbital (LUMO) of the adsorbate are symmetrically disposed in energy with the Fermi level of the metal. In this case, CT excitations occur from Fermi level to LUMO and retro-donation of electron from HOMO to Fermi level of the metal. Under certain conditions, the laser energy can also be directly in resonance with the electronic excitation of the metal-adsorbate complex. The process descriptions are summarized in Figure 2.2.

There is another more sophisticated photo-driven CT process between adsorbate and metal, and is arguably one of the clearest experimental proof of the existence of non-negligible chemical enhancement in SERS [26, 27]. This photo-driven CT process is pronounced when the energy difference between Fermi level of the metal and HOMO or LUMO matches the laser frequency. Under such conditions, a CT mechanism between the HOMO and unoccupied energy states above Fermi level or the LUMO and occupied energy states below Fermi level can be activated. Xie et al. have verified this photo-driven CT processes in Cobalt/Pyridine system by obtaining Raman intensity-potential profiles by changing incident photon energy. It was observed that on increasing laser wavelength, the peak potential shifted to more negative potential in order to match the energy of charge transfer with the incident laser frequency [27].

2.2.3 Analytical/Substrate Enhancement Factors

Although it is very difficult to identify the exact origin of enhancement factors in most of the SERS experiments (as EM and CE enhancements exist together), it is not

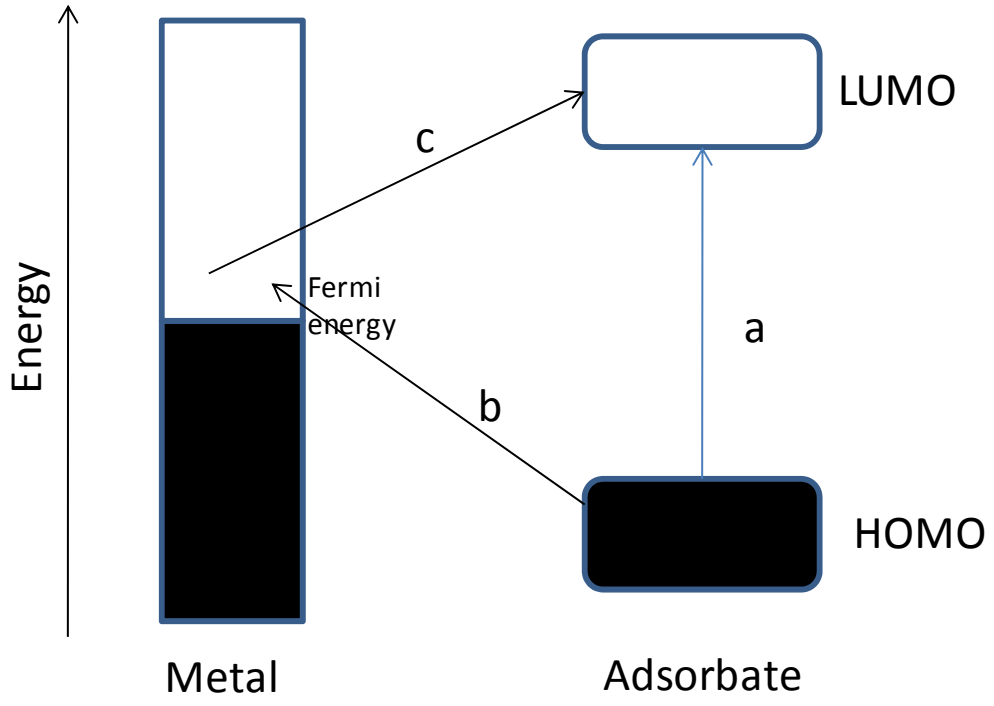


Figure 2.2: Schematics of the origin of charge-transfer mechanism in SERS

important to define them in any analytical measurements. For simplicity, researchers sometime use analytical enhancement factor (AEF) given below

$$AEF = \frac{I_{SERS}}{I_{RS}} \frac{C_{RS}}{C_{SERS}} \tag{2.8}$$

Where I_{RS} is the Raman signal of an analyte at concentration C_{RS}. Similarly, I_{SERS} is the SERS signal measured for same analyte at concentration C_{SERS}. The definition of AEF has made the assumptions that I_{RS} or I_{SERS} scales linearly with incident power density and the concentration of analyte C_{RS} or C_{SERS}. However, the important drawback of the above equation is that it ignores the fact that SERS is a surface spectroscopy and only the adsorbed species contributes on SERS signal. To solve this problem, a following definition of SERS substrate enhancement factor (SSEF) has been widely used

$$SSEF = \frac{I_{SERS}}{I_{RS}} \frac{N_{Vol}}{N_{Surf}} \tag{2.9}$$

Where $N_{Vol} = C_{RS}V$ is the average number of molecular in the scattering volume V, and N_{SERS} is the number of adsorbed molecules on the optically probed SERS substrates. This expression is considered as the best estimate of average SERS EF for a given substrate and has been extensively used in SERS experiments [4, 28–30].

2.3 Applications of SERS

SERS can be approximately considered as Raman spectroscopy with improved sensitivity. Since the Raman technique provides a unique "fingerprint spectrum" of a molecule, the technique is more specific and valuable for its structural information. However, due to the weak signal intensity conventional Raman has lagged behind other analytical techniques like fluorescence. With the gain in Raman intensity provided by SERS, the latter can be used in a variety of applications (already exploited by Raman) with improved sensitivity or limit of detection. In addition

to the improvement on the conventional Raman technique, SERS can also be applied to the system that could not be envisaged with conventional Raman. The potential applications of SERS are in the field of analytical chemistry, biochemistry, forensic sciences, environmental and nuclear sciencs, etc. The technique has been successfully implemented for both trace detection of chemicals (drugs, explosives, environmental contaminations etc.) and sensing and monitoring of biofluids at higher concentrations [31–39]. Moreover, the technique has been implemented in several other applications, such as identification of dyestuffs for ancient paintings and medieval manuscripts [40–42], tissue imaging [43], protein detection [44–46], etc.

SERS is now extensively used in a wide range of scientific areas. As far as applications are concerned, SERS is taken as a big competitor to fluorescence spectroscopy [4]. Nevertheless, both techniques have pros and cons. Regardless, SERS has additional applications such as, tools to study surface plasmon resonances, adsorption properties of analyte, surface chemistries, etc, which could not have been envisaged by conventional Raman or fluorescence spectroscopy.

2.4 SERS substrates

Any nanostructured metallic platform that supports plasmon resonance and amplifies Raman signals to some extent are generally denominated as "SERS substrates". SERS substrates can be classified in a number of ways. Herein, it is classified into two broad distinctions:

(a) Random morphology SERS substrate- includes roughened electrodes, metallic silver & gold colloids, metal-island film on planer substrate, and other related substrates.

(b) Ordered or periodic or uniform planer metallic SERS substrates- includes arrays of regular morphology metallic nanotextures created on planer substrates using nano-lithography and related techniques.

2.4.1 Random morphology SERS substrates

Random morphology SERS substrates are characterized as having inhomogeneous textures and are typically difficult (almost impossible) to fabricate reproducibly. Roughened electrodes are the most primitive SERS substrates and was discovered by Fleischmann et al [10]. These substrates are typically created by running the redox cycle in an electrochemical cell containing metallic salt solution. Such substrates have gained popularity due to an ability to adjust electrode potential to understand the charge transfer phenomenon between adsorbate and metallic surface [26, 27]. Regardless, the importance of this substrate is decreasing substantially due to relatively low enhancement factors.

Another group of SERS substrates that occupied much attention in the early studies are vacuum deposited metal island films on various substrates. Substrates can be planer surfaces like glass, quartz, silicon wafer or polydimethylsiloxane (PDMS) or nanoparticles (silica beads, polystyrene, etc.) embedded surfaces [47–51]. These substrates are relatively easy to prepare and high in purity. Substrates are usually created by vapor deposition of pure gold or silver particles mediated by electron-beam or thermal energy.

Among the random morphology SERS substrates, silver or gold colloids are the most common substrates used in both early and more recent studies. Since colloids are easy to produce in a laboratory and tend to generate large enhancement factors, most researchers are still involved in colloid-based SERS rather than more sophisticated substrates. Metallic colloids are also of historic significance related to SERS development, as the first SMSERS detection were reported using colloid substrates [9, 52]. Metallic colloids are typically produced by a reduction reaction in solution. The existence of colloidal particles in solution is attributed to the stabilization caused by coulombic or steric repulsions among particles. Therefore, it is important to add stabilizing agent in a reaction mixture to prevent colloids from excessive aggregation and precipitation. However, in the most common SERS colloid,

i.e., citrate-reduced colloid, sodium citrate acts both as a reducing and stabilizing agents.

Citrate-reduced (or Lee-&-Meisel) silver colloid is a grey-yellow solution and has a UV/Vis absorption maximum at around 400-430 nm. The shape and size of the sol particles are highly disordered. However, the mean particle size is reported to be 60 nm in diameter. Similarly, citrate-reduced gold colloid is a wine-red solution with UV/Vis absorption maximum at around 520-530 nm. Several other chemical routes can be utilized for the production of silver or gold colloids. Colloids produced by alternative reducing/stabilizing agents usually have different optical properties than previously described one. The most common alternative of citrate reducing agent is borohydride and has been broadly used in SERS research. However, borohydride-reduced colloids are relatively less stable than citrate-reduced one. Moreover, in some cases, controlled morphology metallic colloids (i.e., cubes, rods, triangles etc.) can be produced by careful reduction protocol [53]. Among the groups of metallic colloids, by far, the evidence of SMSERS comes from the Lee-&-Meisel type silver colloidal particles that possess some "hot-spots" [9, 37, 52, 54–56]. Although most of the researchers in the field of SERS admire the ability of SERS to measure single molecules in a variety of experimental situations, the path to SMSERS is not free of controversy. There is still a debate as to whether or not the aggregates or "hot-spots" themselves cause the amplification of Raman signal or if those aggregates possess more than average number of analytes. Researches have also shown that hot-spots can contain a wide range of particles [37, 57]. Nevertheless, most recently Vanduyne group reported frequency domain existence proof of SMSERS by using two isotopologues of rhodamine 6G, R6G-d_0 and R6G-d_4 [58]. To date, this work is considered to be the most reliable dual analyte single-molecule SERS studies. This is mainly due to the identical Raman cross section, surface chemistry, and unperturbed electronic absorption spectrum of the adsorbate or isotopologues.

In addition, we have extended the scope of random morphology SERS substrate through the development of silver-modified polypropylene filter (AgPPF) substrate.

The significance of this new substrate is discussed in greater detail in separate chapters.

2.4.2 Periodic or uniform planer SERS substrate

Although with metallic colloidal particles, it is possible to accomplish SERS spectra of a single molecule, it is often challenging to reproduce or routinely deliver such a high performing SERS feature. To overcome this issue, a few alternatives have been introduced on engineering periodic arrays of metallic nanostructured SERS substrates. Nanosphere lithography (NSL), developed by Vanduyne et al., is the most extensively used nano-fabrication procedure used in understanding SERS phenomena and performing plasmonic based sensing [14]. Electron beam lithography (EBL) is another most widely used conventional nanofabrication technique in designing uniform and controlled morphology SERS substrates [30]. In our current work, non-conventional nanotransfer printing (nTP) technique has been introduced as an effective technique in augmenting and amplifying the utility of EBL for SERS research. A brief discussion of each of these these techniques are provided below.

Nanosphere lithography

NSL is based on the self-assembly of polystyrene nanosphere on a planer surface [59]. The technique has been shown to be reasonably inexpensive and easy to produce nanoparticles array with somewhat controlled shape, size, and spacing. The process begins with the self-organization of size-monodisperse polystyrene nanosphere to form a two-dimensional colloidal crystal depositon mask. Nanosphere solution can be deposited on the desired substrates by drop coating [60], spin coating [59] or thermoelectrically cooled angle coating [61]. The most important requirement for this self-assemby technique is that the nanosphere be able to diffuse freely to reach their minimum energy configuration. For negatively charged substrates like glass or mica, this is often achieved by functionalizing nanospheres with negatively charged

species such as sulphate, carboxylate etc. As the solvent evaporates, nanospheres get closer due to the capillary action and finally forms a hexagonally close-packed pattern or mask on the substrate (Figure 2.3, left). Following the evaporation of metal thin film on NSL mask, nanospheres are lifted-off leaving behind the arrays of metallic nanostructures (truncated tetrahedrons) on the interstitial sites (Figure 2.3, right).

Nanoparticles array created via NSL exhibits UV/Vis extinction band and has been reported that LSPR spectra of NSL-derived nanoparticls can be tuned across the entire visible range [62]. Therefore, the technique is often used to compare theory to experiment studies of the optical properties of nanoparticles [14].

Electron-beam lithography

Another approach to fabricate highly uniform and reproducible planer SERS substrates is EBL (borrowed from semiconductor industry). EBL uses focussed electron beam to create patterns on electron-sensitive resist such as polymethyl methacrylate (PMMA), Zep 520A, etc. Due to the shorter wavelength possessed by energetic electrons (order of 1 Å) it offers higher patterning resolution down to $\approx$ 10 nm [63]. Despite the shorter wavelength of electrons, the limit in the pattern resolution is attributed to the electron scattering in the resist. Therefore, in order to obtain nanopattern with high precision and resolution, it is important to set the parameters (electron gun voltage) so that electron scattering causes minimal resist exposure. With very high energy electrons, the broadening of beam in the resit due to elastic scattering is very small. Instead, the beam diffuses deeply into the resist and hence affects pattering. On the other hand, with very low energy electrons, the electron beam would not be able to scatter over large distances.

A typical EBL system consists of three main components:

(a) an electron gun or electron source that supplies the electrons

(b) a vacuum system or electron column that focuses the electron beam

(c) a computer system that controls the equipment.

EBL is based on the principle that electron-sensitive resists change their properties upon electron exposure. Unlike photolithography, EBL does not need mask, instead a digital image (designed using engineering software such as AutoCAD) is directly patterned on a desired substrate through computer control of the position of the electron beam [64]. An EBL system simply draws the pattern over the resist film using the electron beam as its drawing pen. Thus, EBL systems produce the resist pattern in a serial manner and, hence, has a low throughput (typically an area of $1mm^2$ requires more than an hour writing time) . In our study, we have conjugated EBL with processes like reactive ion etching (RIE) and lift-off to fabricate various nanostructures for SERS detection. Shown in Figure 2.4 (next page) are some EBL/RIE created patterns used in the study. Despite the impressive resolution, EBL has certain limitations in SERS research. The existing pattern resolution of EBL is good enough for the fabrication of isolated particles of different shape and size. However, there still remains challenge in fabricating precisely controlled nanogap of less than 5 nm and is obligatory to understand the gap-plasmon effects.

To augment EBL in SERS research, we have put forwarded an interesting nTP technique that circumvents low throughput and extremely high resolution limitations of EBL in designing SERS substrates.

Nanotransfer printing

nTP is a high resolution printing technique and relies on the interfacial chemistries to control the transfer of thin metal film from "stamp" to a "substrate" [65,66]. The stamps are created either by photolithography or EBL and can be either soft (usually PDMS) or hard (silicon, gallium-arsanide etc.). The technique is purely additive and can pattern complex patterns over the large area in a single step process. nTP is also superior to micro contact printing (μCP), as the former does not suffer from surface diffusion or edge disorder. Moreover, nTP does not require post-printing etching procedure. The process requires the following steps

(a) To create stamp having nanostructured relief pillars

(b) To deposit metal thin film onto the raised features of stamp

(c) To bring stamp into physical contact with with a final substrate

In addition to these steps, surface chemistries play a vital role in transfer printing process. A "releasing" layer is formed on the stamp prior to metal deposition which helps preventing adhesion of metal thin film to the stamp. A "glue" or "griping" layer is formed on the final substrate prior to step (c) which promotes strong adhesion of transfer material onto the substrate of interest. The most commonly use releasing agent is a monolayer of fluorinated silane which reduces the adhesion of transfer metal to the stamp. Both self-assembled monlayer (SAM) or other surface chemistries can act as a "glue" for printing onto final substrates. In our study we used (3-mercaptopropyl)trimethoxysilane (3MPTMS) as a griping reagent to transfer print gold and silver disc arrays onto glass, PDMS, and SU-8 resist (details in chapter 5). Loo et al. have also demonstrated the transfer chemistry of a thin metal bilayer Au/Ti based on dehydration reaction (surface hydroxyl groups on the substrate act as a glue) [66]. Schematic representation of the nTP is depicted in Figure 2.5 (next page).

The resolution of nTP is currently reported to approximately 100 nm [67]. However, the scope of a technique is just limited to the patterning of electronic circuits. This could be possibly due to the ease of transfer process achievable from higher (contact) surface area. In our work, with a few optimization studies, we have successfully demonstrated the transfer printing of an isolated single particle ($\leq$ 150 nm in diameter)that supports plasmonic effects.

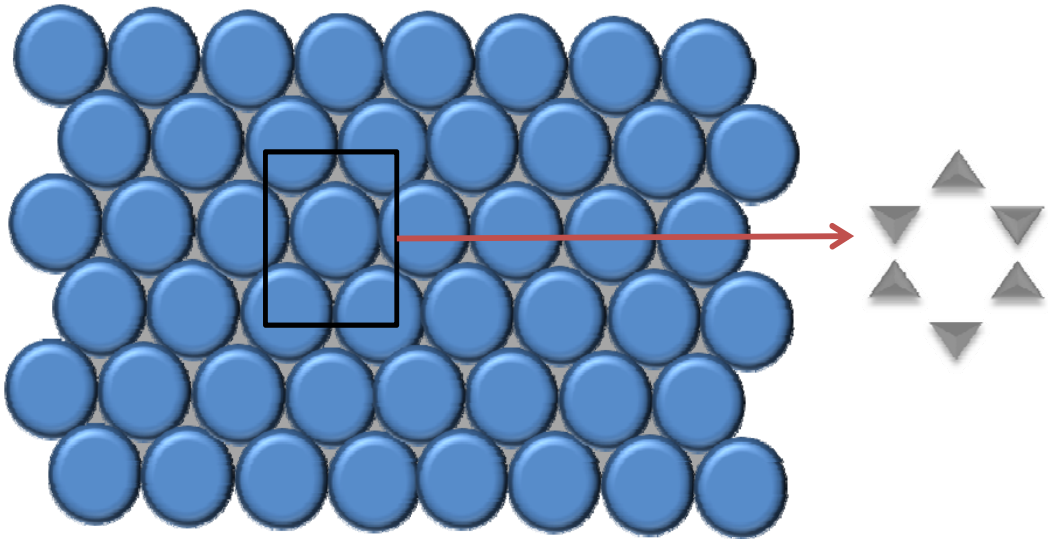


Figure 2.3: Representation of the nanosphere lithography approach for SERS substrate fabrication.

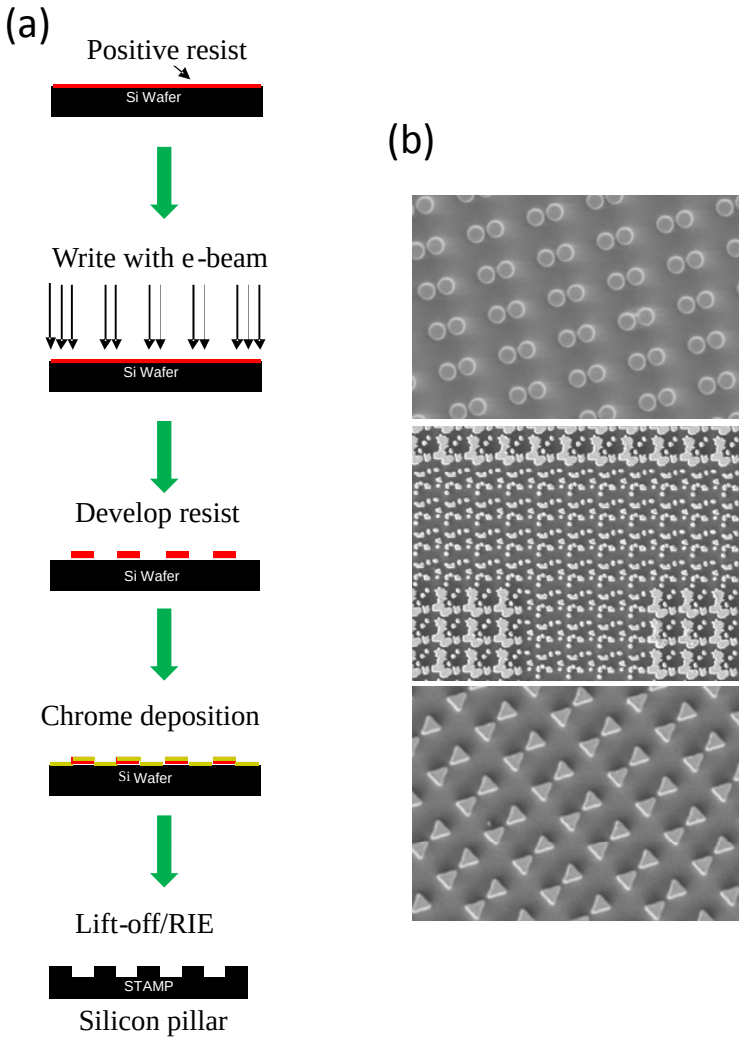


Figure 2.4: Electron beam lithography for SERS substrate fabrication: Schematics of stamp fabrication procedure (left) and scanning electron micrographs of EBL created nanofeatures for SERS studies

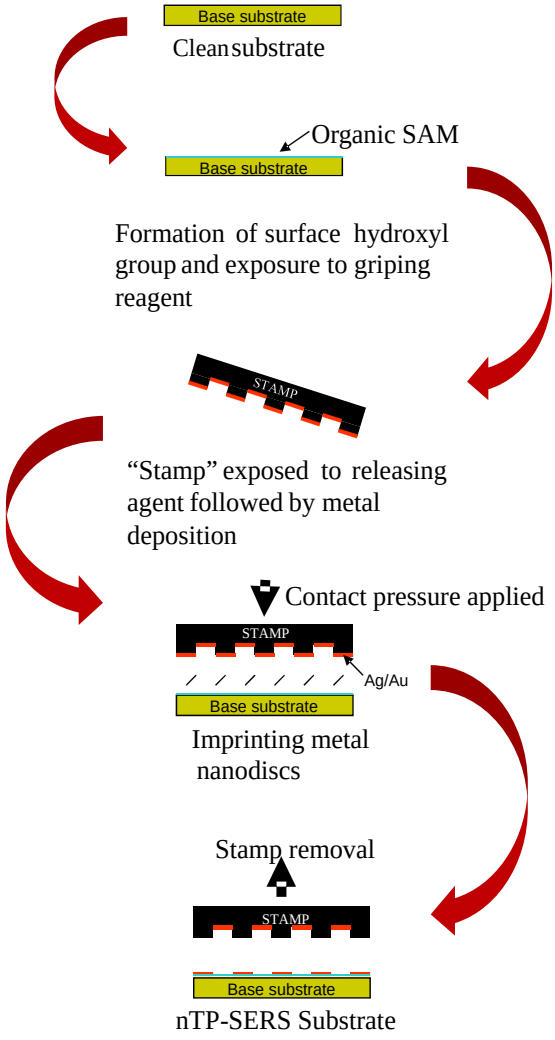


Figure 2.5: Schematic depiction of the nanotransfer printing procedure for the creation of nTP-SERS substrate

Chapter 3

Dual Function Surface-Enhanced Raman Active Extractor for the Detection of Environmental Contaminants

Chapter 3 is an adaptation of a research article *Applied Spectroscopy,* ***2009****, 63, 571-578.* The article describes the development of polypropylene filter based SERS substrate and its application in the detection of possible environmental estrogens.

3.1 Introduction

Artificial and natural organic compounds that continue to be synthesized, used, and disposed are now broadly recognized as environmental contaminants which include pharmaceuticals, surfactants, pesticides, flame retardants, plasticizers, steroids, and other trace organics [68]. The presence of these compounds in the environment has serious impact on humans, wildlife, and aquatic ecosystems. These environmental agents usually mimic or interfere with the endogenous steroid hormones of vertebrates

by interacting with hormone receptors which in turn adversely alters the entire endocrine system [69]. The agents are often classified as endocrine disrupting chemicals (EDCs). This results in abnormal physiological processes and reproductive impairment [70,71], increased incidences of cancer [72], and development of antibiotic-resistant bacteria [73]. Flavonoid phytochemicals are sometimes referred to as environmental estrogens [74] because of their environmental presence and hormone disrupting activity. Isoflavones such as genistein and daidzein are attributed to premature labor upon long exposure [75]. Several other estrogenic and antiestrogenic activities of flavonoids such as, apigenin, genistein, flavone, luteolin etc. can be found elsewhere [74, 76–78]. Environmental occurrence of these pollutants are at very low concentration levels, sometimes ranging from parts per billion to sub parts per trillion1. Since few analytical methods have been developed to detect these compounds at said concentration levels [79] analytical challenges exist that call for the development of techniques capable of detecting trace levels of such environmental contaminants.

Surface enhanced Raman phenomena have garnered much attention since its discovery by Fleischmann et. al in 1974, when pyridine was analyzed on an electrochemically roughened silver surface [10]. Because of its ability to provide information-rich spectra of narrow spectral lines, it has been extensively used as an important analytical technique for both chemical and biological analysis. Studies utilizing this near field effect have focused on the monitoring of toxins in water [80], environmental pollutants [81], explosives detection for homeland security [82], pesticides detection [83], food analysis [84,85], pathogen detection [86–88], rapid DNA sequencing [89]. More importantly, the proven ability of Surface Enhanced Raman Spectroscopy (SERS) in single molecule detection [89–92], has prompted extensive study and development of robust techniques exploiting this effect. However, due to the lack of effective substrates that provide high sensitivity and highly reproducible SERS responses, SERS has not been routinely used for traditional trace analyses [48]. A considerable amount of work has been done in developing effective SERS substrates

from traditional random morphology silver islands on glass [93], colloidal silver solution [94], metal-polymer nanocomposites [48] to more regular structures such as those created via nanosphere lithography [95], and electron beam lithography-nanotransfer printing techniques [96].

Herein we have developed a simple and inexpensive method to create a highly sensitive and highly reproducible SERS substrate that can detect traces of toxic environmental contaminants including environmental estrogens. The SERS spectra of flavonoids in solution is very weak [97]. Our initial means of concentrating analyte on a noble metal surface evolved as we were first able to collect SERS spectra of daidzein from a solvent evaporated mixture of daidzein and silver colloid. Sensitivity was not adequate using this technique. Presented here is the realization of dual functionality of 3M's Empore diminutive extraction cartridges as an extractor/concentrator and a SERS platform. Preconcentration studies of selected environmental estrogens were done with high performance extraction disc cartridges (HPEDCs) to obtain the desired sensitivity and characterize the same as SERS substrate. A polypropylene microfiber prefilter that encloses the empore extraction medium is physically vapor deposited with silver creating nanoparticles. The noble metal nanoroughness allows the cartridge to serve as a SERS active substrate, onto which the analyte was passed through and harvested. Our novel approach of hyphenation of sample concentration on metal surface and SERS eventually resulted into the development of highly sensitive silver coated polypropylene filter (AgPPF) SERS substrate which is capable of detecting environmental pollutants like mitoxanthrone dihydrochloride as low as 1×10^{-10} M (51.74 pg/mL). Although a filter based SERS substrate has been successfully evaluated [98, 99], no one has yet realized the concentration protocol we employed here to increase the sensitivity of the technique. Moreover, we realized the dual functionality of SERS active HPEDCs, which eventually allowed the SERS detection of trace amount of selected environmental estrogen for the first time.

One of the most underlying analytical drawbacks of SERS is thermal and photolytic decomposition or fragmentation of sample analyte due to the continuous

irradiation of the laser beam over the SERS substrate. This alters the observed spectral bands and greatly affects the reproducibility of the technique [100, 101]. In our present work, we coupled our highly sensitive novel approach with a sample translation technique (STT) [100], translation of sample is achieved by spinning the sample off-centre, to improve the reproducibility. The combination of highly sensitive and highly reproducible techniques indeed, makes our approach a promising platform for environmental trace analysis of numerous analytes.

3.2 Experimental

3.2.1 Materials

3M Empore 4 mm dia./1 mL vol. high performance extraction disk cartridges and microscope glass slides were purchased from Fisher Scientific, and 99.99%, 2-3 mm diameter silver shots were from Alfa Aesar. Mitoxanthrone dihydrochloride (MDH), aminothiophenol (ATP), daidzein, genistein, flavone, and apigenin were purchased from Sigma Aldrich Chemicals. Rhodamine 6G (R6G) from Allied Chemical, crystal violet from Fisher Scientific, and p-Aminobenzoic acid (PABA) from Nutritional Biomedicals. Stock solutions were prepared with 18 MΩ Deionised water (Barnstead, E-Pure), HPLC grade methanol (Fisher Sci.), and dimethylsulfoxide (Fisher Sci.) according to their solubility.

3.2.2 Silver Deposition

3M Empore extraction cartridges were cut with a razor blade about 1 cm above the prefilter level. The cut piece of extraction cartridge (containing filter membrane) was adhered onto the microscope slide prior to silver deposition with the help of scotch double sided polyurethane foam tape. Each cartridge was then subjected to high vacuum (ca. 1×10^{-6} Torr) where 10 nm silver was then physically vapor deposited

onto the polypropylene filter at a rate of 1Å/sec using vapor depositor (Cooke Vacuum Product). Prepared AgPPF-SERS substrates were stored in a vacuum dessicator in the dark prior to use.

3.2.3 Scanning Electron and Atomic Force Microscopy

Scanning electron microscopy (SEM) image of a microfiber of AgPPF was taken using a LEO 1525 scanning electron microscope in a secondary electron detection mode. Low voltage (2kV field emission gun) was applied to reduce charging effect. Because of charge build up at high voltage, atomic force microscopy (AFM) is used to characterize silver nanoparticles on the AgPPF substrate.

All AFM images were taken in AC mode in air using Asylum Research atomic force microscope. Commercial silicon AC160 cantilever tips (Olympus) with a spring constant of 2.45 nN/nm were used. The tips were tetrahedral in shape and the tip radius of curvature was less than 10nm. The non contacting mode images reported here were taken at a scan speed of 0.67 lines per second.

3.2.4 Sample preparation and preconcentration

1×10^{-3} M stock solutions of crystal violet, MDH, and R6G were prepared in 18 MΩ deionised water. Stock solutions of PABA, ATP, daidzein, genistein, and flavone were made in HPLC grade methanol while stock solution of apigenin was prepared in dimethyl sulfoxide. All the stock solutions were diluted to the desired concentration with 18 MΩ deionised water.

For the preconcentration studies of daidzein and apigenin, each HPEDC was first conditioned with 150 μL methanol followed by 300 μL deionized water. 5mL of sample solution was then passed through the cartridge centrifuging at ∼3400 rpm, a mL at a time. Analyte was then extracted with 50 μL methanol in a 1.5 mL centrifuge tube. A 50 μL extract was evaporated to dryness in a speedVac evaporater, and then regenerated with ca. 5% methanol in deionized water prior to SERS analysis.

3.2.5 SERS Measurement and data acquisition

All SERS measurements were obtained using a LabRam spectrograph from JY-Horiba. The instrument is equipped with three different objectives, viz. Nikon 50X (0.45 NA, ∞), Olympus LWD CDPlan 20X PL (0.4 NA, ∞), and Olympus 10X BX-40 (0.25 NA, ∞). All objectives deliver up to 9 mW of the 632.8 nm line from an electrically cooled He-Ne laser source. The confocal hole and slit hole of the instrument were set to 500 μm and 200 μm, respectively. All spectra were collected in 180° geometry with a 3000 cm^{-1} spectral window. The scatter was dispersed with a 600 grooves/mm grating, imaged with a 1024$\times$ 256 thermoelectrically cooled charge coupled device (CCD) camera, and processed with Labspec 4.12 software. Focusing of the microscopic objective and positioning of the laser spot under stationary and translation conditions were done with a computer controlled x-y-z stage. The stanford SR-540 chopper was used for fast translation via spinning of the samples during experiment. The chopper allows the translation of the sample at spin rates up to 8000 rpm.

150 μL aliquots of each sample solution was exposed to the AgPPF substrate for approximately three minutes. Sample solution was then slowly passed through the substrate (ca. 500 μL/min) with the gas tight syringe prior to SERS analysis. Sample concentrated AgPPF is then precisely centered at the top of translator and brought into focus for maximum SERS intensity. Spectra were collected by spinning translator at 2000 rpm and 10 micron off-center. Baseline corrections were done in order to correct the optical background signal from the substrate. Since there was not any significant evidence of SERS background of AgPPF, substrate background corrections were not needed.

3.3 Results and Discussion

In the present work, we realized a simple and inexpensive approach to perform a highly sensitive and reproducible SERS analyses. Our approach of passing analyte through the extraction cartridge via AgPPF substrate allows proximal access of analyte onto the roughened silver surface which in turn enhances SERS intensity. In order to characterize AgPPF as a promising SERS substrate a silver thickness study and volume optimization study were carried out to identify optimal conditions relating to SERS performance. The roughened silver surface on the polypropylene filter was characterized by atomic force microscopy, and general performance and sensitivity of the technique is presented with respect to various environmental constituents. SERS signatures of several flavonoids, so called environmental estrogens, and their limit of detection (LOD) are reported at nanomolar concentrations for the first time.

3.3.1 Substrate Morphology

The polypropylene filter in the HPEDC is made up of polypropylene microfibers of various sizes. An SEM image of silver deposited polypropylene filter is shown in Figure 3.1A. Due to the excess charge build up at high voltage, AFM images were taken to characterize the bare and silver modified polypropylene surface. Figure 3.1B is the AFM image of bare polypropylene fiber. After coating with 10 nm silver, the surface developed nanoroughness due to the formation of various sized silver nanoglobules. Figure 3.1C shows that silver nanoglobules formed on microfibers are less than 100 nm in size and are closely packed. Since these closely packed nanoparticles resemble colloid aggregates, such as just touching nanoparticles [37] and immobilized silver colloids [102], it is reasonable to expect good SERS activity. However, the increased sensitivity is largely due to our protocol of concentrating probe molecules on and between silver globules when sample solution is passed through the substrate.

In our study, sample solution was dispensed through AgPPF prior to spectral acquisition. Therefore we were suspicious whether the surface morphology becomes

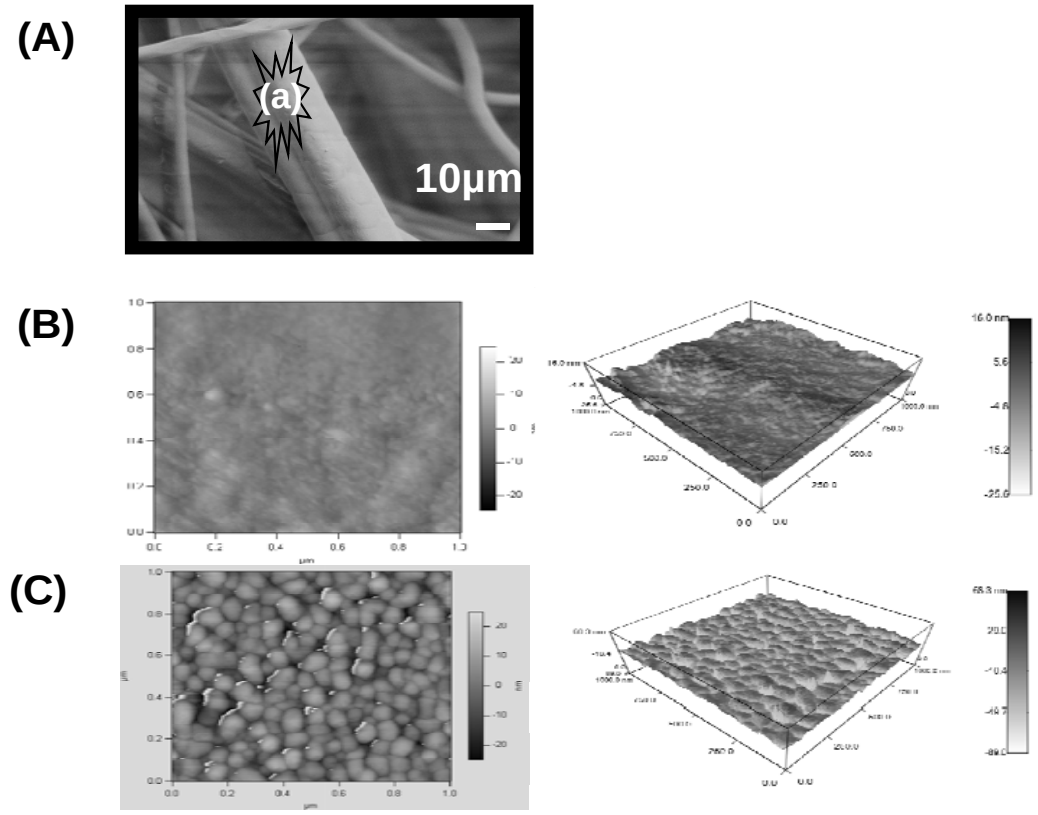


Figure 3.1: SEM image of polypropylene prefilter (A) and AFM images of part "a" of Figure 1A, without silver (B) and with 10 nm physically vapor deposited silver (C).

altered after analyte is passed through the substrate. AFM images of AgPPF were obtained for both aqueous solution and methanol (used as eluant in preconcentration study). There was not a noticeable difference observed for aqueous solution, however, very slight differences were observed for the methanol rinse but not distinct enough to allow or call for significant interpretation.

3.3.2 Optimization Studies

Thermal deposition of silver at various average thicknesses was performed and the respective SERS response was recorded with respect to R6G. The thickness of the silver particles was monitored by a parallel quartz crystal microbalance in a cryogenically pumped deposition chamber at about 1×10^{-6} Torr. Figure 3.2 shows the SERS response of R6G as a function of metal thickness. It is observed that 10 nm silver thickness gives the best SERS activity. All mass thickness studies were carried out at the same constant deposition rate of 1Å/Sec. The best SERS performance at 10 nm silver thickness might be because of both greater Raman cross-section for adsorbed molecules and improved plasmon resonance at our excitation wavelength of 632 nm. Although recent studies support that there is often no direct correlation between the maximum of the extinction spectrum with the laser excitation for SERS activity [37, 54], we attempted to report extinction spectra for each mass thickness. Since our substrate is opaque, attempts were made in a diffusion reflectance mode. Unfortunately, we were unable to obtain acceptable extinction spectra. This might be because of highly variable reflectivity of our AgPPF substate in which silver nanoglobules are dispersed on different sized (width) polypropylene microfibers.

In addition, we noticed that the volume dispensed through the AgPPF substrate has an interesting effect on the SERS activity. In order to optimize the sample volume permeated through the substrate two different approaches were studied. Since SERS is a surface phenomenon dependent on amount of analyte in close proximity to the noble metal surface, we first attempted to collect the SERS response of a sample

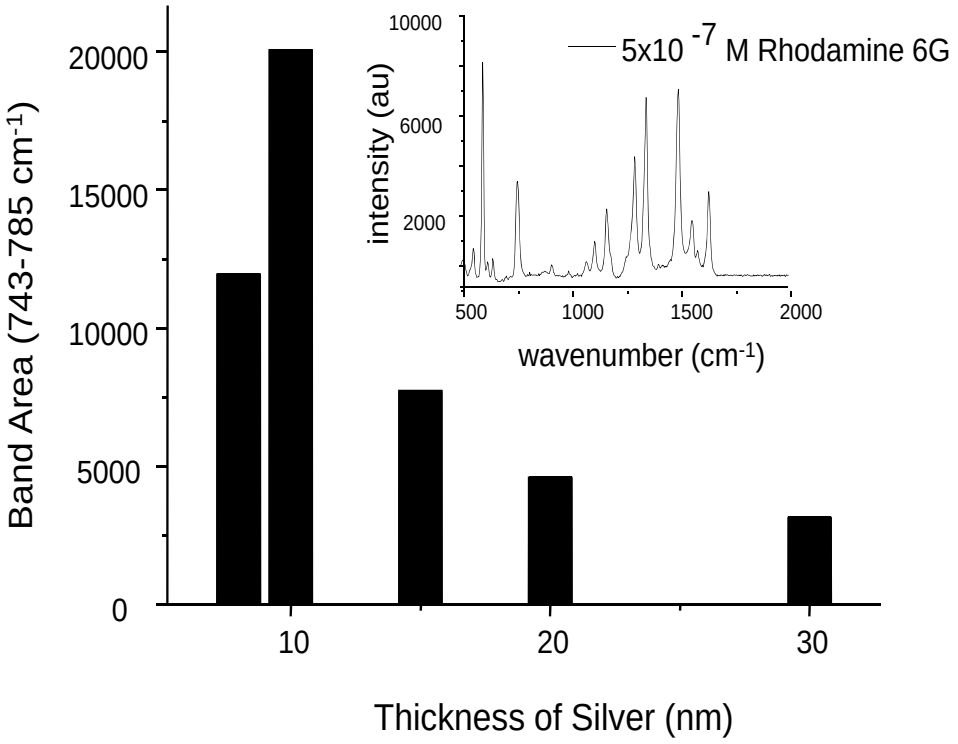


Figure 3.2: Silver thickness optimization; Band areas centered at 763 cm^{-1} of 5×10^{-7} M R6G on AgPPF substrate at various thickness of silver. The inset is the spectrum of 5×10^{-7} M R6G (conditions: STT; 20x objective; 1s acquisition time; laser excitation of 4.0 mW at 632.8nm; and Ag deposition rate of 1.0 Å/sec).

solution for different mass by volume (w/v) ratios of analyte to solvent. Keeping the mass constant, the volume of solvent was increased (sample was diluted to certain volume), and the whole volume was passed through the substrate prior to SERS acquisition. Figure 3.3A shows that upon diluting 50 μL of 1×10^{-6} M R6G to 100 μL, 150 μL, 250 μL, and 350 μL followed by dispensing all through the substrate, the SERS intensity decreases (Fig 3.3A, solid bar). In other words, just by keeping the mass constant for different load volumes, the SERS intensity does not remain constant; instead the response decreases as the dilution factor increases. Parallel experiments were performed by dispensing 50 μL aliquots of each diluted sample (Fig 3A, patterned bar), and compared to the results with the former (different w/v ratios sample loads). As expected it was observed that 50 μL aliquots give a weaker intensity than the large volume counter parts and in proportion to concentration. This provides evidence that both molecular kinetics and thermodynamics of equilibrium between solid-liquid phases influences in the adsorption of R6G on the AgPPF surface, and eventually in achieving optimal SERS performance. Since R6G has been chosen as the model analyte, other system might behave differently depending on the intrinsic thermodynamic affinity of the solute for the substrate surface.

Since our first volume study was not conclusive in volume optimization, a second study was carried out simply by altering the total volume of a solution at a particular concentration (mol/L). Fig 3.3B shows that upon increasing the total volume of 1×10^{-6} M R6G from 50 μL to 500 μL, the SERS signal intensifies up to 150 μL and then degrades. A similar study was performed for other concentrations with the same outcome (data not shown). This volume effect is not clearly understood. However, it is to be noted that over the volume range of 50 - 500 μL, the variation in spectral intensity is approximately two fold. This suggests that as the volume is increased from the optimized amount, there might be minute individual or collective effects of several factors on SERS activity, such as slight change is surface morphology, wash-off of analyte, and/or formation of a multilayer depending on the concentration and volume of sample solution dispensed through it.

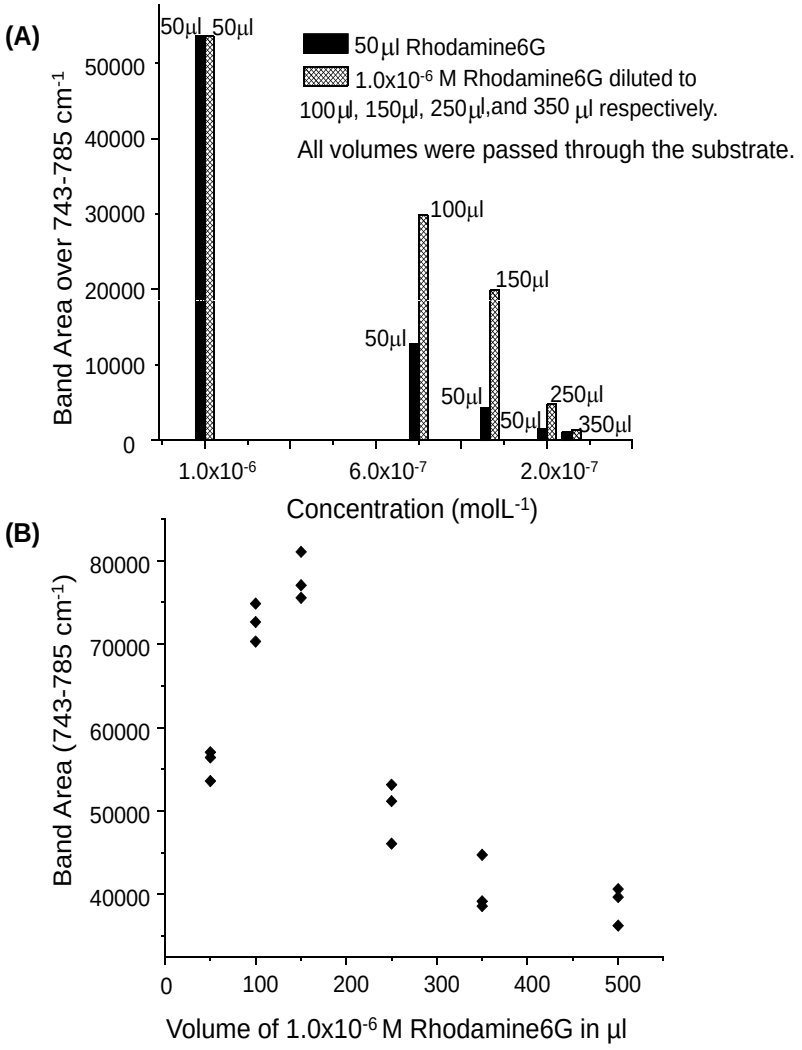


Figure 3.3: Effect of Volume passed through AgPPF substrate on SERS signal; (A) Band area centered at 763 cm^{-1} against different load volumes but constant mass R6G solution (patterned bar). Solid bar is of 50 μL aliquot of each diluted solution. (B) SERS responses (triplicate) of 1×10^{-6} M R6G against the volume of analyte dispensed through AgPPF substrate. 150 μL is the optimized volume in our study. (Conditions: same as Figure 3.2)

3.3.3 Performance Studies

SERS performance of our new substrate in combination with our novel approach of concentrating analyte on AgPPF substrate was studied with resonant enhanced, near-resonant, and nonresonant compounds at our excitation wavelength of 632 nm. The organic dye R6G and the personal care product pABA were selected as nonresonant compounds, crystalviolet as near-resonant, and pharmaceutical MDH was chosen as resonant enhanced compounds at our excitation wavelength. Figure 3.4 reveals SERS signatures of the previously mentioned compounds and their detectable spectra at a low concentration, without a preconcentration step. All significant bands from R6G and pABA were detected as low as 5×10^{-8} M each, along with the similar sensitive detection of 1×10^{-9} M and 1×10^{-10} M for crystalviolet and MDH, respectively.

Substrate-to-substrate reproducibility is of major concern for SERS, and was determined with reference to the peak area of 5×10^{-5} M ATP centered at 1056 cm^{-1}. To avoid thermal and photolytic decomposition or fragmentation of sample analyte, we used an STT method [100], previously developed in our research group, during data acquisition. Data was collected 10 microns off-center as explained earlier in the experimental section. For five different substrates (n=5), the overall relative standard deviation (RSD) was observed to be 7.3%. Moreover, validity of our concentration protocol over dipping method was tested. Two test compounds, ATP, which is expected to saturate the silver surface with a covalently bound self-assembled monolayer, and pABA, that does not necessarily form a monolayer, were selected. As shown in Fig 3.5B, there is almost no difference in SERS activity for ATP while SERS enhancement for pABA is almost 10-fold more intense using the concentration protocol rather than the dipping approach. This observation suggests that, irrelevant to the inherent surface enhancements of the SERS substrate, our approach of concentrating analyte on noble metal surface increase SERS intensity to some extent depending on the nature of analyte.

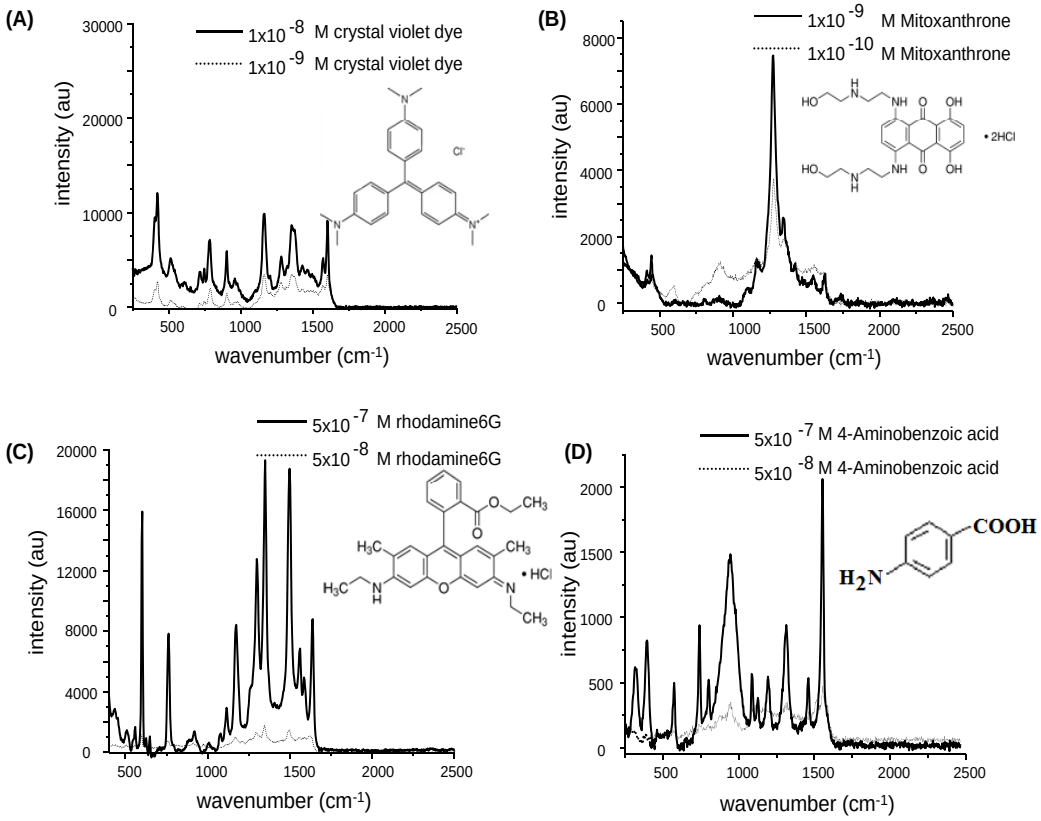


Figure 3.4: SERS signatures and detectable spectra of various analyte at low concentration; (A) crystalviolet (B) MDH (C) R6G, and (D) PABA, at optimized conditions (Spectra were collected under STT conditions with 80x objective at 5 sec acquisition time using 4.0 mW, 632.8nm laser excitation)

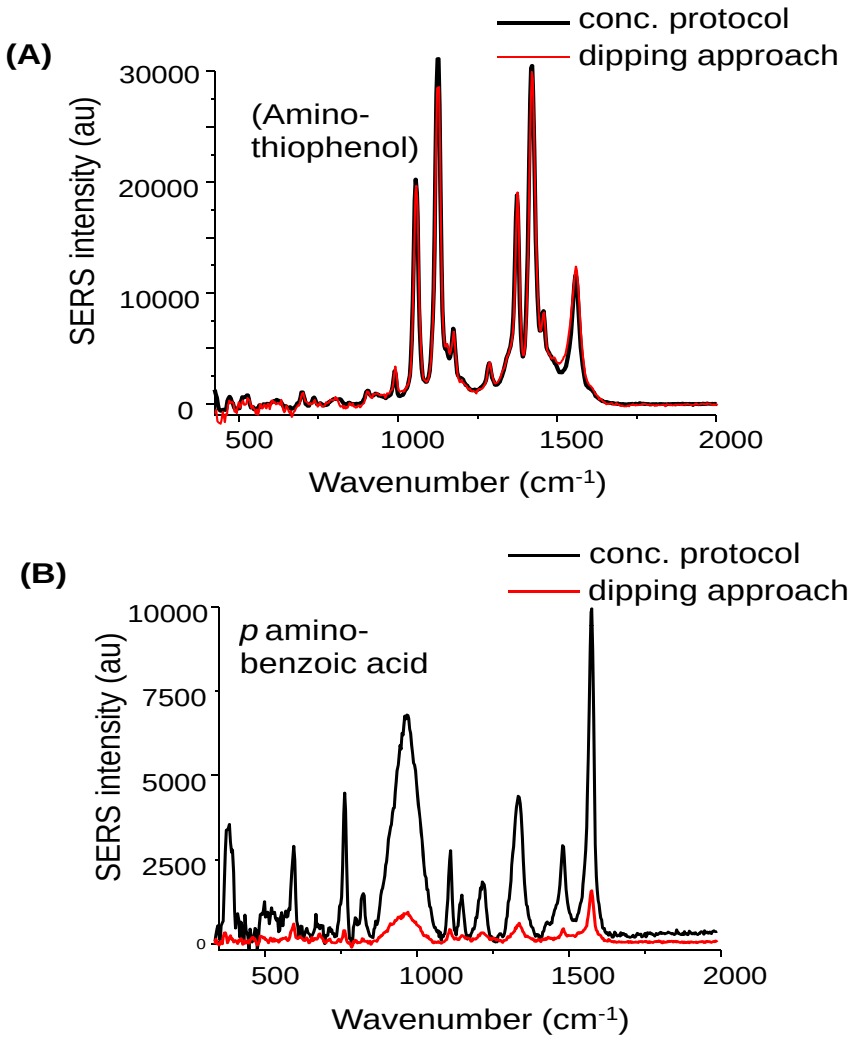


Figure 3.5: Comparison of concentration protocol and dipping method for SERS enhancement of 1×10^{-5} M Aminothiophenol (A), and 1×10^{-5} M p-Aminobenzoic acid (B).(Spectra were collected under STT condition with 10x objective at 1 sec acquisition time using 10.0 mW, 632.8nm laser excitation)

Moreover, the HPEDCs were used both for SERS and preconcentration study (discussed later in flavonoid studies). Therefore, experiments were carried out to test if the same extraction cartridge could be developed as a SERS substrate after a preconcentration step has taken place. Silver was physically vapor deposited on the polypropylene filter of an extraction cartridge after the preconcentration step was performed. The SERS spectrum of 1×10^{-5} M daidzein was then acquired and compared with daidzein deposited on a SERS substrate created with an unused extraction cartridge. It was observed that there is no appreciable compromise in SERS activity of a substrate created in a used HPEDC when compared to the one created in a new cartridge (Band area centered at 837 cm^{-1} for the two cases were within 10%). Hence, the current approach offers a cost effective dual use for HPEDCs.

3.3.4 SERS of Selected Flavonoids

Despite the enormous interest in environmental estrogens, only a few SERS studies of flavonoid have been reported [97, 103, 104]. This can be attributed to the poor aqueous solubility and low SERS sensitivity of the chemicals. However, our approach of concentrating a sample analyte onto a novel SERS substrate prior to SERS interrogation allows for significant sensitivity enhancement of the flavonoid SERS signal. Figure 3.6 shows the SERS signature of daidzein, genistein, apigenin, and flavone. Each individual SERS spectrum can be used as the "fingerprint" of the corresponding compound for the further study. Moreover, as of our knowledge, no one has previously reported the SERS signature of daidzein and genistein.

In this work, we have selected daidzein and apigenin for quantitation. In order to identify distinct bands from each of these chemicals, SERS spectra of their mixtures were obtained and compared with their individual spectra. Figure 3.7A shows that the peaks at 1217 cm^{-1}, and 837 cm^{-1} are solely from apigenin and daidzein, respectively. The distinct bands from the individual spectra were used to plot a calibration curve for each compound. Beside the working curve of standard solutions, preconcentration

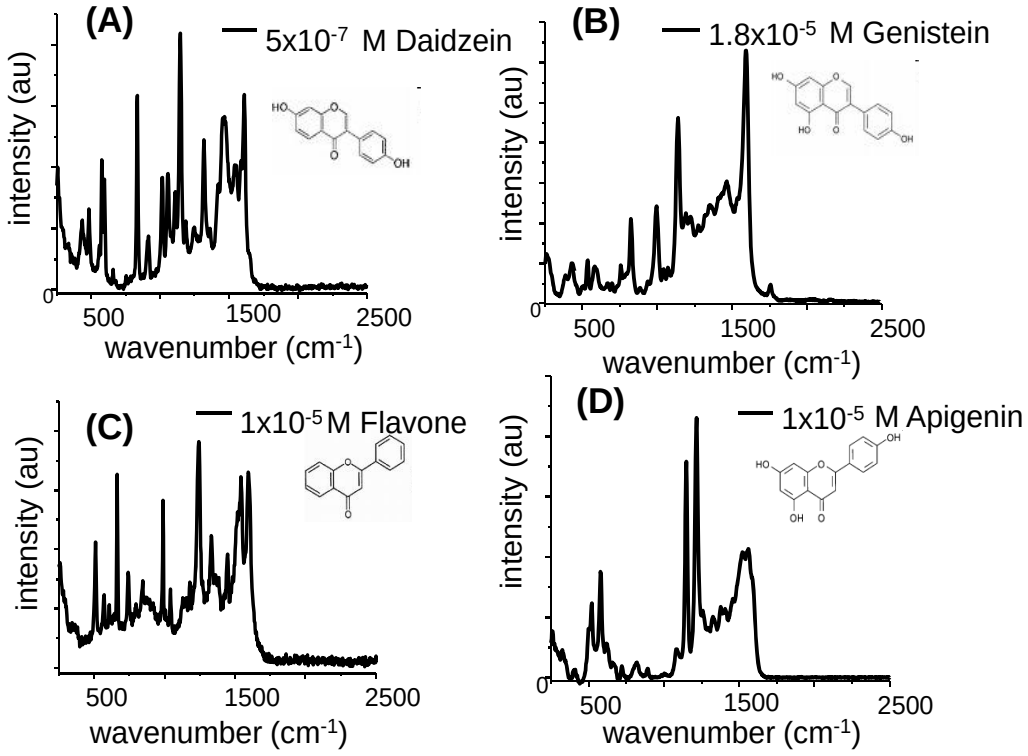


Figure 3.6: SERS signatures of selected Flavonoids; (A) daidzein (B) genistein (C) flavone, and (D) apigenin. (Spectra were collected under STT conditions with 50x objective at 1 sec acquisition time using 4.0 mW, 632.8 nm laser excitation)

studies of both apigenin and daidzein were performed. In this study, we were able to detect apigenin and daidzein down to 5×10^{-8} M and 1×10^{-7} M, respectively, without any preconcentration step. With the generic preconcentration step using HPEDCs, we estimated for the first time the sensitive SERS detection of daidzein and apigenin as low as 1×10^{-9} M (0.254 ng/mL) and 4×10^{-9} M (1.08 ng/mL), respectively with a signal-to-noise ratio of greater than 3.

Working curves of both daidzein and apigenin, with and without preconcentration, are shown in Figures 3.7B and 3.7C. Each plot in the figure has two x- and y-scales. Bottom X and left Y axes are for standard solutions while top X and right Y axes are for preconcentrated solution. The calibration curve is presented in double X/Y axes plot in order to show direct comparison between the spectral counts of preconcentrated solution and standard solution. The ratio of SERS response of preconcentrated solution and 100-times more concentrated standard solution is considered to evaluate the extraction/regeneration efficiency of the technique. It is observed in the calibration plots that the ratio decreases with dilution. As a result, about 5% of the total SERS response of 1×10^{-7} daidzein was observed for 1×10^{-9} in contrast to about 37% of 1×10^{-5} M for 1×10^{-7} M. Similarly, for apigenin about 32% SERS response was observed for higher concentration while the signal from 1×10^{-9} M was not seen. This shows that there is a possible loss of analyte during extraction/regeneration step that affects the SERS intensity. Despite the sample loss during preconcentration study, one can further increase the sensitivity by using large HPEDCs having more sorbent mass [105]. In addition to this, it is to be noted that during preconcentration, 50μL methanol extract was not directly used for SERS interrogation; instead the aliquot was evaporated/dried and regenerated with about 5% methanol, as stated in experimental section. No SERS response was observed in methanol solution. This could possibly be attributed to the influence of the methanol on the equilibrium of flavonoid with the silver surface. It is believed that hydroxyl group present in flavonoid facilitates strong chemical binding to the silver surface [97]. In addition to the relative chemical affinity of flavonoid, methanol solution resides a

relatively shorter time than the aqueous solution on AgPPF substrate because of the different wettability of solvents. This perturbs both diffusion and equilibrium between solid/liquid interfaces and hence affects the SERS response accordingly.

3.4 Conclusions

In conclusion, we developed a highly sensitive and reproducible silver modified polypropylene prefilter SERS substrate that is capable of detecting selected environmental contaminants like mitoxanthrone dihydrochloride in the mid pM range without any preconcentration step. Our simple and unique approach of concentrating analyte on silver surface prior to SERS data acquisition allows sensitive detection of rarely SERS-studied environmental estrogens. Our realization of dual functionality of HPEDCs for extraction and SERS substrate allows the cost effective and highly sensitive SERS detection of trace amount of Daidzein and Apigenin for the first time and the SERS spectra of daidzein and genistein can be used as SERS signature of respective flavonoids for further study.

3.5 Acknowledgements

This work was supported by the US Environmental Protection Agency STAR Program under grant EPA-83274001 with the University of Tennessee. The authors would like to acknowledge Dr. John Dunlap of UT-Knoxville, Division of Biology-Microscopy Facility for assistance with atomic force microscopy.

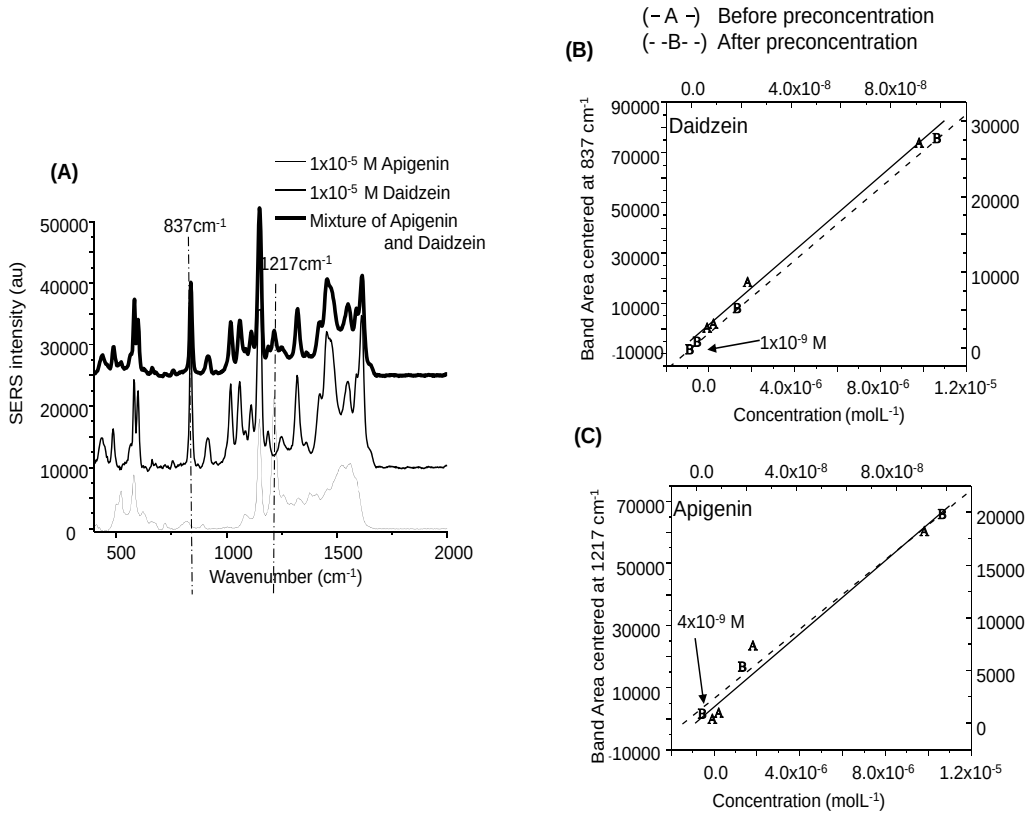


Figure 3.7: (A) SERS spectra of both apigenin and daidzein compared with the SERS spectrum of their mixture. Bands at 837 cm^{-1} and 1217 cm^{-1} are solely due to daidzein and apigenin, respectively. (B, C) Working curves for daidzein and apigenin, respectively. Bottom X- and left Y-axes (designated -A-) are for standard solutions without preconcentration, similarly top X- and right Y- axes (designated –B–) are of preconcentrated solutions. (Conditions; same as Figure 3.6)

Chapter 4

Characterization and Detection of Uranyl Ion Sorption on Silver Surfaces Using Surface-Enhanced Raman Scattering Detection

Chapter 4 is an adaptation of a research article *Analytical Chemistry,* ***2009****, 81, 8061-8067*. The article describes the use of AgPPF and nanolithographically created SERS substrates in the study of uranyl ion sorption on nanostructured silver surfaces.

4.1 Introduction

The key component in spent nuclear fuel is Uranium. Due to the direct disposal of spent fuel in a nuclear waste repository and the possible migration of the contaminants to the groundwater [106], the assessment of water contamination is of primary environmental concern. With respect to this, the behavior of Uranium(VI) is most important. The aqueous chemistry of UO_2^{2+} has been fairly well-investigated using potentiometric measurement [107], time-resolved fluorescence spectroscopy [108], and

Raman spectroscopy [109, 110]. In an aqueous solution, uranyl species exists in a number of polymeric uranium(VI) forms, usually monomers, dimers, and trimers. The hydrolysis equilibrium establishes according to the following equation;

$$mUO_2^{2+} + nH_2O \rightarrow (UO_2)_m(OH)_n^{2m-n} + nH^+ \tag{4.1}$$

Equation (1) shows that pH is a main factor in the hydrolysis of uranyl and the reaction equilibrium shifts towards the product as the pH increases. Results from previous studies [107, 108, 110, 111] reveal that three species [UO_2^{2+}, $(UO_2)_2(OH)_2^{2+}$, and $(UO_2)_3(OH)_2^{5+}$] are the most prevalent species in acidic medium (pH 0 to 4). However, the chemistry of uranyl(VI) solution near neutral pH and alkaline condition is rather uncertain. This is attributed both to the coexistence of number of hydroxo species [107, 108] and formation of a uranate salt [112, 113].

Although aqueous chemistry of the Uranium(VI) has been studied for several decades, it is equally important to understand the interaction of these complexes with the solid surfaces [114, 115], which can be pursued using surface techniques like surface enhanced Raman spectroscopy (SERS). Several studies focused on the sorption mechanism of uranyl species on different solid surfaces have been published using different spectroscopic techniques [115–121]. However, as of now, only a few Raman spectroscopic studies highlighting the direct adsorption mechanism of uranyl on a silver surface have been found [114, 115, 122]. Despite the limited understanding of uranyl sorption on a silver surface, several attempts have been made in quantifying UO_2^{2+} using SERS [114, 122–127]. Although Clavijo et al. [125] had performed a SERS study of the interaction mechanism of uranyl superphtahlocyanine on silver surface, Dai et al. [122] were the first to report the SERS enhancement of UO_2^{2+} on a sol-gel silver surface. Depending on the nature of experimental methodology, different researchers have assigned the distinct symmetric stretching ν mode of uranyl species at different wavenumbers. For example, Tsushima et al. [115] used 0.1 M uranyl nitrate solution to study uranyl adsorption on the silver sol and observed a continuous

band shift of the symmetric stretching frequency of UO_2^{2+} from 798 cm^{-1} to 751 cm^{-1} on increasing pH. Teiten and Burneau modified the silver colloid surface with N-(2-mercaptopropionyl)glycine [127] and 2-(5-bromo-2-pyridylazo)-5-diethylaminophenol [124] and reported that the symmetric stretching band of UO_2^{2+} appeared at 840 cm^{-1} and 828 cm^{-1}, respectively. Using a silver-doped sol-gel SERS substrate, Bao et al. [123] observed the uranyl peak around 710 cm^{-1}. More recently, Ruan et al. [126] detected uranyl peak at around 830 cm^{-1} on the (aminomethyl)phosphonic acid modified gold particles, while Leverette et al. [114] observed broad peak of uranyl cast film on aligned silver nanorod SERS substrate at around 700 cm^{-1}.

A very wide distribution of symmetric stretching frequencies of uranyl species on a noble metal surface and the broadness of the band gives a general notion that different sorption mechanisms exist. Two different novel SERS substrates, not used before for the uranyl characterization, are utilized with high sensitivity in the present work. In the first case, a thermally vapor deposited silver surface on a polypropylene filter (PPF) is used for the sorption study of UO_2^{2+} and its detection. A broad Raman peak that appeared around 700 cm^{-1} is considered to be the symmetric stretching mode of the oxygen-bridged uranyl species, similar to uranates. It is anticipated that an oxy-bridge between silver particles and the uranyl functional group exists in our system. The effect of temperature, prolonged solute-surface interaction time, and pH are studied in terms of spectral changes. Exploiting the results of our studies elucidating the basic chemistry behind the sorption behavior of the uranyl ion on a silver surface, this radionuclide species is detected as low as 20 ng/mL. In a second approach, well-defined nanofabricated SERS substrates are designed and created via electron beam lithography (EBL) and a lift-off approach in which dimer nanoparticles with variable nanogaps are periodically arrayed. The possibility of using this lithographic SERS substrate in the sensitive detection of uranyl is explored.

4.2 Materials and Methods

4.2.1 Materials

Polypropylene prefilters (0.2 μm x 47 mm), prime grade silicon wafer (orientation100), and 13 mm syringe filter holder were purchased from Sterlitech Corporation, Wafer World Inc., and Fisher Scientific, respectively. Silver shot (99.99%, 2-3 mm diameter) were purchased from Alfa Aesar. Uranyl nitrate hexahydrate, Baker reagent 4196, was purchased from Baker Chemical Company and Benzenethiol from Acros Chemicals. All solutions were prepared with 18 MΩ deionised water (Barnstead, E-Pure).

4.2.2 Vapor deposition of silver particles

PPF were cut to a 12 mm diameter size pieces by using cork borer. The cut pieces of filter membrane were adhered onto the microscope glass slide with the help of scotch tape. A glass slide holding few 12 mm diameter PPF pieces was then placed into a high vacuum chamber (ca. 1×10^{-6} Torr). 10 nm silver was then thermally vapor deposited onto the PPF at the rate of 1Å/sec using vapor depositor (Cooke Vacuum Product). Silver deposited substrates were then used for SERS interrogation and stored in a vacuum desiccator in the dark in between the sample run. All substrates were used within 24 hours. Similarly, 25 nm silver was deposited onto the nanofabricated substrates.

4.2.3 Preparation of nanofabricated substrates (electron beam lithography, EBL, and reactive ion etching, RIE)

50×50 micron periodic arrays were created in AutoCAD 2005. Each array contains sets of ellipse-sphere dimers. Each sphere was designed to be 54 nm in diameter with the ellipses of 81:36 nm (long axis : short axis) size with and interparticle spacing ranging from 40 nm to 70 nm and dimer-dimer spacing of 450 nm. By using

the LinkCAD conversion program, each AutoCAD drawing was converted to GDS-II format and then transferred to the EBL system computer.

A 2 inch silicon wafer (Wafer World, FL) was prebaked at 250°C for 45 minutes to drive off any moisture that had adsorbed onto the surface. A 300 nm thick positive resist, ZEP 520 A (Zeon Chemicals, KY), was spin coated onto the silicon wafer at 6000 rpm for 45 seconds, baked at 180°C for 2 minutes and then placed under vacuum in the EBL system. The thickness of the resist was estimated from a chart provided by the manufacturer based on the spin rate. A Jeol JBX-9300 EBL system with a 100 keV thermal field emission gun at a beam dose of 420 $\mu C/cm^2$ was used for the direct writing of the nanopatterns. Each 50×50 micron array was equally spaced 200 μm in x-direction and 200 μm in y-direction to create a 4×5 set (rows$\times$columns). Each row has similar features while each column has varied interparticle spacing within a dimer. The exposed patterns were then developed in xylenes for 30 seconds and rinsed with isopropanol. A descum process was then run on the developed patterns with an oxygen plasma (Technics Reactive Ion Etcher) at 100 Watts for 6 seconds. For the lift-off procedure, 10 nm of chromium was vapor deposited onto the plasma treated patterns using dual gun electron beam evaporation chamber (Thermonics Laboratory, VE-240). The wafer was then rinsed with acetone, isopropanol, and water, successively to remove leftover resist and extra chromium. The patterns were then etched to 250 nm pillar height using an Oxford RIE at the rate of 100 nm/min. After etching, chromium on the substrate is removed using a chromium photomask etchant, Cr-14S. This was followed by the deposition of 20 nm silicon dioxide using an Oxford Plasma Enhanced Chemical Vapor Depositon at the rate of 1.2 nm/sec. The substrate thus created is ready for the silver deposition. Note that the dimmer gap is reduced following the deposition of SiO_2 and Ag.

4.2.4 Scanning electron microscopy

All scanning electron microscopy (SEM) images were collected using LEO 1525 microscope in a secondary electron detection mode. The field emission gun at an operating voltage of 3 kV was applied to reduce the charge build-up and sample damage.

4.2.5 SERS measurement and data acquisition

SERS measurements were acquired using a LabRam Spectrograph from JY-Horiba. Details about the optics have been previously described [128]. For the SERS interrogation using silver modified PPF substrate, 12 mm size SERS substrate is placed into the filter holder and 150 μL aliquot of sample solution was exposed to the silver surface for the specified time and then slowly passed through the substrate (ca. 500 μL/min) with the help of gas tight syringe prior to SERS analysis. The substrate is then precisely centered at the top of translator. Spectra were collected by using sample translation technique [100]. Similarly, the nanofabricated SERS substrate was dip-coated with 20 μL of analyte prior to SERS interrogation using x-y-z translator. In each case, baseline corrections were done in order to correct the optical background signal from the substrate. Since there was not any significant evidence of SERS signal from the substrate, background corrections were not needed. Temperature studies were performed using Frigidaire Refrigerator and Precision mechanical convention oven prior to data acquisition. The pH adjustments of the solution were done with nitric acid and sodium hydroxide. All spectra were recorded using 80X microscope objective, 2 mW laser power, and 2 sec acquisition time unless otherwise mentioned.

4.3 Results and Discussions

4.3.1 Studies involving experimental conditions

Due to an overwhelming environmental and non-proliferation concerns, detection of uranyl ion in an aqueous solution is of primary importance. In order to quantify uranyl using SERS, it is equally important to understand the basic chemistry behind sorption behavior of the ion on the metal surface. Two different novel SERS substrates, silver modified PPF and well-defined nanofabricated ellipse-sphere dimer patterns, were utilized for the present study. The PPF substrate was chosen mainly for two reasons; firstly, it is a simple and promising SERS substrate onto which silver easily develops nanoroughness [128], and secondly, it is commercially available and is cost effective as each substrate (12 mm diameter) costs less than $0.10. PPF substrate has been used mainly in this manuscript. Similarly, our purpose of introducing nanofabricated dimer patterns is to demonstrate an alternative SERS approach that has the possibility of ultra trace detection of uranyl through rational optimization of substrate morphology. The AFM images of silver deposited PPF can be found elsewhere [128]. Throughout the manuscript we discuss both basic insights into uranyl-surface interaction and the sensitive detection of uranyl via SERS.

Representative Raman and SERS spectra of uranyl nitrate hexahydrate are shown in Figure 4.1. The nitrate peak [129], in both cases, is not altered and appeared at 1031 cm^{-1} while the symmetric stretching band of the uranyl in a Raman and SERS spectra appeared at 854 cm^{-1} and 707 cm^{-1}, respectively. Moreover, the SERS band of uranyl is relatively broad and asymmetric which could indicate the contribution of several hydrolyzed uranyl species to the band. This sort of broad SERS peak of uranyl has also been previously reported by Dai et al. and Laverette et al. directly on the unmodified silver surfaces using different SERS substrates [114, 122]. There also appears an unassigned peak at about 870 cm^{-1}. In order to confirm that the 870 cm^{-1} peak is not from the physisorbed uranyl species, the uranyl loaded PPF substrate

was rinsed with water for several times prior to data acquisition. No alteration was observed in the peak. Moreover, a broad spectral feature appeared at around 1500 cm^{-1} in a SERS spectrum is attributed to the carbon residue on the PPF substrate.

Since SERS has an extreme dependence on surface-analyte distance, the total number of probe molecules in the proximity of the metal nanoparticles is very important and may depend on the sorption kinetic phenomena. The effect of solute-surface interaction time between uranyl and silver surface is reported herein. Figure 4.2 shows that on increasing the exposure time, Raman intensity increases. However, it is to be noted that at a certain point, the intensity dropped abruptly. The sudden fall in spectral counts might be due to the oxidation of the substrate, which is very common with silver nanoparticles. The appearance of distinct symmetric bending frequency of Ag-O at 215 cm^{-1} supports silver oxidation [130]. A plot of signal intensity against interaction time with the error bars is shown in the inset of Figure 4.2 showing that the signal intensity increases continuously up to 75 minutes and then drops-off suddenly without any indication of reaching equilibrium. Although the sorption equilibrium is not illustrated, our study provides the general scheme of sorption kinetics of uranyl ion on the silver surface which can be an important factor in the trace analysis of this radioactive species.

Because this temporal study reveals that the rate of adsorption of uranyl on the silver surface is a rather slow process, we performed a temperature study to further investigate the sorption chemistry. Although there are several factors that affect sorption from solution onto the solid surface, temperature is expected to have a substantial impact. Normally one would expect that sorption processes would entropically diminish as temperature increases. However, in our present study, for the temperature range from 4°C to 90°C, the Raman intensity continuously increases with increasing temperature (see Figure 4.3). In other words, the energy provided to the system favors the sorption process. In addition to the complex solvation properties of the free uranyl at elevated temperatures as reported by Zanonato et al. [131], our

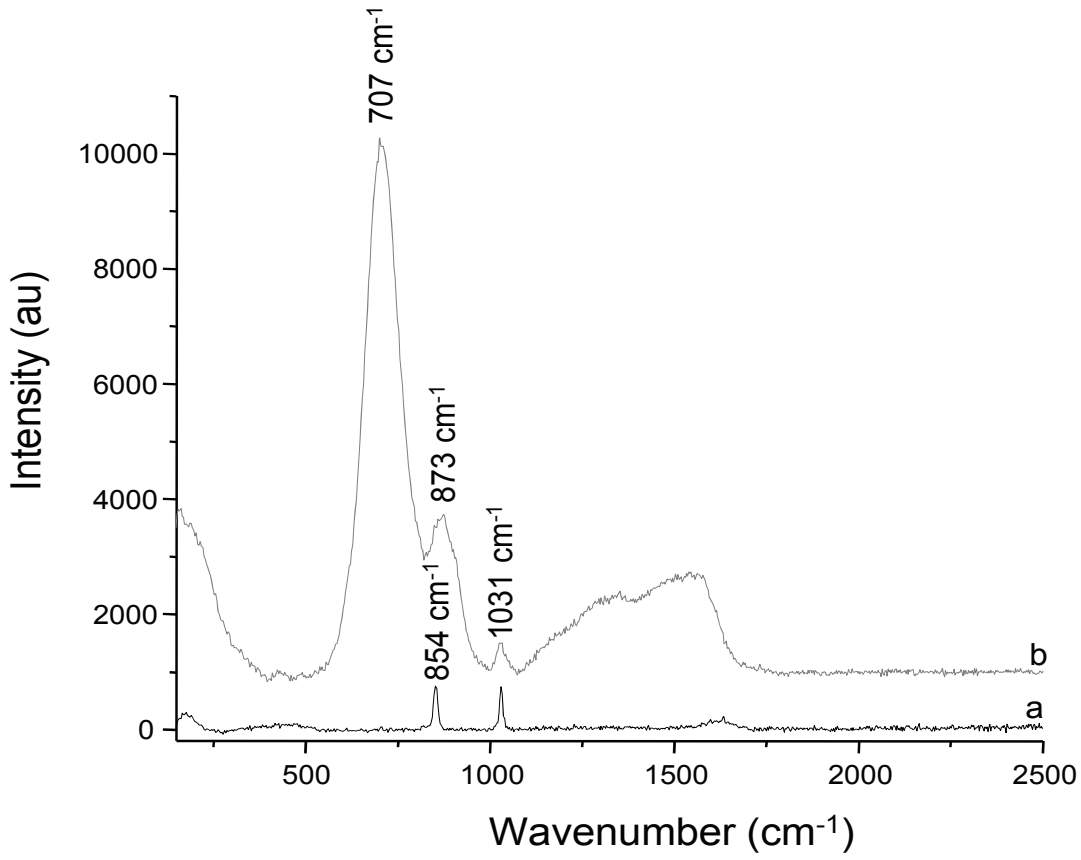


Figure 4.1: Representative (a) Raman ($[UO_2^{2+}]$ =0.1M, pH=3.6), and (b) SERS spectra ($[UO_2^{2+}] = 5 \times 10^{-7}$ M, 75 minutes delay time at room temperature, pH=7.1, PPF substrate) of uranyl nitrate hexahydrate solution.

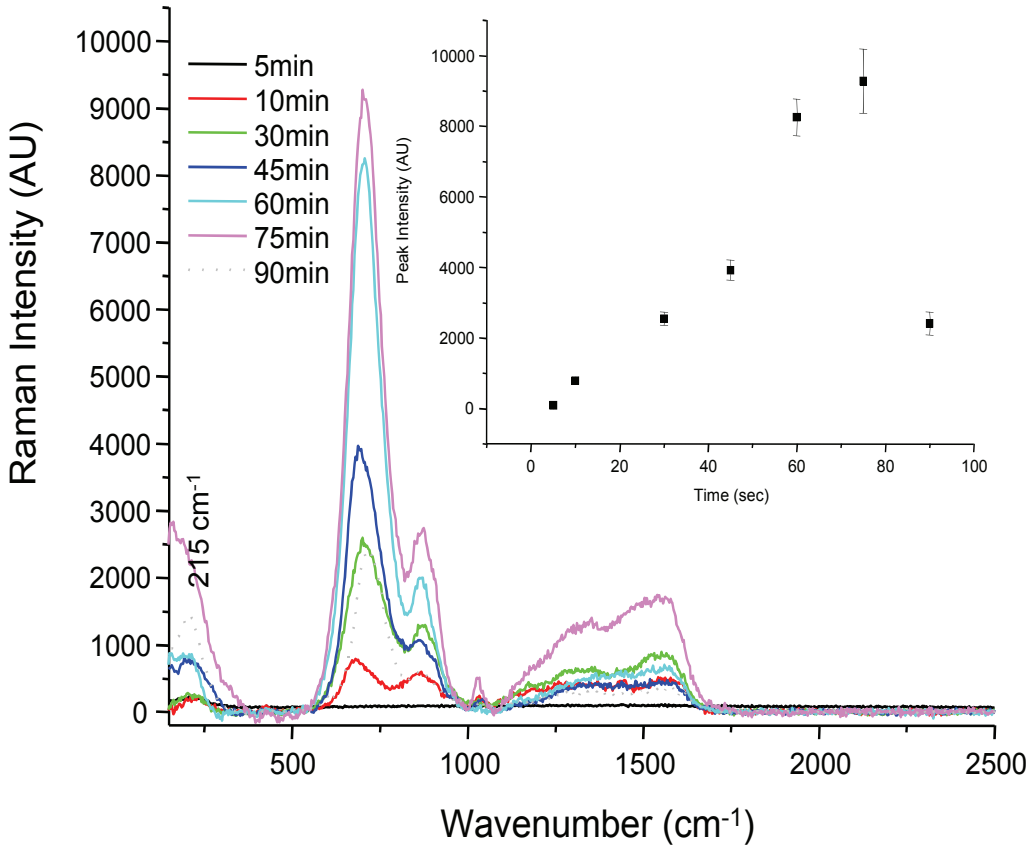


Figure 4.2: Figure showing the effect of solute-surface interaction time on SERS intensity of uranyl loaded silver. Inset shown is the intensity versus time plot (5×10^{-7} M solution, pH=7.1 at room temperature, and PPF substrate used). [Each error bar indicates the standard deviation associated with three different substrates]

result may also indicate chemical interactions between uranyl species and a silver surface.

From the aforementioned results it is reasonable to consider a chemical bond formation between uranyl species and silver surface. Since the aqueous chemistry of the uranyl is dominated by the hydroxyl species and the affinity of hydroxyl groups for the silver surface is rather good [97], there is a possibility of development of hydroxyl-bridge between silver and uranyl moiety. However, we doubt this mechanism because in the previous studies, the symmetric stretching frequency of uranyl was observed to be unaffected in a hydroxyl linked uranyl network [132, 133]. Considering the mechanism previously proposed for the uranium-sorbed hydrous surface [116, 133] and the vibrational spectra reported for the crystalline uranate compounds [134, 135] we speculate an oxygen-bridge linkage between uranyl and silver particles. Toth et. al [133] reported the Raman spectrum of α-Na_2UO_4(one dimensional chain structure) with a symmetric stretching mode of oxy-bridged uranyl at 711 cm^{-1}. Similarly, in an infrared study of β-Na_2UO_4 (two dimensional sheet structure), Ohwada [134] assigned symmetric stretching vibration of uranyl at 710 cm^{-1}, which also has bridging oxygen. The sorption mechanism proposed by Davies et al. [135] on hydrous titania surface using uranyl carbonate is represented as;

$$M_x(OH)_2 + UO_2(CO_3)_3^{4-} \rightarrow \ M_xO_2UO_2 + CO_3^{2-} + 2HCO^{3-} \tag{4.2}$$

The product, $M_xO_2UO_2$, has uranate composition with an oxygen linkage between metal surface (M) and uranyl functional group. Based on those previous studies and the ν_1 band observed herein for uranyl loaded silver nanoparticles, it is reasonable to speculate a formation of oxy-bridge. However, further study seems worthwhile in order to ascertain the precise sorption mechanism.

With our speculation of oxy-bridge between uranyl and silver, we believe that there is charge transfer from silver surface to the central uranium atom. This results into the repulsion of axial oxygen atom and a decrease in the strength of U=O bond

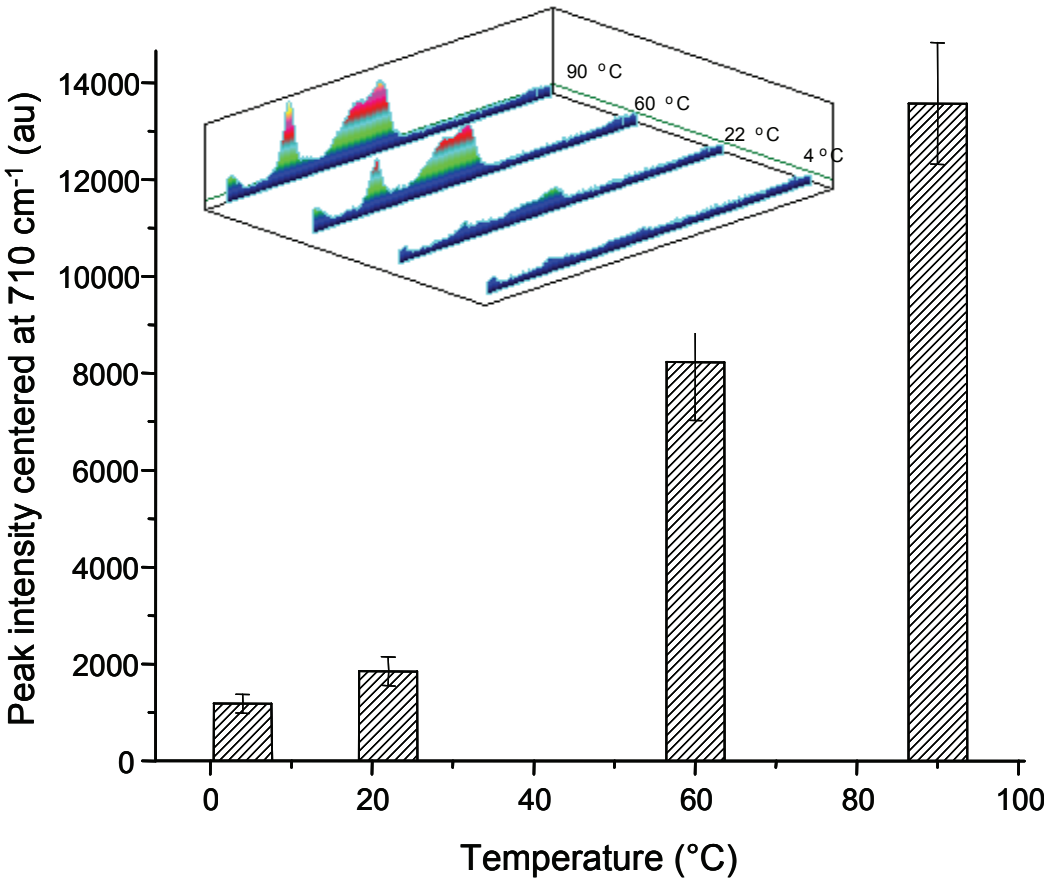


Figure 4.3: Figure showing the effect of temperature on SERS intensity of uranyl loaded silver. Shown on the top panel are the spectral profiles (5×10^{-7} M solution, pH=7.1, and PPF substrate used). [Each error bar indicates the standard deviation associated with three different spots in the same substrate]

which manifest in a lower symmetric stretching frequency of the sorbed uranyl ion. This sort of shifting of symmetric stretching frequency of actinyl group due to the accumulation of charge on the central actinide associated with ligand effect was first reported by McGlynn et al [136]. Later on, Tsushima specifically theorized this for the uranyl ion on silver colloid [115] and stated that the charge transfer from the silver to the central uranium atom weakens the axial U - O bond causing it to shift to lower wavenumber.

Studies were also performed for a wide range of pH. As shown in Figure 4.4, as the solution becomes more basic, the symmetric stretching band of uranyl around 700 cm^{-1} is continuously shifting to lower energy. However, no symmetric stretching ν peak was observed at low pH which is attributed to the oxidation of silver particle as nitric acid was used for the pH adjustment. Over the wide range of pH values, the total band shift was approximately 30 cm^{-1}. Previously, similar band-shift of uranyl ν_1 peak has also been reported in an aqueous solution of 0.1M uranyl nitrate at different pH [115]. This may be attributed to the effect of equilibrium distribution of the uranyl ion and its hydrolysis product as depicted in the previous Raman spectroscopic studies of uranyl speciation in an aqueous solution [110, 111]. Since the composition of hydroxide complexes of uranyl in an aqueous solution depends on the concentration of the solution [107, 108], it is rather difficult to relate the observed band shift in Figure 4.4 with the uranyl speciation without performing parallel complementary experiments like potentiometric titrations. Nevertheless, it is reasonable to consider the dominating $(UO_2)_3(OH)_8^{2-}$, $(UO_2)_3(OH)^{7-}$, and $(UO_2)_3(OH)^{5+}$ species corresponding to the bands 682 cm^{-1} (pH 10.9-11.6), 705 cm^{-1} (pH 7.1-9.1), and 710 cm^{-1} (pH 5.1) based on the speciation diagram previously reported in references 2 and 3. Although the observed SERS peak has been assigned based on the well-documented speciation diagram of solution speciation of uranyl(VI) [110, 111], the possibility of co-adsorption of multiple hydroxides complexes could not be ruled out because of the appearance of broad SERS peak throughout the experimental pH range. Moreover, Figure 4.4 shows that the signal intensity at pH

7.1 is relatively stronger than any other pH values. However, in our study, this does not necessarily mean that the adsorption of dominant $(UO_2)_3(OH)^{7-}$ is stronger than other species as there is a possibility of substrate oxidation, (in acidic solution) and negligible amount of precipitate formation (in basic solution).

4.3.2 Quantitative analysis of uranyl

In order to determine the detection limit (DL) of uranyl, a calibration curve is plotted utilizing the basic understanding of uranyl sorption directly on the silver surface. Due to the saturation problem associated with the detector, a narrow concentration range, from 4x10-8 M to 1×10^{-6} M, and low magnification, 50X, microscope objective was used. Figure 4.5A shows the linear fit calibration curve (R^2=0.975) with error bars shown. Each error bar indicates the standard deviation associated with three different spots in the same substrate. Using the definition of DL (DL= 3s/m), accepted by both International Union of Pure and Applied Chemistry and American Chemical Society [137], a DL of 5.8×10^{-8} M (29 ng/mL) was determined for uranyl species directly adsorbed on silver surface. Despite the calculated DL, we recorded spectra of 4×10^{-8} M (20 ng/mL) uranyl with a signal to noise much better than 3 (Figure 4.5B). Solely based on the spectra obtained, a better DL is expected. Alternatively, by developing a highly reproducible SERS substrate, the standard error in the y-intercept, s, in the definition of DL can be lowered and DL can be improved accordingly. Our approach reported herein offers a modest improvement in the SERS detection of uranyl directly on the vapor deposited silver surface compared to the previously reported result of Dai and coworkers [123]. They demonstrated 8.5×10^{-8} M as the DL of uranyl using the silver doped sol-gel SERS substrate which was impressively reported to be orders of magnitude more sensitive than an approach using the substrate prepared by vapor depositing silver surface on silica beads. Exploiting the understanding of the sorption behavior (temporal, pH, temperature factors) of uranyl on our silver-PPF substrate gain in our studies, an improvement in DL has been achieved.

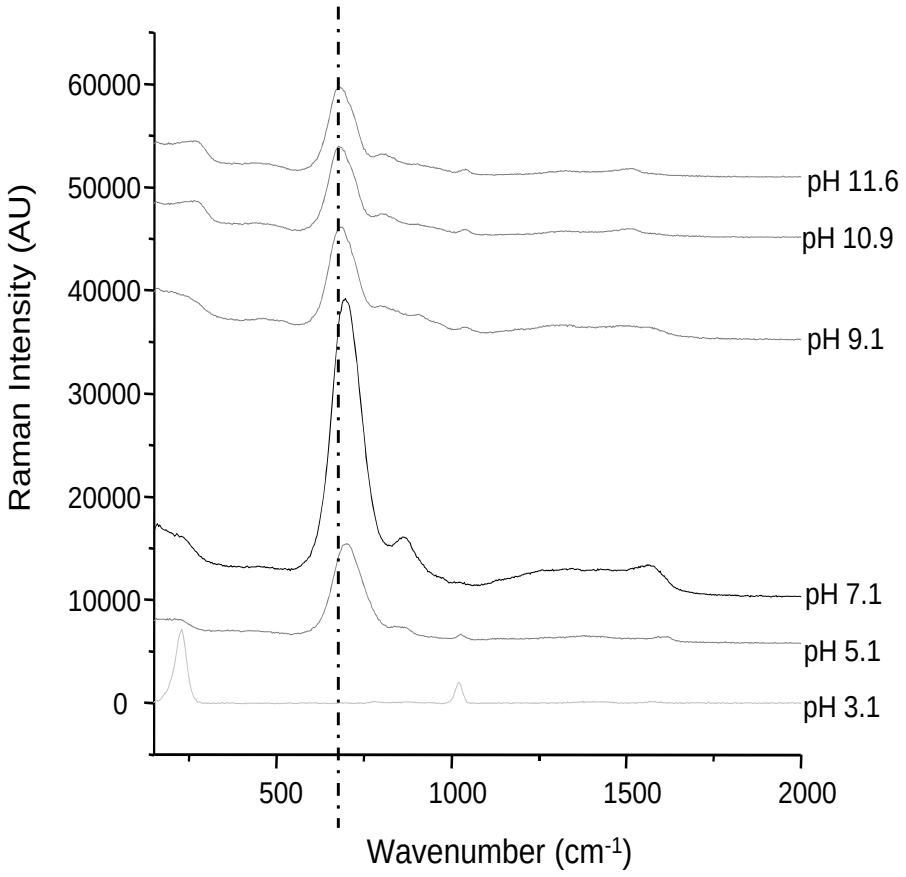


Figure 4.4: Effect of pH on the symmetric stretching frequency of uranyl (5×10^{-6} M) on the silver modified PPF substrate.

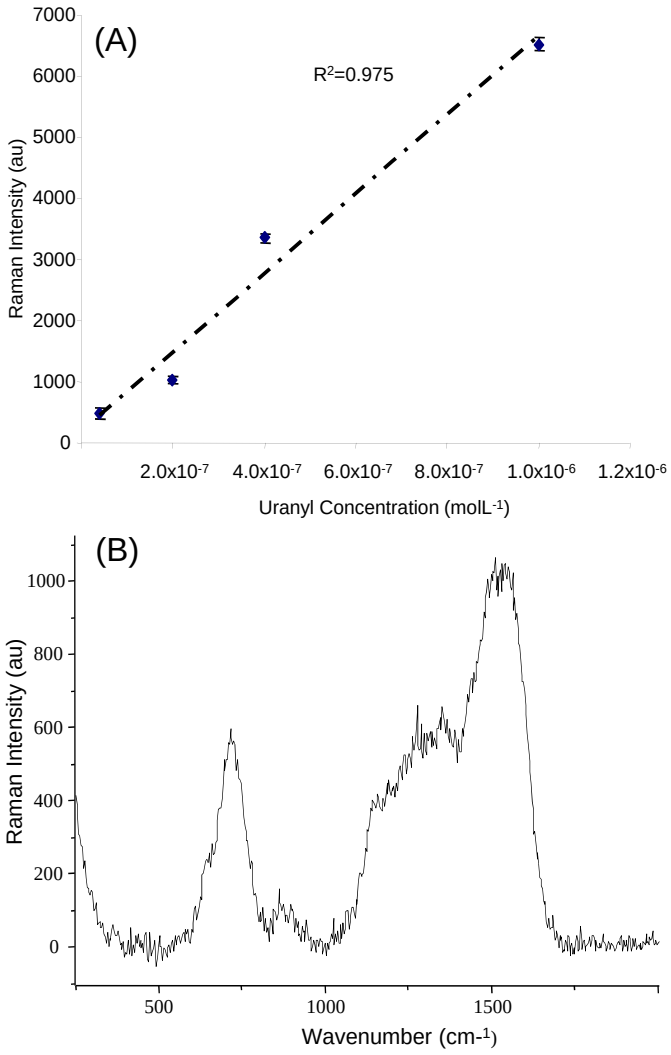


Figure 4.5: (A) Calibration curve of an aqueous solution of uranyl, and (B) SERS spectra of 4×10^{-8} M uranyl recorded. Spectra were recorded using 50x objective, 2mW laser power and 1 sec acquisition time. The temperature, delay time, and pH were 90°C, 45 minutes, and 7.1, respectively on the silver modified PPF surface.

In addition to the reported DL, the minimum mass of uranyl detected on the silver modified PPF substrate has been also estimated in our study. Considering the cast film of 150 μL of 4×10^{-8} M uranyl solution on the 12 mm size PPF substrates, 50x microscope objectives (circular laser spot size 3 μm) and with the assumption that uranyl forms a uniform layer on the sample spot, the amount of uranyl nitrate observed is estimated to be 47 attogram in the focused laser spot.

4.3.3 Prospective for nanofabricated SERS substrates in uranyl detection

SERS has garnered much attention since its discovery in 1974 by Fleischmann et al [10]. Since then the sensitivity of this information rich vibrational spectroscopy has extended to the single molecule detection for both biological and chemical systems [138, 139]. Several enhancement mechanisms were proposed in the early days of SERS, however only two mechanisms are now broadly accepted, i.e, Electromagnetic (EM) theory and Chemical Enhancement (CE) theroy [13]. EM theory is based on the collective oscillation of the free electrons, called surface plasmons, which in turn depends on the surface roughness, i.e, shape, size, and distribution of the nanoparticles. CE is based on the chemical interactions between probe molecules and the metal surface. This can be explained either as a formation of new resonant intermediate state having higher Raman scattering cross-sections, or broadening of the molecular orbitals of an adsorbate also altering the scattering cross-section [13]. It is to be noted that EM theory is chemically nonselective and should provide the same enhancement for all molecules adsorbed on the particular surface. However, this is seldom realized [21].

In our present work, the DL of uranyl is reported utilizing a random morphology SERS substrate, i.e, Ag-PPF. The previously discussed fundamental study indicates the development of chemical bond between uranyl and silver surface. Therefore, it is possible that there is a CE contribution to the overall enhancement and the growth in

signal with time is further evidence. The CE mechanism contributes only a maximum of about two orders of magnitude enhancement [13], while EM mechanism by ten or more orders of magnitude [138, 139]. Therefore, improvements in the EM portion, by rational optimization of substrate design, would potentially help in accomplishing the ultra trace detection of uranyl.

In order to investigate the feasibility of the concept, nanofabricated ellipse-sphere dimer patterns were created as examples of periodic structures using EBL and RIE (see Experimental Section and Figure 4.6). Using dimer substrates with various size nanogaps between ellipse and sphere, SERS spectra were collected and a comparison is made between benzenethiol (BT) and Uranyl. Since BT forms a well-characterized self assembled monolayer on the silver surface [140], it is chosen as the reference for EM enhancement. Figure 4.7 shows the general trend observed for BT and uranyl with regard to substrates with various nanogaps. Result shows that as the nanogap within a dimer particle is decreased from 70 nm to 40 nm, the Raman intensity increases by more than a factor of two in both cases. Note that the listed gaps are prior to depositing SiO_2 and Ag layers. Considering the BT peak at 1575 cm^{-1} as a reference, the ratio of intensity factor for 70nm:60nm:40nm nanogap is 1:1.6:2.2, while for uranyl the ratio observed is 1:1.9:2.5. This observation shows that as in BT, uranyl experience similar EM enhancement trends. The implication is that with substrate improvements uranyl detection will benefit.

As we and others have done [30], it is possible to use the known packing density of BT and a comparison between conventional Raman and SERS to estimate the enhancement factor. Using the 1575 cm^{-1} band this enhancement is determined to be approximately 3x107 for the 40 nm nanogap substrate. We are clearly orders of magnitude short of theoretical limits and with better rationally designed and lithographically fabricated substrates, the expected improvement in EM enhanement may enable the ultra sensitive detection of this environmentally significant radionuclide species.

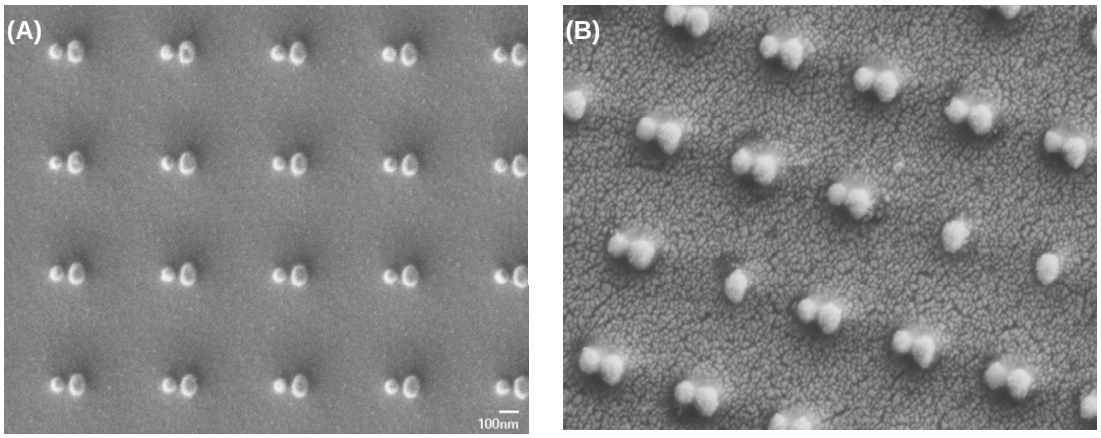


Figure 4.6: SEM of nanofabricated ellipse-sphere dimer patterns (A) without silver and (B) with 25 nm thermally vapor deposited silver.

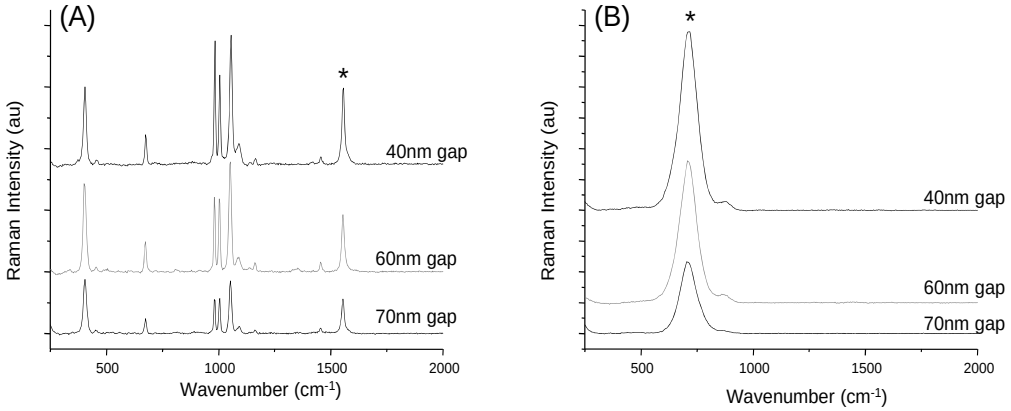


Figure 4.7: Comparisons of SERS spectra of (A) a SAM of Benzenethiol, and (B) neutral pH solution of Uranyl nitrate; on the nanofabricated ellipse-sphere dimer substrates as a function of nanogaps.

4.4 Conclusions

Two rather novel SERS substrates, i.e PPF and nanofabricated "ellipse-sphere dimers" are utilized for the study of sorption phenomenon of environmentally significant radioactive species on the silver surface. Results support that there appears to be a chemical interaction between probe molecules and metal surface. Exploiting this understanding, SERS of uranyl is reported as low as 20 ng/mL on silver deposited PPF substrate without any surface modifications. Moreover, well-defined nanofabricated SERS substrates are created and put forward as a potential alternative approach with the potential for ultra sensitive detection of uranyl.

4.5 Acknowledgements

This research was supported by the US Environmental Protection Agency STAR program under grant EPA-83274001 with the University of Tennessee. Nanofabricated substrates were created at Oak Ridge National Laboratorys Center for Nanophase Material sciences, sponsored by the Scientific User Facilities Division, Office of Basic Energy Sciences, U.S. Department of Energy. The authors would like to thank Dr. George Schweitzer of UT-Knoxville for providing uranyl nitrate hexahydrate.

Chapter 5

Stamping High-Aspect-Ratio Plasmonic Nanoarrays on SERS-supporting Platforms

Chapter 5 has been accepted for publication in a peer-review journal, *Journal of Raman Spectroscopy*. The article describes the use of nanotransfer printing to stamp out electron beam lithography created plasmonic nanofeatures on various substrates for better SERS enhancement.

5.1 Introduction

There is a considerable interest in the optical properties of metal nanoparticles, mostly due to their ability to create intense localized surface plasmon (LSPs) fields. However, due to the nanoscale dimensions, controlled fabrication of rationally-conceived special nanostructures was quite difficult until recent advances in nanoscience and nanotechnology [30,63,141]. Conventional lithographic techniques that emerged from microelectronics are now in widespread use in the fabrication of nanostructures for research in both physical and biological sciences. Currently, there is substantial

interest in alternative non-conventional techniques like nanoimprint lithography [142, 143], soft-lithography [144, 145], near field optical lithography [146, 147], etc. These non-conventional techniques have garnered attention in creating fine nanostructures over a large area at a relatively very low cost.

Surface-enhanced Raman scattering (SERS), first discovered by Fleischmann et al. [10], and Jeanmarie and Van Duyne [11] in the 1970s, exploits near-field plasmonic effects [139, 148, 149]. Molecules located at the vicinity of the roughened surfaces, therefore, experience different spatial field intensity depending on the morphology and arrangement of nanostructures. So far, there have been several theoretical and experimental studies performed on the plasmonics of various shape, size, and distribution of metal nanoparticles [14, 18]. More recently, a good deal of understanding emerged on the substrate plasmonics. A number of studies have shown that substrate dielectric property alone has major contribution on localized surface plasmon resonance (LSPR) frequency [150–153]. This understanding has opened up new challenges in SERS. Since most of the uniform and higher efficiency SERS substrates are nanoparticle-embedded planer surfaces, the proper selection of dielectric materials could notably alter Raman intensity, regardless of a nanoparticle.

Typically, metal nanoparticle or plasmonic surface is fabricated by top-down nanofabrication [154–156] or bottom-up self-assembly approaches [157, 158]. Nevertheless, controlled nanostructured arrays having larger field enhancement and reproducible SERS signals are usually fabricated via top-down approach [141]. Electron beam lithography (EBL) is a burgeoning top-down technique for SERS research. However, the access of EBL to general users is obstructed by the exceptionally high cost of EBL instrumentation and its limitation to specialized materials. Therefore, to produce SERS-active surface at a relatively lower cost on a desired substrate, it is obligatory to develop a novel nanolithography approach that can possibly augment EBL in plasmonic research. Herein, we recognized that nanostructures created on a silicon stamp are robust to facilitate the stamp-and-repeat advantage and compatible with surface modification chemistry (see below).

Silicon stamps were fabricated by EBL and reactive ion etching (RIE). These silicon based nanotransfer printing (nTP) stamps involved the extensive optimization of unique fabrication conditions such as EBL exposure dose, development time, liftoff process, and etching protocol. The stamps contain features with a dimension of as small as 150 nm diameter to large 5 x 5 μm^2 size aggregates, and have relief pillars height of 375 nm. These SERS-active nanofeatures were stamped out, for the first time, on three most commonly used research materials, i.e. PDMS, SU-8 photoresist, and glass. The materials under study were selected on the basis of their extensive use in micro- and nano-technology and distinct refractive indices. The process was optimized for high fidelity transfer printing. Results showed that nTP-created nanoparticles retain their inherent SERS activity and also are consistent with the recently cited substrate dielectric effect and our theoretical calculations. Additional attributes of this work are highlighted by brief discussions on nanogap manipulation and SERS-active fiber facet. In general, the current work develops nTP as a promising route to integrate EBL created nanoarrays on various surfaces for improved SERS enhancement. It also shows potential towards the development of microanalytical plasmonic devices, such as lab-on-chip, fiber optics, etc. by integrating nanoparticles on various dielectric films.

5.2 Experimental

5.2.1 Materials

Prime grade silicon wafer (orientation100), glass slides, SU-8 50 resist, and sylgard 184 silicone elastomer were purchased from Wafer World Inc., Fisher Scientific, Microchem Corporation and Dow Corning Corporation, respectively. Silver shot (99.99%, 2-3 mm diameter) and gold coins were purchased from Alfa Aesar. Rhodamine 6G (R6G) was purchased from Allied chemicals and benzenethiol (BT) from Acros chemicals. All test solutions were prepared in 18 MΩ Deionised water (Barnstead, E-Pure).

5.2.2 Nanofabrication of Silicon Pillars and Metal Deposition

Silicon pillars or "stamp" were created using EBL and RIE. The detailed procedure is explained elsewhere [29, 30, 141]. Briefly, 300 nm thick positive resist, ZEP 520 A (Zeon Chemicals, KY), was spin coated onto the silicon wafer at 6000 rpm for 45 seconds, baked at 180∘C for 2 minutes and then placed under vacuum in the EBL system. The resist was patterned by EBL (Jeol JBX-9300, 100 keV) and then developed in xylenes for 30 seconds and rinsed with isopropanol.

For the lift-off procedure, 10 nm of chromium was vapor deposited onto the nanopatterns using a dual gun electron beam evaporation chamber (Thermonics Laboratory, VE-240). Following lift-off, silicon wafers were etched to produce 375 nm silicon posts using an Oxford Reative Ion Etcher. After etching, chromium on the substrate is removed using a chrome etchant, CR-14S (Cyantek Corp, CA). The silicon stamps thus created were exposed to releasing agent, heptadecafluoro-(1,1,2,2,tetrahydrodecyl)-tricholorosilane (Gelest Inc, PA), in a vacuum desiccator for an hour prior to the physical vapor deposition of silver (Cooke Vacuum Product).

5.2.3 Substrate Preparation and Nanoscale Transfer Printing

PDMS elastomer was prepared by mixing sylgard 184 curing agent and its elastomer in a 1:10 (w/w) ratio. The mixture was then degassed using vacuum dessicator and then spin coated on a clean silicon wafer at 200 rpm for 30 seconds. The solution was finally cured in an oven for an hour at 70°C. Similarly, SU-8 50 resist was spin coated on a clean glass slide at 3000 rpm for a minute, prebaked at 90°C for 20 minutes, exposed to 365 nm UV radiation for 4 minutes and then post baked for 10-15 minutes. Glass slide in the SERS study were used as it was obtained from the vendor. Cured PDMS elastomer and SU-8 resist were then exposed to UV ozone for 5 minutes while glass slide was treated with 30:70 (v/v) mixtures of hydrogen peroxide and sulfuric acid for 30 minutes at 80°C. Each substrates were then treated with a

"griping" reagent, 5x10^{-3} M solution of 3-mercaptopropyl trimeoxysilane(3MPTMS) in acetone (for PDMS) or in toluene (for glass, and SU-8), for 30 minutes. Silver coated silicon stamps were then brought into contact to the final substrate using in-house built pneumatic device. The stamp was finally removed leaving behind metallic nanofeatures on the final substrate.

5.2.4 Scanning Electron and Atomic Force Micrographs

Scanning electron micrographs (SEMs) of all nanofeatures were taken using LEO 1525 scanning electron microscope in a secondary electron detection mode. Low voltage (1.5 kV field emission gun) was applied to reduce charging effect. Due to the excessive charge build up, atomic force microscope (AFM) was used to characterize nanofeatures on SU 8 resist. All AFM images were taken in AC mode in air using Asylum research AFM. Commercial silicon AC160 cantilever tips (Olympus) with a spring constant of 2.45 N/m were used. Tips were tetrahedral in shape and the tip radius of curvature was less than 10 nm.

5.2.5 SERS Measurements

All SERS measurements were acquired using a LabRam Spectrograph from JY-Horiba using 633 laser excitations. Details about the optics can be found elsewhere [128]. For SERS detection, substrates were drop coated with 20 μL solution. However, for BT, extra rinse-off step was carried out to remove unbound analyte from the nanoparticles' surface using de-ionized water. In each case, 25 spectra were acquired over 400 μm^2 area. Baseline corrections were done in order to correct the optical background signal from the substrate. All spectra were recorded using dimer arrays of 300 nm x 300 nm x 30 nm (width x height x thickness) triangles or circles (300 nm diameter x 30 nm thickness), referred as "bowtie" or "dumbbell" throughout, 50X microscope objective, 1 mW laser power, and 2 sec acquisition time unless otherwise mentioned.

Test solutions used in SERS experiments were 5 x 10^{-6} M R6G and 5 x 10^{-4} M BT, the latter creating a self assembled monolayer on the metal surface.

5.2.6 Theoretical Calculations

We have performed simulations using CST Microwave Studio [159], which implements a Finite Integration Technique [160] to solve Maxwells equations. The calculations were performed in the time domain, and spectral information was obtained via discrete Fourier transformation. The grid mesh for both configurations was 2nm, and periodic boundary conditions were employed in directions perpendicular to **k**. The dispersion of the silver has been incorporated via experimentally determined values of the optical constants [161].

The model geometries under investigation are shown in Figure 5.4a, for the bowtie (left) and the dumbbell (right) configurations. The unit cell has dimensions a=1100 nm and b=450 nm for both cases. For the bowtie, w=650 nm and v=300 nm, while the gap is g=50 nm. For the dumbbell, the diameter is d=300 nm and the gap is g=50 nm. The silver nanoparticles are assumed to have thickness p=30nm. The arrays reside on a substrate with refractive index nm. In particular, we have considered the following values: PDMS n_m=1.47, glass n_m=1.51, and SU8 n_m=1.59. All three materials are assumed lossless. The unit cell is illuminated by a normal plane wave at λ_0=633 nm, with electric field polarized perpendicular to the dimer axis.

As a figure of merit, we defined the volume-integrated modulus of the electric field as an indicator of the average near field a Raman active molecule may feel. The volume is defined as a right parallelepiped, where two faces are the substrate/particle interface and the top of the nanoparticle dimer. The remaining four faces are shifted from the outermost locations on the dimer surface by a distance t=10nm. For the bow tie, the base is (2t+w)x(2t+v), and height is the particle thickness p. Equivalently for the dumbbell, the base is (2t+2d+g)x(2t+d), and the same height. Thus, the

figure of merit F is defined over the appropriate volumes as

$$F = \frac{1}{V}\int_V |E(x,y,z)|dV \tag{5.1}$$

5.3 Results and discussion

5.3.1 nTP Process Description

The current approach of incorporating plasmonic nanoarrays on dielectric substrates involves (a) defining nanoscale features on a silicon wafer (referred as a "stamp") and chemically modifying the stamp for facile release, (b) physical vapor deposition of a metallic thin film on stamp, (c) bringing the stamp and the chemically modified substrate into physical contact, and (d) removing the stamp to leave behind nanostructured metallic features on the substrate. Schematics of the process design in shown in Figure 5.1. Initially, EBL and RIE were used to define high-aspect-ratio nanofeatures on the silicon wafer (see insert in Figure 5.1). EBL can pattern arbitrary features with a resolution of approximately 10 nm [63, 141]. Silicon stamps were then treated with fluorinated silane prior to the metal deposition. The presence of fluorinated silane interface between the relief pillar and the metallic film weakens the adhesion between the latter two and facilitates the transfer of metallic discs [65]. Three chemically and physically distinct dielectric materials, i.e., PDMS, glass, and SU-8, were chosen for the study.

The nTP technique depends on the interfacial chemical reactions that occur during the physical contact between stamp and final substrate [65, 66]. To facilitate surface chemistry, hydroxyl groups were created on the substrate of interest. PDMS elastomer and SU-8 photoresist generate a hydrophilic surface upon plasma treatment, while the glass substrate was soaked in a 3:7 volumetric mixtures of hydrogen peroxide and concentrated sulphuric acid. Subsequently, substrates were treated with 3MPTMS to facilitate the co-condensation reaction (see appendix, Figure A.1). This results

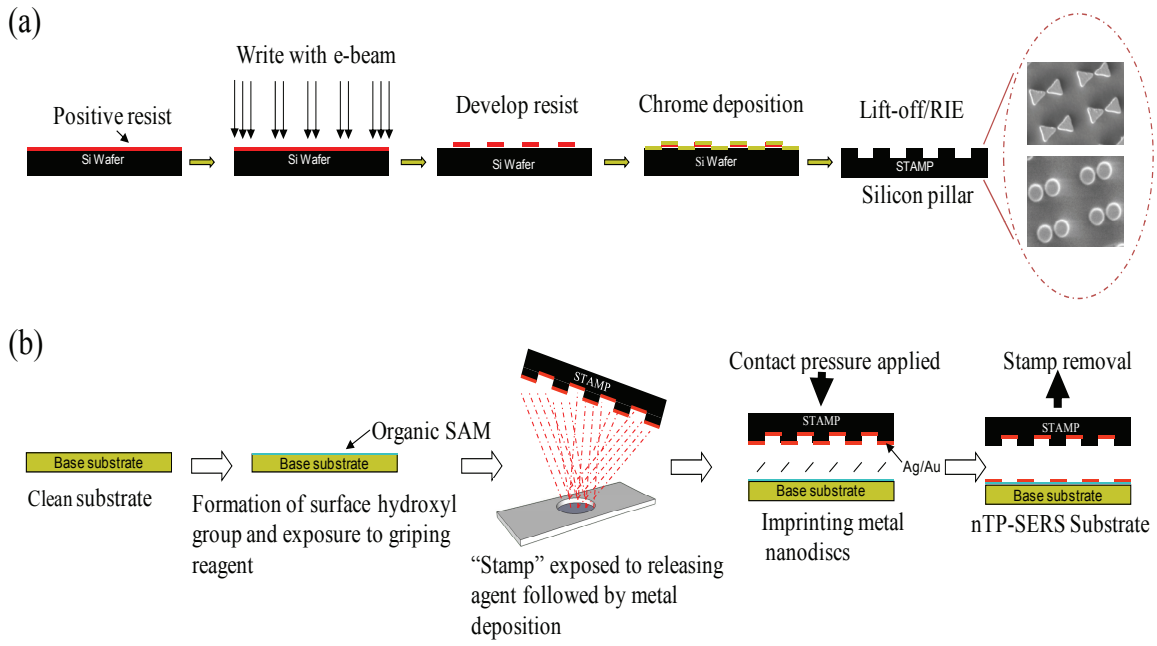


Figure 5.1: Schematic depiction of the procedure for incorporating nanofeatures on various material surfaces: (a) conventional nanofabrication (e-beam lithography/reactive ion etching) in creating relief nanopillars on silicon wafer, and (b) nanotransfer printing approach. Shown in the insets are SEMs of EBL/RIE fabricated silicon pillars.

in the formation of a layer of 3MPTMS with thiol group terminated outward [162]. Since thiol groups bind covalently with coinage metals, when the stamp is brought into physical contact with the 3MPTMS, covalent interactions can assist the transfer process.

5.3.2 nTP Process Optimization

Using a rigid silicon stamp, plasmonic nanoarrays were successfully stamped out on both soft and rigid substrates. For soft PDMS elastomer, external pressure was not needed to bring the stamp and substrate into conformal contact. For rigid substrates like glass and SU-8 resist, adjusting transfer pressure was important for successful nTP. In case of SU-8 resist, we empirically determined that ∼75 psi contact pressure was sufficient to facilitate transfer process while for glass substrate ∼150 psi was required. Contact pressure was monitored by an in-house built pneumatic device. The pneumatic device used in our experiment was composed of a nitrogen tank connected via plastic tubing, with an in-line pressure gauge, to an inverted gas tight glass syringe (see appendix, Figure A.2). The contact pressure reported herein is the amplified pressure per unit area exerted to the stamp and is estimated on the basis of pressure applied per unit area to the syringe plunger and the area of the stamp, which was kept as small as possible to minimize the adverse effect of unevenness.

In addition to the external pressure, contact time between the stamp and the substrate was shown to be important to achieve high transfer success rates. Unlike instant transfer printing of electronic circuits (<15 sec) [65], at least 2 hours of physical contact was imperative for the defect-free transfer printing of metallic nanoarrays. This is possibly due to small contact area and geometry of isolated nanoparticles. Moreover, strong cohesive force between noble metal particles could be another possibility in making a significant difference on transfer printing rate between integrated circuits and particulate patterns. We have shown representative non-optimal condition transfer printed bowtie arrays on PDMS and SU-8 respectively,

with several defects at contact time less than 30 minutes in the supporting information (see appendix, Figure A.3). On the other hand, successfully integrated bowtie arrays on various material surfaces are shown in Figures 5.2b-5.2d along with 30 nm silver modified silicon stamp (Figure 5.2a). In an optimal transfer conditions, we observed less than 1% missing nanotriangles or nanocircles in a 50 μm x 50 μm array. However, minor other defects like scattered silver dots were occasionally observed in a soft PDMS substrate, while it was not the case in rigid substrates.

5.3.3 SERS Detection

The stamping technique employed to integrate metal nanoparticles on three distinct dielectric substrates were tested for SERS detection. Studies were carried out using extended arrays of "bowtie" and "dumbbell" structures. All the adjustable parameters on EBL-created stamps were kept constant whereas the refractive indices of SERS substrates were different, i.e, PDMS elastomer (1.47) [163], glass slide (1.51) [164], and SU-8 resist (1.59) [165]. Self assembled monolayer (SAM) of benzenethiol BT and 5 x 10^{-6} M R6G were used as SERS probes. Raman peak intensities of BT and R6G harvested from respective SERS substrates are shown in Figure 5.3. Each data represents average SERS intensity collected from 25 different spots within 20 x 20 μm^2 areas. The average values, instead of the best intensity, were considered in order to minimize possible errors in SERS intensity that could have resulted from minor variations, including the occurrence of satellite particles [166] on soft substrate, in the fidelity of the transfer process. For both probe molecules, Raman signals from the high refractive index SU-8 substrate were stronger relative to PDMS or glass substrates. Based on refractive index alone, one might expect that a glass substrate would give a larger response than the PDMS, but that was not observed. This is possibly due to the different surface property of PDMS elastomer. PDMS is a cross-linked polymer having an uncross-linked layer on the surface. The presence of this layer could possibly result into the formation of subsurface embedded nanoparticles [48]. In other words,

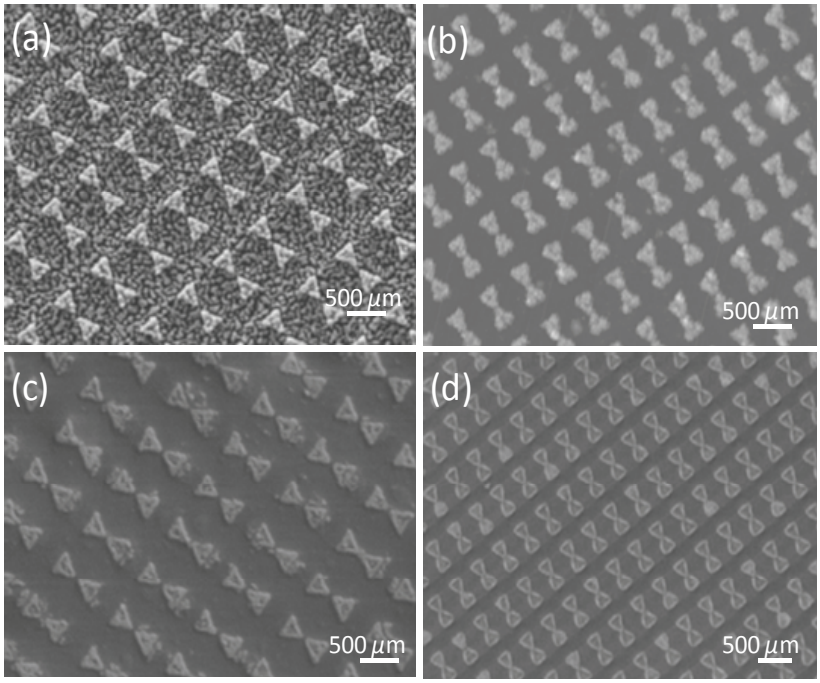


Figure 5.2: Micrographs (AFM, b, SEM a, c, and d) representing transfer printing of metallic nanoarrays: (a) Silver modified nanofabricated silicon pillars prior to stamping. Nanotransfer printed bowtie silver array on (b) PDMS, (c) SU-8, and (d) glass slide.

unlike glass and SU-8 substrates, nanoparticles on PDMS elastomer may be partially submerged into the polymer matrix and are exposed to more of the substrate. As a result, the nanoparticles have plasmon frequencies that are altered due to the change in the local dielectric, and hence act differently in SERS. This sort of understanding based upon effective refractive index considerations has been previously reported by Novo et al. [152].

We have investigated the possibility of the nanoparticles submerging into the substrate theoretically using classical electrodynamics (simulation details in previous section on Theoretical Calculations). The electric field modulus was integrated over the volume of a rectangular prism that enclosed the nanoparticle dimer and the spatial region between. Figure 5.4b displays the results for the bowtie and dumbbell structure on glass, PDMS, and SU-8. The trend observed theoretically is consistent in order with the experimental results shown in Figure 3 for both probe molecules. Figure 4c shows the effect on the integrated field generated by sinking the particles into a PDMS substrate. For both dimers, there is an initial increase followed by a decline. This results from an increase in the effective refractive index of the nanoparticles, corresponding with a shift of the resonance and an increase in the plasmon field, coupled with a decrease in integrated volume (only spatial regions above the substrate were included to represent regions accessible to molecules). A maximum is found at a submersion depth of ∼5 nm for the bowtie and ∼10 nm for the dumbbell. It is these max values that are reported in Figure 5.4b for the PDMS and suggest that the arrays are submerged in this substrate. Note that if the particles were restricted to be on the surface, then the results for glass and PDMS would be reversed following the expected trend with refractive index of the substrate. An additional consideration for PDMS-based substrates is that the elastomer is a common solid phase extraction material and can enhance nanoparticle accessibility for analytes [48, 49, 167]. Accessibility could also include the submerged side as well, although not considered in the enhancement factor evaluation performed herein (see below).

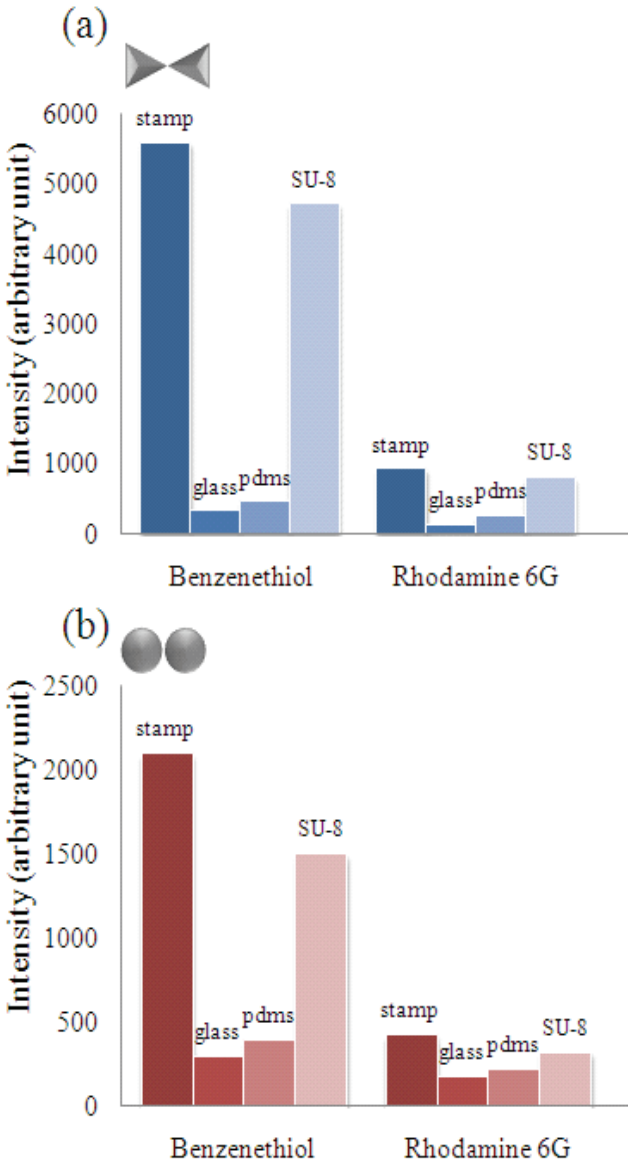


Figure 5.3: SERS intensities of Benzenethiol peak centered at 1575 cm^{-1} and Rhodamine 6G peak centered at 763 cm^{-1}, with respect to various underlying substrates using extended arrays of silver (a) bowtie, and (b) dumbbell.

Generally speaking, regardless of nanoparticle morphology, nTP integrated nanostructures are aware of the underlying substrate properties and so created SERS substrates can exploit this to optimize performance. In other words, the harmony between nTP-created SERS substrates and recently quoted substrate dielectric effect provides new insight in the selection of appropriate substrate and/or nanoparticles morphology for improved sensitivity.

Using an extended array of silver bowtie, SERS reproducibility of silicon stamp and corresponding nTP pattern were investigated. In each case, BT loaded extended arrays of silver bowtie were mapped over 20 x 20 μm^2 area in a 5 μm subsequent step. Based on our observation, the relative standard deviation (RSD) of about 9% and 23% were recorded for silicon stamp and corresponding pattern on SU-8 substrate, respectively. Relatively higher RSD of nTP-created SERS-active surface is presumably due to the minor defects originated during transfer printing. Shown in Figure 5.5a (left) are superimposed spectra of BT collected from 25 different spots on silver modified silicon stamp. Each color pixel in Figure 5.5a (right) gives information on BT peak intensity centered at 1575 cm^{-1}. Similarly, Figure 5.5b shows the result collected from a SU-8 substrate.

It is possible to use the known packing density of BT and a comparison between conventional Raman and SERS to estimate the SERS enhancement factor (EF) [28–30]. EFs of all nTP-SERS substrates employed in this study are estimated. The details of the procedure we followed herein to calculate EF are presented in our prior publication [30]. With reference to the 1575 cm^{-1} peak, we determined that the average enhancement of nTP-created SERS substrates varied by more than one order of magnitude, depending on the nature of supporting-film (Table 5.1). Although the highest EF observed in our study is 5.37 x 10^7, with better rationally designed and nanolithographically fabricated nanoarrays and/or a selection of other suitable substrate, significant improvement in EM enhancement may be possible.

It is now well established that SERS signal can be harvested from a variety of substrates, ranging from a single-nanoparticle to periodic arrays or nanoaggregates

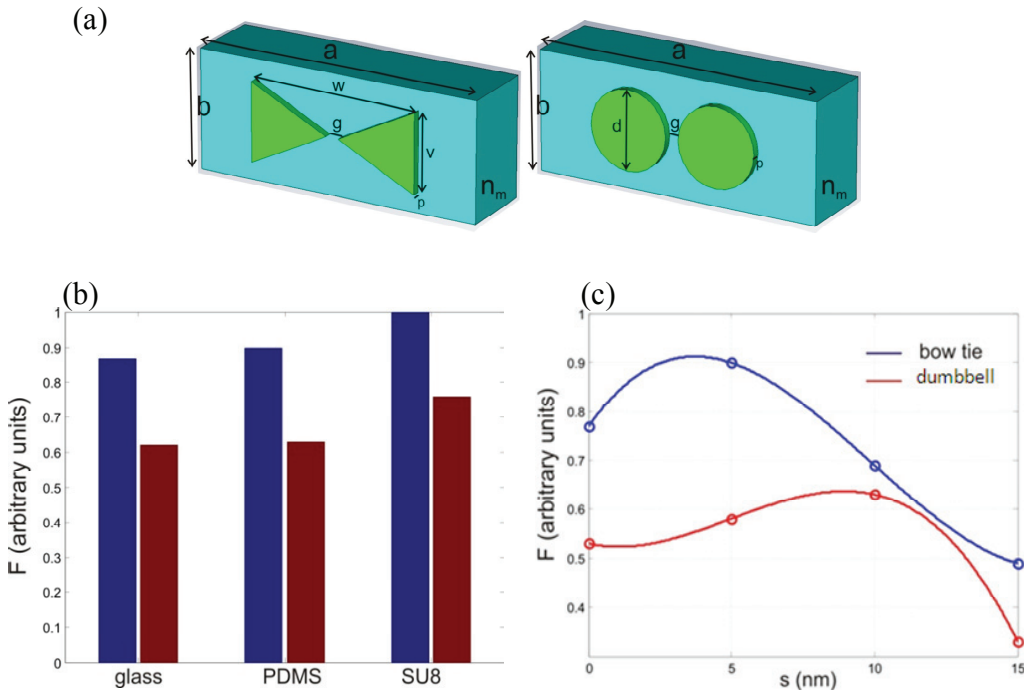


Figure 5.4: Theoretical calculations of the figure of merit: (a) Geometry of both nanoparticles configurations within the unit cell, where a=1100 nm and b=450nm. The nanoparticles are composed of silver and reside on a material substrate with refractive index nm. (Left) bowtie: w=650nm, v=300nm, g=50nm, p=30nm. (Right) dumbbell: d=300nm, g=50nm, p=30nm. (b) Figure of merit F for glass, PDMS, and SU8 reported relative to the maximum SU-8 value. Blue corresponds to the bowtie and red corresponds to the dumbbell configuration; (c) the variation of F as a function of the sinking parameter s in PDMS. Again results are reported relative to the SU-8 bowtie value.

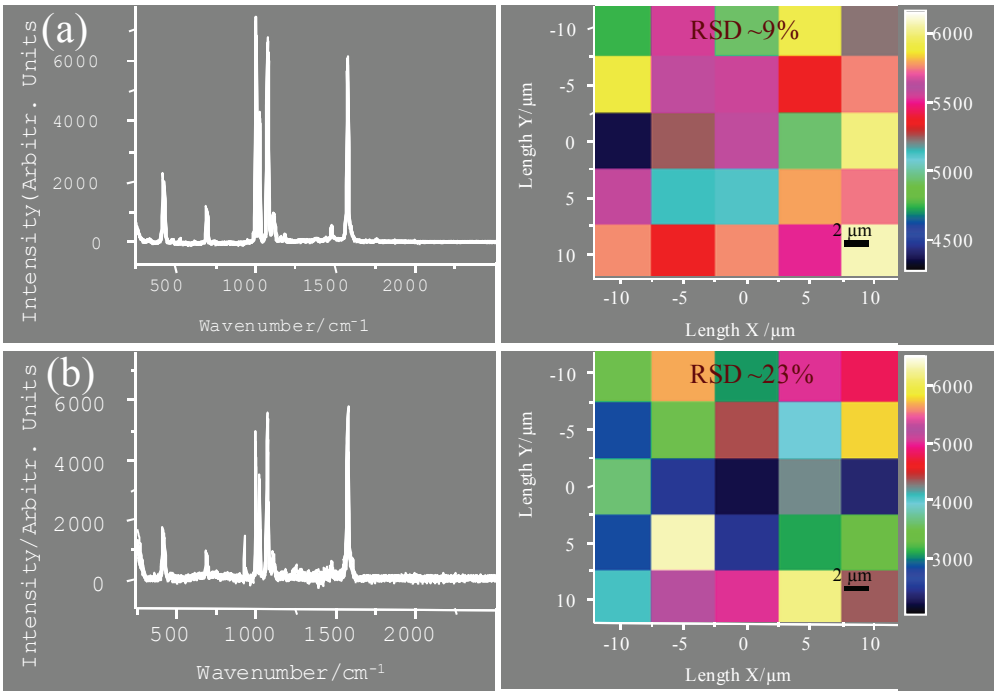


Figure 5.5: SERS spectra of Benzenethiol collected from (a) silver modified silicon pillars (RSD ∼9%), and (b) similar nanopattern on SU-8 surface (RSD∼23%). Figures shown on the right hand side are the spectral mapping of probe molecules over 400 μm^2, and on left hand side are superimposed spectra.

Table 1: Average SERS enhancement factors of dimer nanoarrays stamped on various supporting films.

Nanopatterns	Supporting films	Enhancement Factor
Bowtie antenna	SU-8	5.37×10^7
	PDMS	4.10×10^6
	Glass	2.91×10^6
Dumbbell antenna	SU-8	1.19×10^7
	PDMS	4.0×10^6
	Glass	2.29×10^6

of various morphologies. In order to demonstrate the versatility of nTP, a range of planar SERS substrates were created on both soft and rigid substrates. Shown in Figures 5.6a and 5.6b are transfer printed single-nanoparticle (diameter = 150 μm) and 4 x 4 arrays of similar size nanoparticles on a glass surface. Such structures are important, especially in understanding the plasmonic behavior of metal nanoparticles, both experimentally and theoretically. On the other hand, Figure 5.6c shows a scanning electron micrograph of a relatively large square-pattern integrated on PDMS substrate. A large 120 μm x 120 μm square-pattern was cloned with two different kinds of lithographically designed nanoaggregates (LDNAs). Relatively less dense LDNAs were cloned at the center of a macropattern forming the shape of a "T" and were surrounded by replicas of denser LDNAs (Figures 5.6c-5.6d). Our recent LDNAs-SERS studies showed that less dense nanoaggregates produce relatively stronger SERS intensity than denser one [141]. To demonstrate the legitimacy of nTP-created relatively large SERS-active surfaces, the entire square pattern on PDMS were mapped. A significant difference in the SERS intensity was observed between two LDNAs. Results showed that the average SERS intensity of the T-cloned nanoaggretes is roughly three times stronger than the surrounding nanoaggregates (Figures 5.6e-5.6f). The observed spectral trend is consistent with the previous

LDNAs-SERS result [141] and hence demonstrates the ability of nTP-created patterns to retain their inherent SERS activity over large areas.

5.3.4 Nanogap Manipulation

More than three decades after the discovery of SERS, fundamental challenges still exist. One of the most significant involves the so called "nanogap effect" [37,168–172]. Several theoretical studies have predicted that SERS enhancement field strongly depends on the spacing between plasmonic nanoparticles with a dramatic field enhancement when distance between nanoparticles decreases to near molecular dimensions [168, 169, 172]. However, most recently several groups have published results on maximum SERS enhancement with a capability of single-molecule detection from a variety of nanostructures, ranging from "just touching" dimer [37] to 30 nm-spaced one-dimensional gold disc [170]. Such diverse SERS phenomenon can be perplexing to the scientific community. This is partly associated with the difficulty of routinely delivering nanoparticles with controllable sub 10 nm interparticle spacing using existing nanofabrication techniques. Therefore there is a need for a simple, cost-effective and a handy protocol that enables the manipulation of nanogap reversibly. In this work, bowtie arrays stamped onto a stretched PDMS film followed by the physical relaxation of a polymer demonstrate the feasibility of nanogap reduction. Arrays of 150 nm x 150 nm x 30 nm (width x height x thickness) gold triangles with 100 nm intra- and 300 nm inter-dimer spacing (prior to gold deposition) were transfer printed onto ∼150% stretched PDMS elastomer. Bowtie array-incorporated stretched PDMS was then physically relaxed to its normal position (∼100%) in an in-house built stretching/relaxing device. Figure 5.7 shows that on relaxing stretched PDMS, there is a considerable reduction of nanogap in bowtie arrays. The concept presented here opens up the possibility to monitor nanogap spacing without any rigorous step and hence facilitate the better understanding of plasmonic effects related to nanogap. Efforts to better control gap spacing and environment are ongoing in our laboratory.

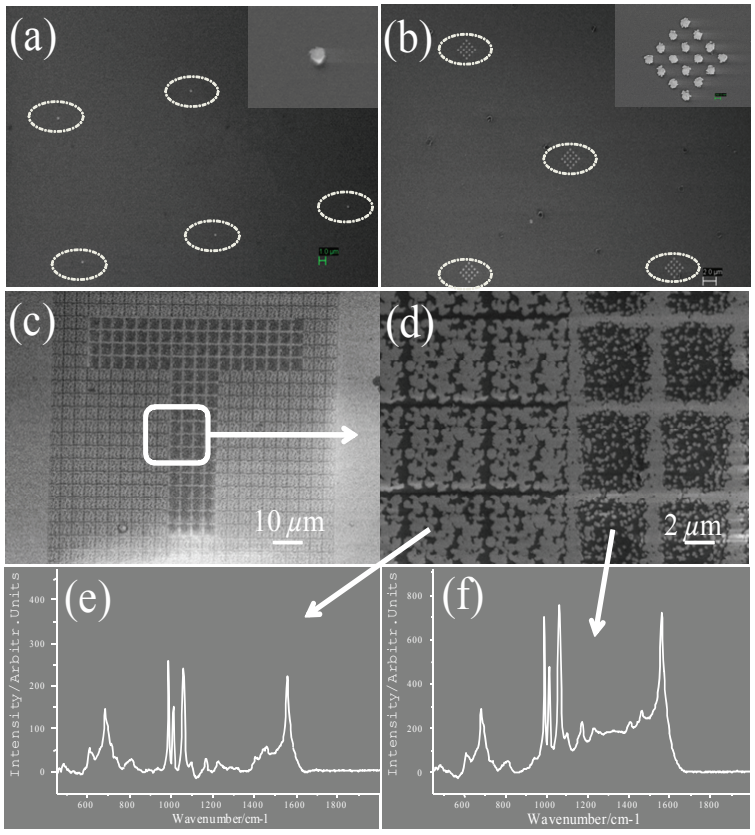


Figure 5.6: Demonstrated an ability to integrate a single-particle to LDNAs macropattern on various substrates; (a, b) single-particle and 4 x 4 arrays of silver nanoparticles on glass substrate. (c, d) relatively large square patterns, consisting of two different types of LDNAs, on a PDMS substrate. (e, f) typical SERS spectra of BT harvested from two different clones.

5.3.5 Nanoarrays on a Microfiber Facet

There is also a significant interest towards the development of intrinsic SERS-active fiber optics, which can be utilized for both biomedical and remote sensing applications [173, 174]. Although nanolithographic techniques like EBL and nanosphere lithography are broadly used in creating SERS substrates, such techniques are not straight forwardly adaptable to the fiber optic geometry. In this work, as a proof of concept, silver arrays defined on silicon stamp were successfully incorporated on a micro-fiber optic facet (core diameter = 400 μm). It is noteworthy that in order to allow conformal contact between stamp and a fiber optic, special attention is required on surface polishing protocol. Briefly, a small piece of Teflon disc (2 cm thick and 4 cm diameter) was drilled through using a drill bit of an optical fiber outer diameter size. The optical fiber was then carefully fitted into the through hole of the teflon. In order to fix the fiber optic firmly, one side of the Teflon was coated with epoxy glue while the uncoated side was sequentially polished using various size polishing grits, i.e., 400, 600, 1200, 2400, 4000 followed by 0.05 micron alumina slurry. The polished fiber optic surface was then brought into conformal contact to facilitate transfer printing (see Appendix, Figure A.4). Figures 5.8a and 5.8b are respectively, transfer printed silver arrays and silicon stamp prior to silver deposition. Our result emphasizes the significance of stamping protocol to integrate metal nanoparticles on a fiber optic facet, without any harsh step. The concept presented here would support the development of SERS-active fiber optic sensor. Similarly, EBL created nanoparticles can be incorporated onto micro/nanofludics channel and other related photonic devices.

5.4 Conclusions

For the first time, we incorporated surface chemistries mediated plasmonic arrays on three distinct dielectric surfaces using EBL crafted silicon relief pillar. To facilitate

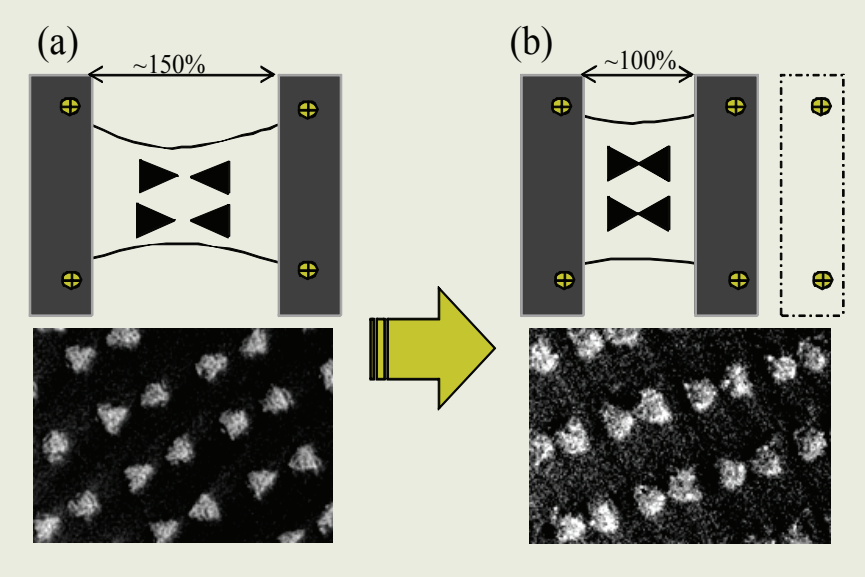


Figure 5.7: Demonstrated nanogap reduction by physical manipulation of a elastomer: SEMs of bowtie arrays stamped on (a) a stretched PDMS, and (b) the same pattern after relaxing elastomer. Figures shown at the top are schematics of the gap manipulation.

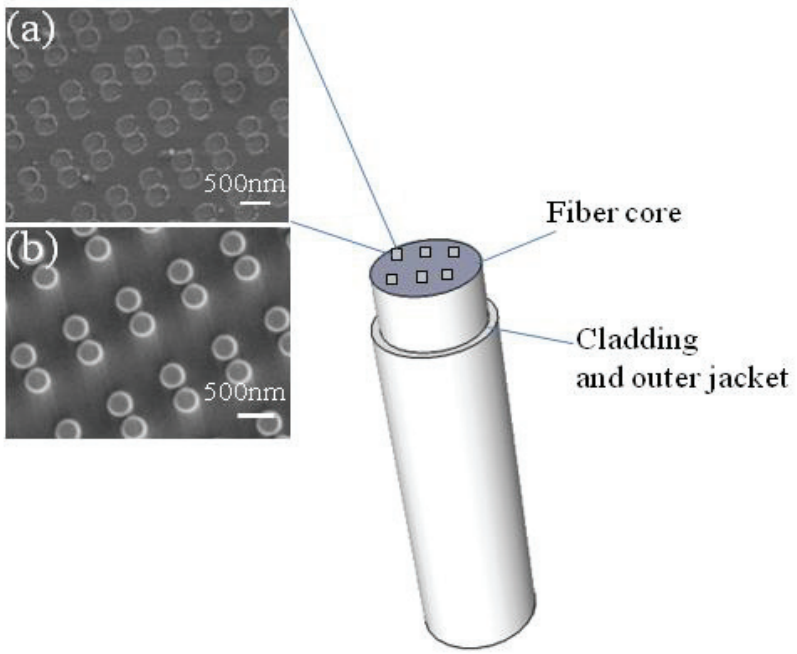


Figure 5.8: SEMs of dumbbell arrays: (a) integrated on the fiber optic facet, (b) original silicon relief pillars prior to silver deposition.

transfer printing of an isolated nanoparticle, careful optimization is required to bring stamp and substrate into conformal contact. These nTP-created plasmonic nanoarrays on dielectric surfaces retain their ability to amplify Raman signals. Both experimental and theoretical results showed that SERS enhancement varies from substrate-to-substrate, and nTP-created SERS substrates exploit this property for better field enhancement. Current work also introduced SU-8 based SERS substrate. This SERS substrate has relatively higher enhancement magnitude than concurrently studied conventional glass and PDMS substrates. The technique can also be easily extended to other dielectric surfaces for better field enhancement. An additional attribute of current approach is towards the incorporation of metal nanodisc on unconventional environments like fiber optic, lab-on-chip, etc. for in situ SERS sensing and other related plasmonic applications.

Chapter 6

Concluding Remarks

The use of SERS for routine chemical analysis is still in its early stages. Several fundamental and applied researches are undergoing in different research groups. Since SERS mainly relies on electromagnetic enhancement, a great deal of attention has been given to nanoarchitectures that generate maximum local field enhancement. In addition to high performance SERS active nanotextures, there are several other parameters that have direct influence on SERS enhancement. Two major efforts were made in our current studies. In chapters 3 and 4, AgPPF substrates acted as a pseudostationary phase and hence brings analytes close to silver nanoglobules. In chapter 5, nTP technique was employed to stamp out dimer nanostructures on various dielectric surfaces to monitor substrate effect on SERS.

Polypropylene filter is a dielectric material and can be used as a SERS substrate. On thermal evaporation of pure silver particles, microfibers produce sub 100 nm nanoglobules to serve as a SERS-active surface. On passing analytes through the filter substrate, molecules are trapped/adsorbed onto the silver and/or polypropylene surfaces based on their affinity to the specific surfaces. This simple and a cost-effective approach has shown great promises in SERS detection of possible endocrine disrupting chemicals, pharmaceuticals, personal care products, radionuclide, and several other organic dyes. Hyphenating concentration protocol with STT, it is possible to detect

range of compounds of environmental significance. Moreover, using AgPPF, the affinity of uranyl hydroxyl complexes to nanostructured silver surfaces was studied. Results support that the sorption of uranyl species to silver surfaces is a slow process. With this understanding, we have shown that, without any surface modification, SERS can be used to detect traces of uranium in an aqueous solution.

Since AgPPF substrate has shown significant promises in detecting range of rarely SERS studied compounds, future studies on filter based SERS substrates can be aimed on developing it as a SERS platform for the analysis of biomolecules.

On the other aspect, we borrowed a printing technique from microelectronics industry and used to stamp out metal nanofeatures on various surfaces. We have augmented the scope of EBL in SERS research by imprinting nanofeatures created on silicon stamp to glass, SU8, and PDMS surfaces. In addition to scaling-up the production of substrates, nTP is shown to be promising in achieving better SERS enhancement by selecting suitable underlying substrates. Moreover, the technique has shown significant promises in the development of SERS-active fiber optics, lab-on-chip, and other related plasmonic devices.

nTP related work is still in progress in our laboratory. More recently, we realized that by *in situ* plasma deposition of fluoropolymer on nanostructured relief pillars, the overall efficiency of printing technique can be improved significantly. In the current approach, octafluorocyclobutane (OFCB) gas is plasma polymerized in a chamber to grow thin film and subsequently used as a proficient nTP mediator. Plasma polymerized OFCB have numerous advantages: OFCB coated silicon stamps are robust and chemical resistant, hence can be re-used after simple cleaning step. Meantime, due to its low surface energy, it promotes easy release of any solid materials embedded on its surface. In situ OFCB deposition step is a fast process and can grow 10 nm thin film in less than 10 sec. The substrate material and stamp may not require any additional chemical modifications prior to nTP. It can create nanoparticles of approximately 50 nm width/diameter with interparticle resolution of sub 10 nm. Results accomplished using OFCB mediated nTP is briefly discussed in appendix 2.

Future studies involving nTP-SERS should be focused on rational design of single-molecule SERS active nanodisc arrays on dielectric surface. Moreover, the capability of current approach to routinely deliver just-touching nanoparticles should be implemented for in-depth plasmonic study of such nanostructures. More controlled experiment can be performed on nanogap plasmonic effect using elastomeric substrates. Plasmonic micro/nanofludics functional devices and SERS-active fiber optic sensor can be fully developed. In addition, the recent success of integrating connecting nanowire between two electrodes has shown significant promise towards the development of nanowire sensors.

Bibliography

Bibliography

[1] Krishnan, R. & Shankar, R. RAMAN Effect- History of the Discovery. *Journal of Raman Spectroscopy* **10**, 1–8 (1981).

[2] Raman, C. & Krishnan, K. A new type of secondary radiation. *Nature* **121**, 501–502 (1928).

[3] Skoog, D., Holler, F. & Nieman, T. (Thomson Learning, Inc., 1997), 5th edn.

[4] Le Ru, E. & Etchegoin, P. In *Principles of Surface-Enhanced Raman Spectroscopy and Related Plasmonic Effects* (Elsevier, 2009).

[5] Bowie, B., Chase, D. & Griffiths, P. Factors Affecting the Performance of Bench-Top Raman Spectrometers. Part I: Instrumental Effects. *Applied Spectroscopy* **54**, 164A–173A (2000).

[6] Pitt, G. *et al.* Engineering Aspects and Applications of the New Raman Instrumentation. *IEE Proceedings-Science Measurement and Technology* **152**, 241–318 (2005).

[7] Laplant, F. & Benamotz, D. Design and Construction of a Microscope-Based Raman System. *Review of Scientific Instruments* **66**, 3537–3544 (1995).

[8] Borman, S. Non-Linear Raman-Spectroscopy. *Analytical Chemistry* **54**, A021 (1982).

[9] Kneipp, K. *et al.* Single Molecule Detection using Surface-Enhanced Raman Scattering (SERS). *Physical Review Letters* **78**, 1667–1670 (1997).

[10] Fleischmann, M., Hendra, P. & Mcquilla, A. Raman Spectra of Pyridine Adsorbed at a Silver Electrode. *Chemical Physics Letters* **26**, 163–166 (1974).

[11] Jeanmaire, D. & Vanduyne, R. Surface Raman Spectroelectrochemistry.1. Heterocyclic, Aromatic, and Aliphatic-Amines Adsorbed on Anodized Silver Electrode. *Journal of Electroanalytical Chemistry* **84**, 1–20 (1977).

[12] Albrecht, M. & Creighton, J. Anomalously Intense Raman-Spectra of Pyridine at a Silver Electrode . *Journal of the Americal Chemical Society* **99**, 5215–5217 (1977).

[13] Campion, A. & Kambhampati, P. Surface-Enhanced Raman Scattering. *Chemical Society Reviews* **27**, 241–250 (1998).

[14] Schatz, G. C., Young, M. A. & Van Duyne, R. P. Electromagnetic mechanism of SERS. In *Surface-Enhanced Raman Scattering: Physics and Applications*, vol. 103 of *Topics in Applied Physics*, 19–45 (2006).

[15] Brockman, J., Nelson, B. & Corn, R. Surface Plasmon Resonance Imaging Measurements of Ultrathin Organic Films. *Annual Review of Physical Chemistry* **51**, 41–63 (2000).

[16] Knoll, W. Interfaces and Thin Films as Seen by Bound Electromagnetic Waves. *Annual Review of Physical Chemistry* **49**, 569–638 (1998).

[17] Kelly, K., Coronado, E., Zhao, L. & Schatz, G. The Optical Properties of Metal Nanoparticles: The Influence of Size, Shape, and Dielectric Environment. *Journal of Physical Chemistry B* **107**, 668–677 (2003).

[18] Haes, A. *et al.* Plasmonic Materials for Surface-Enhanced Sensing and Spectroscopy. *MRS Bulletin* **30**, 368–375 (2005).

[19] Aroca, R. In *Surface-Enhanced Vibrational Spectroscopy* (John Wiley & Sons, Chichester, 2006).

[20] Campion, A., Ivanecky, J., Child, C. & Foster, M. On the Mechanism of Chemical Enhancement in Surface-Enhanced Raman Scattering. *Journal of the American Chemical Society* **117**, 11807–11808 (1995).

[21] Kambhampati, P., Child, C., Foster, M. & Campion, A. On the Chemical Mechanism of Surface Enhanced Raman Scattering: Experiment and Theory. *Journal of Chemical Physics* **108**, 5013–5026 (1998).

[22] Kambhampati, P., Child, C. & Campion, A. On the Role of Charge-Transfer Resonances in the Chemical Mechanism of Surface-Enhanced Raman Scattering. *Journal of the Chemical Society-Faraday Transactions* **92**, 4775–4780 (1996).

[23] Child, C., Fieberg, J. & Campion, A. Surface Chemistry of Polyimide Formation on Cu(111). *Surface Science* **372**, L254–L260 (1997).

[24] Aroca, R., Clavijo, R., Halls, M. & Schlegel, H. Surface-Enhanced Raman Spectra of Phthalimide. Interpretation of the SERS Spectra of the Surface Complex Formed on Silver Islands and Colloids. *Journal of Physical Chemistry A* **104**, 9500–9505 (2000).

[25] Lombardi, J., Birke, R., Lu, T. & Xu, J. Charge-Transfer Theory of Surface Enhanced Raman Spectroscopy; Herzberg-Teller Contributions. *Journal of Chemical Physics* **84**, 4174–4180 (1986).

[26] Cai, W. *et al.* Investigation of Surface-Enhanced Raman Scattering from Platinum Electrodes using a Confocal Raman Microscope: Dependence of Surface Roughening Pretreatment. *Surface Science* **406**, 9–22 (1998).

[27] Xie, Y. *et al.* Adsorption and Photon-Driven Charge Transfer of Pyridine on a Cobalt Electrode Analyzed by Surface Enhanced Raman Spectroscopy and Relevant Theories. *Journal of Electroanalytical Chemistry* **554**, 417–425 (2003).

[28] Haynes, C. & Van Duyne, R. Plasmon-Sampled Surface-Enhanced Raman Excitation Spectroscopy. *Journal of Physical Chemistry B* **107**, 7426–7433 (2003).

[29] Bhandari, D., Wells, S. M., Retterer, S. T. & Sepaniak, M. J. Characterization and Detection of Uranyl Ion Sorption on Silver Surfaces Using Surface Enhanced Raman Spectroscopy. *Analytical Chemistry* **81**, 8061–8067 (2009).

[30] Oran, J., Hinde, R., Abu Hatab, N., Retterer, S. & Sepaniak, M. Nanofabricated Periodic Arrays of Silver Elliptical Discs as SERS Substrates. *Journal of Raman Spectroscopy* **39**, 1811–1820 (2008).

[31] Sylvia, J., Janni, J., Klein, J. & Spencer, K. Surface-Enhanced Raman Detection of 1,4-Dinitro Toluene Impurity Vapor as a Marker to Locate Landmines. *Analytical Chemistry* **72**, 5834–5840 (2000).

[32] Cinta-Pinzaru, S. *et al.* FT-Raman and NIR-SERS Characterization of the Antimalarial Drugs Chloroquine and Mefloquine and their Interaction with Hematin. *Journal of Raman Spectroscopy* **37**, 326–334 (2006).

[33] Binoy, J., Joe, I., Jayakumar, V., Nielsen, O. & Aubard, J. DFT Based Relaxed PES Scan Studies and SERS of Anti Cancer Drug, Combretastatin A-4. *Laser Physics Letters* **2**, 544–550 (2005).

[34] Szeghalmi, A. *et al.* Adsorption of 6-Mercaptopurine and 6-Mercaptopurine Riboside on Silver Colloid: a pH Dependent Surface Enhanced Raman Spectroscopy and Density Functional Theory Study. Part I. 6-Mercaptopurine. *Journal of molecular structures* **735**, 103–113 (2005).

[35] Szeghalmi, A. *et al.* Adsorption of 6-Mercaptopurine and 6-Mercaptopurine-Riboside on Silver Colloid: A pH-Dependent Surface-Enhanced Raman Spectroscopy and Density Functional Theory Study. II. 6-Mercaptopurine-Riboside. *Biopolymers* **78**, 298–310 (2005).

[36] Alvarez-Puebla, R. A., dos Santos, D. S., Jr. & Aroca, R. F. SERS Detection of Environmental Pollutants in Humic Acid-Gold Nanoparticle Composite Materials. *Analyst* **132**, 1210–1214 (2007).

[37] Camden, J. P., Dieringer, J. A., Zhao, J. & Van Duyne, R. P. Controlled Plasmonic Nanostructures for Surface-Enhanced Spectroscopy and Sensing. *Accounts of Chemical Research* **41**, 1653–1661 (2008).

[38] Yonzon, C. R., Lyandres, O., Shah, N. C., Dieringer, J. A. & Van Duyne, R. P. Glucose Sensing with Surface-Enhanced Raman Spectroscopy. In *Surface-Enhanced Raman Scattering: Physics and Applications*, vol. 103 of *Topics in Applied Physics*, 367–379 (2006).

[39] Lyandres, O. *et al.* Real-Time Glucose Sensing by Surface-enhanced Raman Spectroscopy in Bovine Plasma Facilitated by a Mixed Decanethiol/Mercaptohexanol Partition Layer. *Analytical Chemistry* **77**, 6134–6139 (2005).

[40] Leona, M. Microanalysis of Organic Pigments and Glazes in Polychrome Works of Art by surface-enhanced Resonance Raman Scattering. *Proceeding of the National Academy of Sciences of the United States of America* **106**, 14757–14762 (2009).

[41] Lau, D., Livett, M. & Prawer, S. Application of Surface-Enhanced Raman Spectroscopy (SERS) to the Analysis of Natural Resins in Artworks. *Journal of Raman Spectroscopy* **39**, 545–552 (2008).

[42] Chen, K., Leona, M. & Vo-Dinh, T. Surface-enhanced Raman Scattering for Identification of Organic Pigments and Dyes in Works of Art and Cultural Heritage Material. *Sensor Review* **27**, 109–120 (2007).

[43] Feng, S. *et al.* Gold Nanoparticle Based Surface-Enhanced Raman Scattering Spectroscopy of Cancerous and Normal Nasopharyngeal Tissues Under Near-Infrared Laser Excitation. *Applied Spectroscopy* **63**, 1089–1094 (2009).

[44] Han, X. X., Zhao, B. & Ozaki, Y. Surface-enhanced Raman Scattering for Protein Detection. *Analytical and Bioanalytical Chemistry* **394**, 1719–1727 (2009).

[45] Han, X. X., Huang, G. G., Zhao, B. & Ozaki, Y. Label-Free Highly Sensitive Detection of Proteins in Aqueous Solutions Using Surface-Enhanced Raman Scattering. *Analytical Chemistry* **81**, 3329–3333 (2009).

[46] Chowdhury, M. H., Ray, K., Gray, S. K., Pond, J. & Lakowicz, J. R. Aluminum Nanoparticles as Substrates for Metal-Enhanced Fluorescence in the Ultraviolet for the Label-Free Detection of Biomolecules. *Analytical Chemistry* **81**, 1397–1403 (2009).

[47] Vanduyne, R., Hulteen, J. & Treichel, D. Atomic-Force Microscopy and Surface-Enhanced Raman Spectroscopy .1. Ag Island Films and Ag Film over Polymer Nanosphere Surfaces Supported on Glass. *Journal of Chemical Physics* **99**, 2101–2115 (1993).

[48] Giesfeldt, K. *et al.* Studies of the Optical Properties of Metal-pliable Polymer Composite Materials. *Applied Spectroscopy* **57**, 1346–1352 (2003).

[49] Giesfeldt, K., Connatser, R., De Jesus, M., Dutta, P. & Sepaniak, M. Gold-Polymer Nanocomposites: Studies of their Optical Properties and their Potential as SERS Substrates. *Journal of Raman Spectroscopy* **36**, 1134–1142 (2005).

[50] Freunscht, P., Van Duyne, R. & Schneider, S. Surface-enhanced Raman Spectroscopy of Trans-stilbene Adsorbed on Platinum- or Self-Assembled Monolayer-modified Silver Film over Nanosphere Surfaces. *Chemical Physics Letters* **281**, 372–378 (1997).

[51] Dick, L., McFarland, A., Haynes, C. & Van Duyne, R. Metal Film over Nanosphere (MFON) Electrodes for Surface-Enhanced Raman Spectroscopy (SERS): Improvements in Surface Nanostructure Stability and Suppression of Irreversible loss. *Journal of Physical Chemistry B* **106**, 853–860 (2002).

[52] Nie, S. & Emery, S. Probing Single Molecules and Single Nanoparticles by Surface-Enhanced Raman Scattering. *Science* **275**, 1102–1106 (1997).

[53] Aroca, R., Alvarez-Puebla, R., Pieczonka, N., Sanchez-Cortez, S. & Garcia-Ramos, J. Surface-enhanced Raman Scattering on Colloidal Nanostructures. *Advances in Colloid and Interface Science* **116**, 45–61 (2005).

[54] Michaels, A., Nirmal, M. & LE, B. Surface-enhanced Raman Spectroscopy of Individual Rhodamine 6G Molecules on Large Ag Nanocrystals. *Journal of American Chemical Society* 45–61 (1999).

[55] Weiss, A. & Haran, G. Time Dependent Single-molecule Raman Scattering as a Probe of Surface Dynamics. *Journal of Physical Chemistry B* **105**, 12348–12354 (2001).

[56] Etchegoin, P. *et al.* New Limits in Ultrasensitive Trace Detection by Surface Enhanced Raman Scattering (SERS). *Chemical Physics Letters* **375**, 84–90 (2003).

[57] Khan, I., Cunningham, D., Graham, D., McComb, D. & Smith, W. Identification and Characterization of Active and Inactive Species for Surface-Enhanced Resonance Raman Scattering. *Journal of Physical Chemistry B* **109**, 3454–3459 (2005).

[58] Dieringer, J. A., Lettan, R. B., II, Scheidt, K. A. & Van Duyne, R. P. A frequency domain existence proof of single-molecule surface-enhanced Raman Spectroscopy. *Journal of the American Chemical Society* **129**, 16249–16256 (2007).

[59] Hulteen, J. & Vanduyne, R. Nanosphere lithography - A Materials General Fabrication Process For Periodic Particle Array Surfaces. *Journal of Vacuum Science & Technology A-Vacuum Surfaces and Films* **13**, 1553–1558 (1995).

[60] Hulteen, J. *et al.* Nanosphere Lithography: Size-Tunable Silver Nanoparticle and Surface Cluster Arrays. *Journal of Physical Chemistry B* **103**, 3854–3863 (1999).

[61] Micheletto, R., Fukuda, H. & Ohtsu, M. A Simple Method for the Production of a 2-Dimensional, Ordered array of small Latex-Particles. *Langmuir* **11**, 3333–3336 (1995).

[62] Dieringer, J. *et al.* Surface Enhanced Raman Spectroscopy: New Materials, Concepts, Characterization Tools, and Applications. *Faraday Discussions* **132**, 9–26 (2006).

[63] Wang, H. *et al.* Low temperature ZEP-520A Development Process for Enhanced Critical Dimension Realization in Reactive Ion Etched Polysilicon. *Journal of Vacuum Science & Technology B* **25**, 102–105 (2007).

[64] Zhou, Z. In Yao, N and Wang ZL (ed.) *Handbook of Microscopy for Nanotechnology*, vol. I (Springer, 2005).

[65] Loo, Y., Willett, R., Baldwin, K. & Rogers, J. Interfacial Chemistries for Nanoscale Transfer Printing. *Journal of the American Chemical Society* **124**, 7654–7655 (2002).

[66] Loo, Y., Willett, R., Baldwin, K. & Rogers, J. Additive, Nanoscale Patterning of Metal Films with a Stamp and a Surface Chemistry Mediated Transfer Process: Applications in Plastic Electronics. *Applied Physics Letters* **81**, 562–564 (2002).

[67] Menard, E. & Rogers, J. A. In *Springer Handbook of Nanotechnology*, 313–332 (Springer, 2010), 3rd edn.

[68] Focazio, M. J. *et al.* A National Reconnaissance for Pharmaceuticals and other Organic Wastewater Contaminants in the United States - II) Untreated Drinking Water Sources. *Science of the Total Environment* **402**, 201–216 (2008).

[69] McLachlan, J. Environmental Signaling: What Embryos and Evolution Teach us about Endocrine Disrupting Chemicals. *Endocrine Reviews* **22**, 319–341 (2001).

[70] Panter, G., Thompson, R. & Sumpter, J. Intermittent Exposure of Fish to Estradiol. *ENVIRONMENTAL SCIENCE & TECHNOLOGY* **34**, 2756–2760 (2000).

[71] White, R., Jobling, S., Hoare, S., Sumpter, J. & Parker, M. Environmentally Persistent Alkylphenolic Compounds are Estrogenic. *Endocrinology* **135**, 175–182 (1994).

[72] Davis, D. & Bradlow, H. Can Environmental Estrogens Cause Breast-Cancer. *Scientific American* **273**, 166–& (1995).

[73] Gilliver, M., Bennett, M., Begon, M., Hazel, S. & Hart, C. Enterobacteria - Antibiotic Resistance found in Wild Rodents. *Nature* **401**, 233–234 (1999).

[74] Collins-Burow, B., Burow, M., Duong, B. & McLachlan, J. Estrogenic and Antiestrogenic Activities of Flavonoid Phytochemicals through Estrogen Receptor Binding-Dependent and -Independent Mechanisms. *Nutrition and Cancer-An International Journal* **38**, 229–244 (2000).

[75] Wood, S. L., Jarrell, J. J., Swaby, C. & Chan, S. Endocrine disruptors and spontaneous premature labor: a case control study. *Environmental Health* **6** (2007).

[76] Curnow, D. Oestrogenic Activity of Subterranean Clover.2. The Isolation of Genistein from Subterranean Clover and Methods of Quantitative Estimation. *Biochemical Journal* **58**, 283–287 (1954).

[77] Setchell, K. *et al.* Dietary Estrogens - A Probable Cause of Infertility and Liver-Disease in Captive Cheetahs. *Gastroenterology* **93**, 225–233 (1987).

[78] Fox, J., Starcevic, M., Kow, K., Burow, M. & McLachlan, J. Nitrogen Fixation - Endocrine Disrupters and Flavonoid Signalling. *Nature* **413**, 128–129 (2001).

[79] Sedlak, D., Gray, J. & Pinkston, K. Contaminants in Recycled Water. *Environmental Science & Technology* **34**, 509A–515A (2000).

[80] Spencer, K., Sylvia, J., Clauson, S., Bertone, J. & Christesen, S. *Proc. SPIE-Int. Soc. Opt. Eng.* **340**, 5268 (2004).

[81] De Jesus, M., Giesfeldt, K. & Sepaniak, M. Improving the Analytical Figures of Merit of SERS for the Analysis of Model Environmental Pollutants. *Journal of Raman Spectroscopy* **35**, 895–904 (2004).

[82] Spencer, K., Sylvia, J., Clauson, S., Bertone, J. & Christesen, S. *Proc. SPIE-Int. Soc. Opt. Eng.* **340**, 5269 (2004).

[83] Alvarez-Ros, M., Sanchez-Cortes, S., Francioso, O. & Garcia-Ramos, J. Adsorption and Chemical Modification of Gallic Acid on Silver Nanoparticles Studied by Raman Spectroscopy: Effect of Anions and Cationic Pesticide Paraquat. *Canadian Journal of Analytical Sciences and Spectroscopy* **48**, 132–138 (2003).

[84] Peica, N., Lehene, C., Leopold, N., Cozar, O. & Kiefer, W. Raman and Surface-Enhanced Raman Studies of the Food Additive Sodium Benzoate. *Journal of Optoelectronics and Advanced Materials* **9**, 2943–2948 (2007).

[85] Peica, N., Pavel, I., Pinzaru, S., Rastogi, V. & Kiefer, W. Vibrational Characterization of E102 Food Additive by Raman and Surface-Enhanced Raman Spectroscopy and Theoretical Studies. *Journal of Raman Spectroscopy* **36**, 657–666 (2005).

[86] Driskell, J. D. *et al.* Infectious Agent Detection with SERS-Active Silver Nanorod Arrays Prepared by Oblique Angle Deposition. *IEEE Sensors Journal* **8**, 863–870 (2008).

[87] Shanmukh, S. *et al.* Rapid and Sensitive Detection of Respiratory Virus Molecular Signatures using a Silver Nanorod Array SERS Substrate. *Nano Letters* **6**, 2630–2636 (2006).

[88] Farquharson, S. *et al.* Detecting Bacillus Cereus Spores on a Mail Sorting System Using Raman Spectroscopy. *Journal of Raman Spectroscopy* **35**, 82–86 (2004).

[89] Kneipp, K. *et al.* Near-Infrared Surface-Enhanced Raman Scattering can Detect Single Molecules and Observe 'Hot' Vibrational Transitions. *Journal of Raman Spectroscopy* **29**, 743–747 (1998).

[90] Kneipp, K. *et al.* Surface-enhanced Raman Scattering (SERS) - A New Tool for Single Molecule Detection and Identification. *Bioimaging* **6**, 104–110 (1998).

[91] Kneipp, K. *et al.* Detection and Identification of a Single DNA Base Molecule Using Surface-Enhanced Raman Scattering (SERS). *Physical Review E* **57**, R6281–R6284 (1998).

[92] Kneipp, K. *et al.* Single-Molecule Detection of a Cyanine Dye in Silver Colloidal Solution Using Near-Infrared Surface-Enhanced Raman Scattering. *Applied Spectroscopy* **52**, 175–178 (1998).

[93] Vo-Dinh, T. Surface-Enhanced Raman Spectroscopy Using Metallic Nanostructures. *Trac-Trends in Analytical Chemistry* **17**, 557–582 (1998).

[94] Rivas, L., Sanchez-Cortes, S., Garcia-Ramos, J. & Morcillo, G. Growth of Silver Colloidal Particles Obtained by Citrate Reduction to Increase the Raman Enhancement Factor. *Langmuir* **17**, 574–577 (2001).

[95] Jensen, T., Malinsky, M., Haynes, C. & Van Duyne, R. Nanosphere Lithography: Tunable Localized Surface Plasmon Resonance Spectra of Silver Nanoparticles. *Journal of Physical Chemistry B* **104**, 10549–10556 (2000).

[96] Abu Hatab, N. A., Oran, J. M. & Sepaniak, M. J. Surface-enhanced Raman Spectroscopy Substrates Created via Electron Beam Lithography and Nanotransfer Printing. *ACS Nano* **2**, 377–385 (2008).

[97] Teslova, T. *et al.* Raman and Surface-Enhanced Raman Spectra of Flavone and Several Hydroxy Derivatives. *Journal of Raman Spectroscopy* **38**, 802–818 (2007).

[98] Szabo, N. & Winefordner, J. Evaluation of a Solid-Phase Extraction Membrane as a Surface-Enhanced Raman Substrate. *Applied Spectroscopy* **52**, 500–512 (1998).

[99] Walsh, R. & Chumanov, G. Silver Coated Porous Alumina as a New Substrate for Surface-Enhanced Raman Scattering. *Applied Spectroscopy* **55**, 1695–1700 (2001).

[100] De Jesus, M., Giesfeldt, K. & Sepaniak, M. Use of a Sample Translation Technique to Minimize Adverse Effects of Laser Irradiation in Surface-Enhanced Raman Spectroscopy. *Applied Spectroscopy* **57**, 428–438 (2003).

[101] Kiefer, W. & Bernstei, H. Rotating Raman Sample Technique for Colored Crystal Powders - Resonance Raman Effect in Solid KMN04. *Applied Spectroscopy* **25**, 609–& (1971).

[102] Horimoto, N., Ishikawa, N. & Nakajima, A. Preparation of a SERS Substrate Using Vacuum-Synthesized Silver Nanoparticles. *Chemical Physics Letters* **413**, 78–83 (2005).

[103] Jurasekova, Z., Domingo, C., Garcia-Ramos, J. V. & Sanchez-Cortes, S. In situ Detection of Flavonoids in Weld-Dyed Wool and Silk Textiles by Surface-Enhanced Raman Scattering. *Journal of Raman Spectroscopy* **39**, 1309–1312 (2008).

[104] Jurasekova, Z., Garcia-Ramos, J. V., Domingo, C. & Sanchez-Cortes, S. Surface-Enhanced Raman Scattering of Flavonoids. *Journal of Raman Spectroscopy* **37**, 1239–1241 (2006).

[105] `http://solutions.3m.com/wps/portal/3M/enUS/Empore/extraction/center/technical-library/cartridge-faq/`.

[106] Morrison, S., Tripathi, V. & Spangler, R. Coupled Reaction Transport Modeling of a Chemical Barrier for Controlling Uranium(VI) Contamination in Groundwater. *Journal of Contaminant Hydrology* **17**, 347–363 (1995).

[107] Palmer, D. & NguyenTrung, C. Aqueous Uranyl Complexes .3. Potentiometric Measurements of the Hydrolysis of Uranyl(VI) Ion at 25 degrees C. *Journal of Solution Chemistry* **24**, 1281–1291 (1995).

[108] Eliet, V., Bidoglio, G., Omenetto, N., Parma, L. & Grenthe, I. Characterization of Hydroxide Complexes of Uranium(VI) by Time-Resolved Fluorescence Spectroscopy. *Journal of the Chemical Society-Faraday Transactions* **91**, 2275–2285 (1995).

[109] Clark, D. *et al.* Chemical Speciation of the Uranyl Ion Under Highly Alkaline Conditions. Synthesis, Structures, and Oxo Ligand Exchange Dynamics. *Inorganic Chemistry* **38**, 1456–1466 (1999).

[110] Nguyen-Trung, C., , D., Begun, G., Peiffert, C. & Mesmer, R. Aqueous Uranyl Complexes 1. Raman Spectroscopic Study of the Hydrolysis of Uranyl(VI) in Solutions of Trifluoromethanesulfonic Acid and/or Tetramethylammonium Hydroxide at 25 degrees C and 0.1 MPa. *Journal of Solution Chemistry* **29**, 101–129 (2000).

[111] Toth, L. & Begun, G. Raman-Spectra of Uranyl-Ion and its Hydrolysis Products in Aqueous HNO3. *Journal of Physical Chemistry* **85**, 547–549 (1981).

[112] Katz, J., Seaborg, G. & Morss, L. In *The Chemistry of the Atinide Elements* (Chapman and Hall: London, 1986).

[113] Rodriguez, A., Lopez, B., Fucugauchi, L. & Martinezquiroz, E. Preparation of Ammonium Uranate in the Recovery Treatment of Non-Fissioned Uranium. *Journal of Radioanalytical and Nuclear Chemistry- Articles* **177**, 279–290 (1994).

[114] Leverette, C. L. *et al.* Trace Detection and Differentiation of Uranyl(VI) Ion Cast Films Utilizing Aligned Ag Nanorod SERS Substrates. *Vibrational Spectroscopy* **50**, 143–151 (2009).

[115] Tsushima, S., Nagasaki, S., Tanaka, S. & Suzuki, A. A Raman Spectroscopic Study of Uranyl Species Adsorbed onto Colloidal Particles. *Journal of Physical Chemistry B* **102**, 9029–9032 (1998).

[116] Maya, L. Sorbed Uranium (VI) Species on Hydrous Titania, Zirconia, and Silica-gel. *Radiochimica acta* **31**, 147–151 (1982).

[117] Maya, L. & Begun, G. A Raman-Spectroscopy Study of Hydroxo and Carbonato Species of the Uranyl (VI)Ion. *Journal of Inorganic & Nuclear Chemistry* **43**, 2827–2832 (1981).

[118] Lefevre, G., Kneppers, J. & Fedoroff, M. Sorption of Uranyl Ions on Titanium Oxide Studied by ATR-IR Spectroscopy. *Journal of Colloid and Interface Science* **327**, 15–20 (2008).

[119] Ortiz-Oliveros, H. B., Ordonez-Regil, E. & Fernandez-Valverde, S. M. Sorption of Uranium(VI) onto Strontium Titanate in KNO3 Medium. *Journal of Radioanalytical and Nuclear Chemistry* **279**, 601–610 (2009).

[120] Perron, H. *et al.* Theoretical Investigation of the Uranyl Ion Sorption on the Rutile TiO2(110) Face. *Inorganic Chemistry* **47**, 10991–10997 (2008).

[121] Vandenborre, J., Drot, R. & Simoni, E. Interaction Mechanisms Between Uranium(VI) and Rutile Titanium dioxide: From Single Crystal to Powder. *Inorganic Chemistry* **46**, 1291–1296 (2007).

[122] Dai, S., Lee, Y. & Young, J. Observation of the Surface-enhanced Raman Scattering Spectrum of Uranyl Ion. *Applied Spectroscopy* **50**, 536–537 (1996).

[123] Bao, L., Mahurin, S., Haire, R. & Dai, S. Silver-doped Sol-gel Film as a Surface-enhanced Raman Scattering Substrate for Detection of Uranyl and Neptunyl Ions. *Analytical Chemistry* **75**, 6614–6620 (2003).

[124] Burneau, A. & Teiten, B. Surface-enhanced Raman spectra of both uranyl(VI) and 2-(5-bromo-2-pyridylazo)-5-diethylaminophenol in silver colloids. *Vibrational Spectroscopy* **21**, 97–109 (1999).

[125] Clavijo, R. *et al.* Raman-Spectra of Thin Solid Films .7. Uranyl Superphthalocyanine. *Journal of Raman Spectroscopy* **20**, 461–465 (1989).

[126] Ruan, C., Luo, W., Wang, W. & Gu, B. Surface-enhanced Raman spectroscopy for uranium detection and analysis in environmental samples. *Analytica Chimica Acta* **605**, 80–86 (2007).

[127] Teiten, B. & Burneau, A. Detection and sorption study of dioxouranium(VI) ions on N-(2-mercaptopropionyl)glycine-modified silver colloid by surface-enhanced Raman scattering. *Journal of Raman Spectroscopy* **28**, 879–884 (1997).

[128] Bhandari, D., Walworth, M. J. & Sepaniak, M. J. Dual Function Surface-Enhanced Raman Active Extractor for the Detection of Environmental Contaminants. *Applied Spectroscopy* **63**, 571–578 (2009).

[129] Palacios, M. & Taylor, S. Characterization of uranium oxides using in situ micro-Raman spectroscopy. *Applied Spectroscopy* **54**, 1372–1378 (2000).

[130] Waterhouse, G., Bowmaker, G. & Metson, J. The thermal decomposition of silver (I, III) oxide: A combined XRD, FT-IR and Raman spectroscopic study. *Physical Chemistry Chemical Physics* **3**, 3838–3845 (2001).

[131] Zanonato, P. *et al.* Hydrolysis of uranium(VI) at variable temperatures (10-85 degrees C). *Journal of the American Chemical Society* **126**, 5515–5522 (2004).

[132] Roof, R., Cromer, D. & Larson, A. In *Technical Report LADC-5718* (Los Alamos National Laboratory, Los Alamos, NM, 1962).

[133] Toth, L., Friedman, H., Begun, G. & Dorris, S. Raman Study of Uranyl-ion Attachment to Thorium (IV) Hydrous Polymer. *Journal of Physical Chemistry* **88**, 5574–5577 (1984).

[134] Ohwada, K. Uranium-Oxygen Lattice Vibrations of Lithium, Beta-Sodium, and Beta-Strontium Uranates. *Journal of Inorganic & Nuclear Chemistry* **32**, 1209–& (1970).

[135] Davies, R., Kennedy, J., Peckett, J., Robinson, B. & Steeton, R. In *Report AERE-R 5024*.

[136] McGlynn, S., Neely, W. & Smith, J. Electronic Structure, Spectra, and Magnetic Properties of Oxycations.3. Ligation Effects on Infrared Spectrum of Uranyl Ion. *Journal of Chemical Physics* **35**, 105–& (1961).

[137] Long, G. & Winefordner, J. Limit of Detection. *Analytical Chemistry* **55**, A712–& (1983).

[138] Kneipp, J., Kneipp, H. & Kneipp, K. SERS - a single-molecule and nanoscale tool for bioanalytics. *Chemical Society Reviews* **37**, 1052–1060 (2008).

[139] Moskovits, M. Surface-enhanced Raman spectroscopy: a brief perspective. In *Surface-Enhanced Raman Scattering: Physics and Applications*, vol. 103 of *Topics in Applied Physics*, 1–17 (2006).

[140] Gui, J. *et al.* Adsorption and Surface Structureal Chemistry of Thiophenol, Benzyl mercaptan, and Alkyl mercaptans - Comparative Studies at Ag (111) and Pt (111) Electrodes by Means of Auger-Spectroscopy, Electron-energy Loss Spectroscopy, Low-energy Electron Diffraction, and Electrochemistry. *Langmuir* **7**, 955–963 (1991).

[141] Wells, S. M., Retterer, S. D., Oran, J. M. & Sepaniak, M. J. Controllable Nanofabrication of Aggregate-like Nanoparticle Substrates and Evaluation for Surface-Enhanced Raman Spectroscopy. *ACS Nano* **3**, 3845–3853 (2009).

[142] Chou, S., Krauss, P. & Renstrom, P. Nanoimprint Lithography. *Journal of Vacuum Science & Technology B* **14**, 4129–4133 (1996).

[143] Chou, S., Krauss, P., Zhang, W., Guo, L. & Zhuang, L. Sub-10 nm imprint lithography and applications. *Journal of Vacuum Science & Technology B* **15**, 2897–2904 (1997).

[144] Xia, Y. & Whitesides, G. Soft Lithography. *Annual Review of Materials Science* **28**, 153–184 (1998).

[145] Xia, Y. & Whitesides, G. Soft Lithography. *Angewandte Chemie-International Edition* **37**, 551–575 (1998).

[146] Aizenberg, J., Rogers, J., Paul, K. & Whitesides, G. Imaging Profiles of Light Intensity in the Near Field: Applications to Phase-Shift Photolithography. *Applied Optics* **37**, 2145–2152 (1998).

[147] Smith, H., Efremow, N. & Kelley, P. Photolithographic Contact Printing of 4000A Linewidth Patterns. *Journal of Electrochemical Society* **121**, 1503–1506 (1974).

[148] Creighton, J., Blatchford, C. & Albrecht, M. Plasma Resonance Enhancement of Raman-Scattering by Pyridine Adsorbed on Silver or Gold Sol Particles of Size Comparable to the Excitation Wavelength. *Journal of the Chemical Society-Faraday Transactions II* **75**, 790–798 (1979).

[149] Moskovits, M. Surface-Roughness and Enhanced Intensity of Raman-Scattering by Molecules Adsorbed on Metals. *Journal of Chemical Physics* **69**, 4159–4161 (1978).

[150] Kinnan, M. K., Kachan, S., Simmons, C. K. & Chumanov, G. Plasmon Coupling in Two-Dimensional Arrays of Silver Nanoparticles: I. Effect of the Dielectric Medium. *Journal of physical chemistry C* **113**, 7079–7084 (2009).

[151] Malinsky, M., Kelly, K., Schatz, G. & Van Duyne, R. Nanosphere lithography: Effect of substrate on the localized surface plasmon resonance spectrum of silver nanoparticles. *Journal of physical chemistry B* **105**, 2343–2350 (2001).

[152] Novo, C., Funston, A. M., Pastoriza-Santos, I., Liz-Marzan, L. M. & Mulvaney, P. Influence of the Medium Refractive Index on the Optical Properties of Single

Gold Triangular Prisms on a Substrate. *Journal of Physical Chemistry C* **112**, 3–7 (2008).

[153] Sherry, L. J., Jin, R., Mirkin, C. A., Schatz, G. C. & Van Duyne, R. P. Localized surface plasmon resonance spectroscopy of single silver triangular nanoprisms. *Nano letters* **6**, 2060–2065 (2006).

[154] De Jesus, M. *et al.* Nanofabrication of Densely Packed Metal-Polymer Arrays for Surface-Enhanced Raman spectroscopy. *Applied Spectroscopy* **59**, 1501–1508 (2005).

[155] Felidj, N. *et al.* Controlling the optical response of regular arrays of gold particles for surface-enhanced Raman scattering. *Physical Review B* **65** (2002).

[156] Gunnarsson, L. *et al.* Interparticle Coupling Effects in Nanofabricated Substrates for Surface-Enhanced Raman Scattering. *Applied Physics Letters* **78**, 802–804 (2001).

[157] Hunyadi, S. E. & Murphy, C. J. Bimetallic Silver-Gold Nanowires: Fabrication and Use in Surface-Enhanced Raman Scattering. *Journal of Materials Chemistry* **16**, 3929–3935 (2006).

[158] Sun, Y. & Xia, Y. Shape-Controlled Synthesis of Gold and Silver Nanoparticles. *SCIENCE* **298**, 2176–2179 (2002).

[159] `www.cst.com`.

[160] Weiland, T. Discretization Method for Solution of Maxwell's Equations for 6-component Fields . *AEU-International Journal of Electronics and Communications* **31**, 116–120 (1977).

[161] Palik, E. In *Handbook of Optical Constants of Solids* (Academic Press, Orlando, 1985), 1st edn.

[162] Hu, M., Noda, S., Okubo, T., Yamaguchi, Y. & Komiyama, H. Structure and Morphology of Self-Assembled 3-mercaptopropyltrimethoxysilane Layers on Silicon Oxide. *Applied Surface Science* **181**, 307–316 (2001).

[163] Wellman, A. D. & Sepaniak, M. J. Multiplexed, waveguide approach to magnetically assisted transport evanescent field fluoroassays. *Analytical Chemistry* **79**, 6622–6628 (2007).

[164] Chah, S., Hutter, E., Roy, D., Fendler, J. & Yi, J. The effect of substrate metal on 2-aminoethanethiol and nanoparticle enhanced surface plasmon resonance imaging. *Chemical Physics* **272**, 127–136 (2001).

[165] Ong, B. H., Yuan, X. & Tjin, S. C. Adjustable Refractive Index Modulation for a Waveguide with SU-8 Photoresist by Dual-UV Exposure Lithography. *Applied Optics* **45**, 8036–8039 (2006).

[166] Gopinath, A. *et al.* Plasmonic Nanogalaxies: Multiscale Aperiodic Arrays for Surface-Enhanced Raman Sensing. *Nano Letters* **9**, 3922–3929 (2009).

[167] Connatser, R., Riddle, L. & Sepaniak, M. Metal-polymer nanocomposites for integrated microfluidic separations and surface enhanced Raman spectroscopic detection. *Journal of Separation Science* **27**, 1545–1550 (2004).

[168] Hao, E. & Schatz, G. Electromagnetic Fields Around Silver Nanoparticles and Dimers. *Journal of Chemical Physics* **120**, 357–366 (2004).

[169] Hinde, R., Sepaniak, M., Compton, R., Nordling, J. & Lavrik, N. Surface-Enhanced Resonance Raman Scattering of Adsorbates under Liquid Nitrogen. *Chemical Physics Letters* **339**, 167–173 (2001).

[170] Qin, L. *et al.* Designing, fabricating, and imaging Raman hot spots. *Proceedings of the National Academy of Scineces of the United States of America* **103**, 13300–13303 (2006).

[171] Ward, D. R. *et al.* Electromigrated nanoscale gaps for surface-enhanced Raman spectroscopy. *Nano Letters* **7**, 1396–1400 (2007).

[172] Xu, H., Bjerneld, E., Kall, M. & Borjesson, L. Spectroscopy of single hemoglobin molecules by surface enhanced Raman scattering. *Physical Review Letters* **83**, 4357–4360 (1999).

[173] Dhawan, A. *et al.* Focused in beam fabrication of metallic nanostructures on end faces of optical fibers for chemical sensing applications. *Journal of Vacuum Science & Technology B* **26**, 2168–2173 (2008).

[174] Smythe, E. J., Dickey, M. D., Bao, J., Whitesides, G. M. & Capasso, F. Optical Antenna Arrays on a Fiber Facet for in Situ Surface-Enhanced Raman Scattering Detection. *Nano Letters* **9**, 1132–1138 (2009).

Appendix

Appendix A

Supporting Information: Stamping High-Aspect-Ratio Plasmonic Nanoarrays on SERS-Supporting Platforms

A.1 Functionalization of substrates

Substrates were silanized in a 5 mM (3-mercaptopropyl)-trimethoxysilane (3MPTMS) solution. 3MPTMS and surface hydroxyl groups on the substrate facilitate co-condensation of the methoxy group. Figure A.1. shows the surface chemistries between a hydroxyl group and 3MPTMS that promotes adhesion between substrate and transferred metallic array.

A.2 In-house built pressure monitoring device and nanotransfer printing

In our study, we observed that the transfer pressure and contact time between stamp and substrate was important for imprinting defect free nanoantenna arrays. Contact pressure was monitored by in-house built pneumatic device. Schematic of the device is shown in Figure A.2.

Shown in Figures A.3a and A.3b are representative non-optimal conditions transfer printed bowtie arrays.

A.3 Nanotransfer printing protocol on fiber optic facet

Shown in Figure A.4 is a visual depiction of the protocol developed to nanotransfer print arrays of metallic nanostructures on a fiber optic facet.

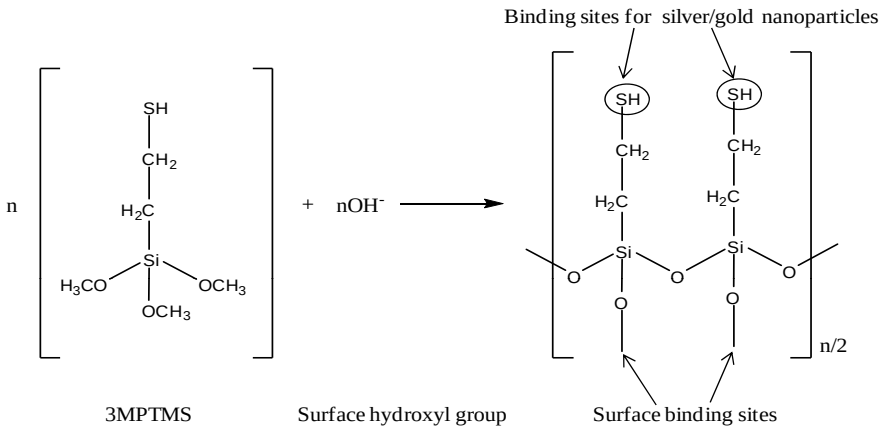


Figure A.1: Surface Chemistries between surface hydroxyl and 3MPTMS

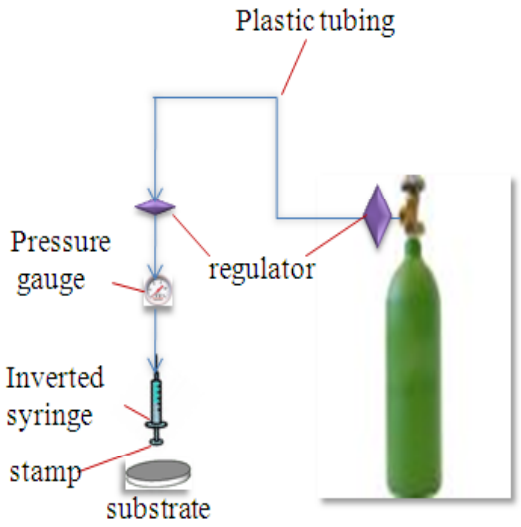


Figure A.2: Schematic depiction of an in-house built pressure device

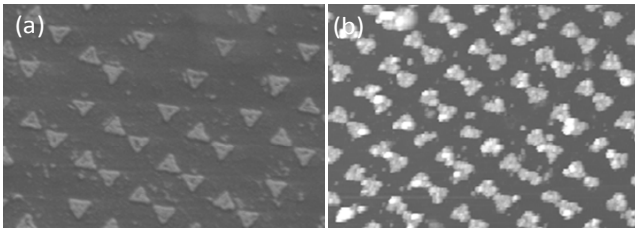


Figure A.3: Micrographs (AFM, b, SEM, a) representing non-optimal conditions imprinting on (a) PDMS elastomer and (b) SU-8 resist.

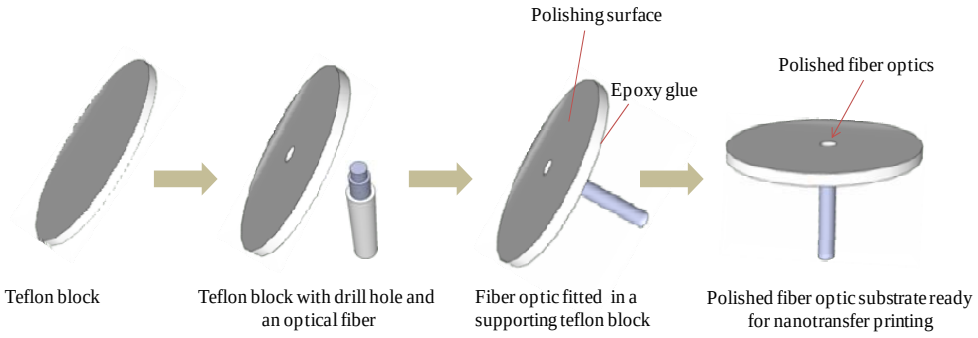


Figure A.4: Schematic depiction of the procedure for transfer printing metallic nanostructures on a fiber optic facet.

Appendix B

Nanotransfer Printing *via* Fluropolymer Coated Stamp

Similar to teflon, plasma polymerized fluorocarbons have lowest surface energy and can easily release any materials embedded on it. Because of relatively high elastic modulus than widely used PDMS stamp, they are less prone to deformation and feature collapse during printing process. The stamp can be repeatedly metal-inked and scale-up the production without any harsh step. Despite these attractive features, plasma polymerized fluorocarbon-assisted nTP has not been studied yet.

We have recently developed an *in situ* protocol to deposit teflon-like thin film on nanostructured surface via plasma-assisted polymerization of fluorocarbon (i.e., octafluorocyclobutane). The polymer thin film is then used as a proficient mediator to transfer print nanofeatures. At first, top-down nanolithography approach was used to create a variety of nanofeatures on positive e-beam resist (Zep520A) coated silicon wafer. Following Cr-mask deposition and lift-off procedure, silicon relief pillars were created using reactive ion etcher. Thus created relief features were then plasma treated along with fluorcarbon gas on a nanostructured surface. Metal thin film was then vapor deposited onto polymer coated relief pillars prior to nTP. Figure B.1 shows SEMs of nanofabricated stamp and gold patterns printed on quartz substrate.

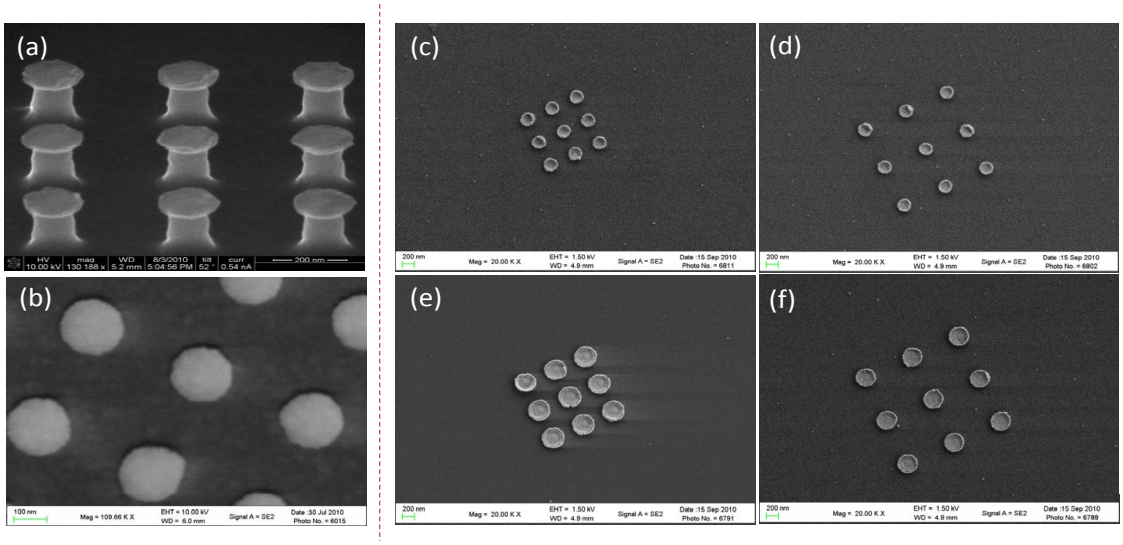


Figure B.1: Electron beam lithography and nanotransfer printing created nanoarrays: (a) 45° tilted view of fluoropolymer coated stamp, (b) top-view of the stamp after vapor deposition of 30 nm gold, (c-f) different size and spacing gold arrays tranfer printed on quartz surfaces.

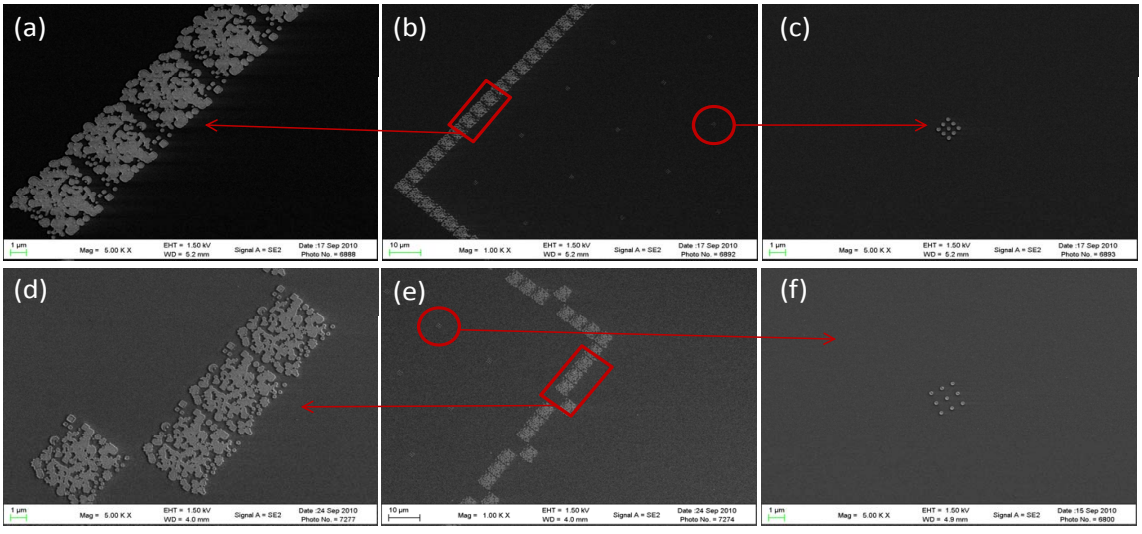


Figure B.2: Silver nanopatterns imprinted on quartz surface without any surface modification of a substrate (a-c); and gold nanopatterns on quartz surface treated with mercaptosilane griping reagent.

The proposed plasma polymerized film mediated nTP protocols have numerous advantages over widely known PDMS based printing. Polymer coated silicon stamps are robust and can be re-used after simple cleaning step. Plasma polymerized thin films are well-known for their excellent adhesion to substrate materials and strong chemical resistance. Meanwhile, due to its low surface energy it promotes easy release of any materials embedded on its surface. These qualities add-on the significance of this fast and convenient dry chemical process for efficient transfer printing. *In situ* polymer deposition step is a fast process and can grow ∼10 nm thin film in <10 sec. The substrate material and stamp may not require additional chemical modifications prior to nTP (Figure B.2). It can create nanoparticles of approximately 50 nm width and/or diameter and has interparticle spacing resolution of sub 10 nm. Various complex nanostructures were created on silicon wafers and were replicated on quartz and silicon substrates (Figures B.3 and B.4).

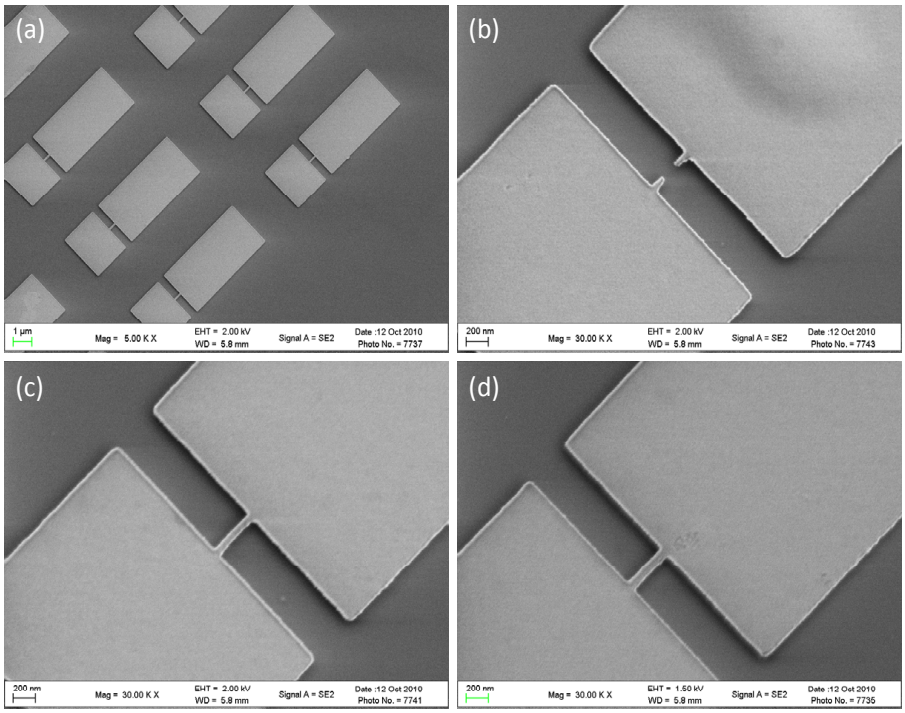


Figure B.3: SEMs of transfer printed nanowire sensors: (a) Nanowire sensor array, (b) 12 nm wide (CAD design) connecting wire, (c) 24 nm wide (CAD design) connecting wire, (d) 32 nm wide (CAD design)connecting wire.

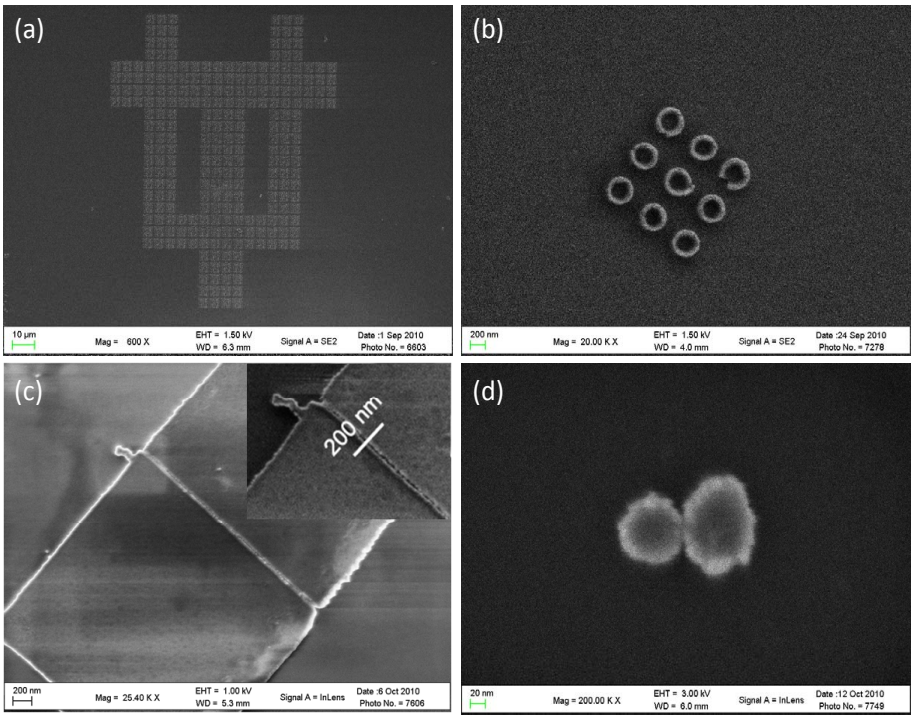


Figure B.4: SEMs of various nanostructured devices fabricated via nTP: (a) Nanoaggregates of random morphology nanoparticles cloned on large UT pattern, (b) palladium nanoring array, (c) Planer nanogap gold electrode, (d) Just-touching dimer nanoparticles.

Vita

Deepak was born and raised in a beautiful mountainous country, Nepal. He earned his BS and MS degrees in Chemistry from the Tribhuvan University. After graduating with a Master degree in Physical Chemistry he took off to the other side of the world in August 2006, to join the University of Tennessee-Knoxville, for the doctoral degree. He is under the direction of Professor Michael Sepaniak in the department of Chemistry. In May 2011 he will graduate with a Ph.D. in Chemistry.